IAEA TECDOC SERIES

IAEA-TECDOC-2012

Muon Imaging

Present Status and Emerging Applications

IAEA
International Atomic Energy Agency

MUON IMAGING

The following States are Members of the International Atomic Energy Agency:

AFGHANISTAN
ALBANIA
ALGERIA
ANGOLA
ANTIGUA AND BARBUDA
ARGENTINA
ARMENIA
AUSTRALIA
AUSTRIA
AZERBAIJAN
BAHAMAS
BAHRAIN
BANGLADESH
BARBADOS
BELARUS
BELGIUM
BELIZE
BENIN
BOLIVIA, PLURINATIONAL STATE OF
BOSNIA AND HERZEGOVINA
BOTSWANA
BRAZIL
BRUNEI DARUSSALAM
BULGARIA
BURKINA FASO
BURUNDI
CAMBODIA
CAMEROON
CANADA
CENTRAL AFRICAN REPUBLIC
CHAD
CHILE
CHINA
COLOMBIA
COMOROS
CONGO
COSTA RICA
CÔTE D'IVOIRE
CROATIA
CUBA
CYPRUS
CZECH REPUBLIC
DEMOCRATIC REPUBLIC OF THE CONGO
DENMARK
DJIBOUTI
DOMINICA
DOMINICAN REPUBLIC
ECUADOR
EGYPT
EL SALVADOR
ERITREA
ESTONIA
ESWATINI
ETHIOPIA
FIJI
FINLAND
FRANCE
GABON
GEORGIA
GERMANY
GHANA
GREECE
GRENADA
GUATEMALA
GUYANA
HAITI
HOLY SEE
HONDURAS
HUNGARY
ICELAND
INDIA
INDONESIA
IRAN, ISLAMIC REPUBLIC OF
IRAQ
IRELAND
ISRAEL
ITALY
JAMAICA
JAPAN
JORDAN
KAZAKHSTAN
KENYA
KOREA, REPUBLIC OF
KUWAIT
KYRGYZSTAN
LAO PEOPLE'S DEMOCRATIC REPUBLIC
LATVIA
LEBANON
LESOTHO
LIBERIA
LIBYA
LIECHTENSTEIN
LITHUANIA
LUXEMBOURG
MADAGASCAR
MALAWI
MALAYSIA
MALI
MALTA
MARSHALL ISLANDS
MAURITANIA
MAURITIUS
MEXICO
MONACO
MONGOLIA
MONTENEGRO
MOROCCO
MOZAMBIQUE
MYANMAR
NAMIBIA
NEPAL
NETHERLANDS
NEW ZEALAND
NICARAGUA
NIGER
NIGERIA
NORTH MACEDONIA
NORWAY
OMAN
PAKISTAN
PALAU
PANAMA
PAPUA NEW GUINEA
PARAGUAY
PERU
PHILIPPINES
POLAND
PORTUGAL
QATAR
REPUBLIC OF MOLDOVA
ROMANIA
RUSSIAN FEDERATION
RWANDA
SAINT KITTS AND NEVIS
SAINT LUCIA
SAINT VINCENT AND THE GRENADINES
SAMOA
SAN MARINO
SAUDI ARABIA
SENEGAL
SERBIA
SEYCHELLES
SIERRA LEONE
SINGAPORE
SLOVAKIA
SLOVENIA
SOUTH AFRICA
SPAIN
SRI LANKA
SUDAN
SWEDEN
SWITZERLAND
SYRIAN ARAB REPUBLIC
TAJIKISTAN
THAILAND
TOGO
TONGA
TRINIDAD AND TOBAGO
TUNISIA
TÜRKİYE
TURKMENISTAN
UGANDA
UKRAINE
UNITED ARAB EMIRATES
UNITED KINGDOM OF GREAT BRITAIN AND NORTHERN IRELAND
UNITED REPUBLIC OF TANZANIA
UNITED STATES OF AMERICA
URUGUAY
UZBEKISTAN
VANUATU
VENEZUELA, BOLIVARIAN REPUBLIC OF
VIET NAM
YEMEN
ZAMBIA
ZIMBABWE

The Agency's Statute was approved on 23 October 1956 by the Conference on the Statute of the IAEA held at United Nations Headquarters, New York; it entered into force on 29 July 1957. The Headquarters of the Agency are situated in Vienna. Its principal objective is "to accelerate and enlarge the contribution of atomic energy to peace, health and prosperity throughout the world''.

IAEA-TECDOC-2012

MUON IMAGING

PRESENT STATUS AND EMERGING APPLICATIONS

INTERNATIONAL ATOMIC ENERGY AGENCY
VIENNA, 2022

COPYRIGHT NOTICE

All IAEA scientific and technical publications are protected by the terms of the Universal Copyright Convention as adopted in 1952 (Berne) and as revised in 1972 (Paris). The copyright has since been extended by the World Intellectual Property Organization (Geneva) to include electronic and virtual intellectual property. Permission to use whole or parts of texts contained in IAEA publications in printed or electronic form must be obtained and is usually subject to royalty agreements. Proposals for non-commercial reproductions and translations are welcomed and considered on a case-by-case basis. Enquiries should be addressed to the IAEA Publishing Section at:

Marketing and Sales Unit, Publishing Section
International Atomic Energy Agency
Vienna International Centre
PO Box 100
1400 Vienna, Austria
fax: +43 1 26007 22529
tel.: +43 1 2600 22417
email: sales.publications@iaea.org
www.iaea.org/publications

For further information on this publication, please contact:

Physics Section
International Atomic Energy Agency
Vienna International Centre
PO Box 100
1400 Vienna, Austria
Email: Official.Mail@iaea.org

© IAEA, 2022
Printed by the IAEA in Austria
October 2022

IAEA Library Cataloguing in Publication Data

Names: International Atomic Energy Agency.
Title: Muon imaging / International Atomic Energy Agency.
Description: Vienna : International Atomic Energy Agency, 2022. | Series: IAEA TECDOC series, ISSN 1011–4289 ; no. 2012 | Includes bibliographical references.
Identifiers: IAEAL 22-01542 | ISBN 978–92–0–142722–9 (paperback : alk. paper) | ISBN 978–92–0–142622–2 (pdf)
Subjects: LCSH: Muons. | Muons — Imaging. | Radiography.

FOREWORD

X ray, neutron and gamma radiography have been widely used in industry as non-destructive testing methods for industrial quality control and to assess the safety and integrity of structures and components. These techniques use reasonably intense, artificial radiation sources (small accelerators or sealed isotopic sources) in laboratories and at industrial sites. Muon radiography, which is based on cosmic rays, is an alternative for certain applications that does not require artificial sources of ionizing radiation, and so is without regulatory constraints.

High energy primary cosmic ray particles (mainly protons) interact with the nuclei composing the Earth's upper atmosphere to produce copious numbers of charged pi-mesons, which decay into muons. Muons are similar to electrons in that they are elementary particles but with approximately 200 times the mass. They interact with matter mainly through electromagnetic force and are easily capable of reaching the Earth's surface. All other high energy charged particles, as well as gamma rays, are effectively shielded by the atmosphere so that muons represent the vast majority of charged cosmic rays at the Earth's surface.

Some muons can penetrate hundreds of metres of rock and so can be used as a highly penetrating, non-destructive natural probe. Muons can be readily used for imaging in situations where days or more of exposure time are available. Various techniques have been developed that aim to measure the attenuation, transmission or scattering of the muon flux. Using these, information concerning the composition and dimensions of the materials encountered can be estimated.

Numerous potential applications have been identified — ranging from examination of modern and ancient built environments, volcanology and industry, to nuclear security and safeguards — that have attracted attention around the world. This international interest led to a Technical Meeting held in Vienna in 2019, which was attended by 28 participants from 14 Member States and a representative from the European Commission. This publication is the output of that meeting.

The IAEA acknowledges the valuable contributions and support of the international experts who contributed to the drafting and review of this publication, particularly A. Giammanco (Belgium). The IAEA officers responsible for this publication were F. Foulon and I. Swainson of the Division of Physical and Chemical Sciences.

EDITORIAL NOTE

This publication has been prepared from the original material as submitted by the contributors and has not been edited by the editorial staff of the IAEA. The views expressed remain the responsibility of the contributors and do not necessarily represent the views of the IAEA or its Member States.

Neither the IAEA nor its Member States assume any responsibility for consequences which may arise from the use of this publication. This publication does not address questions of responsibility, legal or otherwise, for acts or omissions on the part of any person.

The use of particular designations of countries or territories does not imply any judgement by the publisher, the IAEA, as to the legal status of such countries or territories, of their authorities and institutions or of the delimitation of their boundaries.

The mention of names of specific companies or products (whether or not indicated as registered) does not imply any intention to infringe proprietary rights, nor should it be construed as an endorsement or recommendation on the part of the IAEA.

The authors are responsible for having obtained the necessary permission for the IAEA to reproduce, translate or use material from sources already protected by copyrights.

The IAEA has no responsibility for the persistence or accuracy of URLs for external or third party Internet web sites referred to in this publication and does not guarantee that any content on such web sites is, or will remain, accurate or appropriate.

CONTENTS

1. INTRODUCTION

This Section introduces the basic concepts of muon radiography (also known by the term 'muography'), muon scattering tomography, and the terminology used through the rest of this document. It describes the principles of the methods, the main techniques and their range of applicability, and finally some of the main practical issues. Muon imaging and its applications were recently highlighted in the IAEA Nuclear Technology Review [1]. More detailed methodological information can be found in the review in Ref. [2].

1.1. BACKGROUND

The muon (μ) is an elementary particle with the same electric charge and spin as the electron. It has a mass of about 1.9×10^{-25} g, or equivalently 105 megaelectron volts [MeV] in 'natural units', where the speed of light in the vacuum (c) is conventionally set to 1. This is equivalent to almost 200 times the mass of the electron. The sign of its electric charge can be positive or negative. In contexts where this is important, the sign of the charge is indicated by a '+' or '–' superscript, and the word 'muon' indicates μ^- while 'anti-muon' indicates μ^+.

Muons are unstable, and decay almost exclusively into electrons (symbol e^-) and pairs of neutral and almost massless particles known as neutrinos (ν): one muonic neutrino and one electronic anti-neutrino. Conversely, anti-muons decay into positrons (i.e., anti-electrons, e^+) and neutrinos of opposite denomination (i.e., one muonic anti-neutrino and one electronic neutrino). The average lifetime of a muon is 2.2 μs when at rest, but one of the key effects predicted by the Theory of Relativity is the dilation of its observable lifetime by the so-called Lorentz factor, which is a function of muon momentum. For momenta of several gigaelectron volts [GeV], as is typical for muons of cosmogenic origin used in muon imaging, the dilation is such that they can traverse the Earth's atmosphere without decaying. Therefore, for practical purposes, the tiny fraction of muons that decay before being detected or being absorbed is usually ignored.

Below, we elaborate on how muons are naturally produced in cosmic ray interactions and how they interact with matter. More information (and the source for all the quantitative statements in this Section, unless otherwise indicated) can be found in the Review of Particle Physics, periodically updated by the Particle Data Group [3].

Cosmic rays are subatomic particles that travel through interplanetary, interstellar or even intergalactic space. The term 'primary cosmic rays' is often used for these to distinguish them from 'secondary cosmic rays', a term employed for the particles produced in cascades produced by the interactions of primary cosmic rays with other particles. Primary cosmic rays consist mostly of protons, with small fractions of heavier nuclei, electrons, positrons and antiprotons.

Muons are examples of secondary cosmic rays, which are abundantly and freely produced by the interaction of primary cosmic rays within the upper atmosphere typically at heights 15 to 16 km above sea level. For this reason, they are called 'atmospheric muons', to distinguish them from those originating from other production mechanisms (including anthropogenic muons produced in particle physics laboratories.) The spectra of cosmic ray protons and other primary cosmic rays can extend to very large energies: it is not uncommon that they exceed even the largest kinetic energies reached by the Large Hadron Collider. They collide with atmospheric nuclei in the atmosphere and interact via the strong nuclear force. Many of the collisions are sufficiently energetic that they not only break up nuclei, but also their constituent protons and neutrons. Only hadrons (i.e., particles composed of quarks and/or antiquarks) are sensitive to

the strong nuclear force, and both protons and neutrons are examples of these. High-energy collisions cause the production of new hadrons that can further interact with the atmosphere by the strong nuclear force, or by the electromagnetic force, unless they decay. A cascade of particles (called a 'cosmic shower') develops in the atmosphere, due to multiple nuclear and electromagnetic interactions. Pions and kaons are the hadrons most abundantly produced in these cascades. They can be charged or neutral, and when they are charged their dominant decay modes produce muons: this is the main production mechanism of atmospheric muons.

Muons are not hadrons and are assumed to be elementary particles. At sea level, muons constitute the vast majority of the charged particles in a cosmic shower (and the second most abundant particle species after neutrinos), arriving at an intensity of roughly 100 $m^{-2}s^{-1}$. Other charged particles (hadrons, electrons and positrons) are produced in the cosmic showers and in a fraction of cases reach sea level, constituting a potential background for measurements of atmospheric muons.

The behaviour of muons is very different from that of other secondary cosmic ray particles. Not being a hadron, the muon is insensitive to strong nuclear interactions. The muon is an elementary lepton, like the electron, and being electrically charged it is subject to energy loss via electromagnetic interactions such as bremsstrahlung. Recalling that the mass of a muon is approximately 200 times that of an electron, and as losses from bremsstrahlung follow a $1/m^2$ dependence (where m is the particle mass), losses of kinetic energy via this mechanism are ~40,000 times smaller for muons than for electrons and positrons (the latter of which readily annihilate with electrons in the atmosphere). Therefore, muons have a negligible probability of producing electromagnetic cascades, which become significant only for the rare atmospheric muons with momenta greater than 500 GeV. Ionization and atomic excitation are the dominant energy loss mechanisms of muons through matter.

The Bethe function [4] describes the mean energy loss per unit distance (i.e., the stopping power) of swift charged particles traversing matter. At sea level, the atmospheric muon spectrum peaks at ca. 4 GeV; in this region, the mean energy loss rate is close to the minimum of the Bethe function, is almost linearly dependent on the density of the traversed material, and only very mildly dependent on other properties of the material. The 'range' of a muon in a given material is defined as the distance that a muon can travel before dissipating all of its kinetic energy inside the material and coming to rest. The 'opacity' of an object along a line of sight is defined as the density integrated along that line. The 'metre water equivalent' (mwe) is the common unit for opacity[1]. For muons, energy loss is about 0.2 GeV/mwe. The measurement of opacity is at the core of the muon transmission (or muon absorption) method, also known as 'muography'.

Coulomb scattering affects all charged particles passing through matter because of the intense electric fields near nuclei. Rutherford's Law gives the angular probability distribution, θ, for single scattering. When traversing a macroscopic amount of material, a muon undergoes several individual scattering events; as most deflections are small, the θ distribution has an approximately Gaussian shape, as expected from the central limit theorem, with a long tail that is inversely proportional to $\sin^4(\theta/2)$, following Rutherford's Law. This tail arises from rare large-scattering events. The Gaussian approximation describes ~98% of the actual distribution. The average muon deflection, $\langle\theta\rangle$, due to Coulomb scattering, is always zero. The width of the θ distribution depends on x/X_0 (at first order proportional to $\sqrt{x/X_0}$), where x is the distance traversed by the muon within the material. X_0 is the so-called 'radiation length' and is a property

[1] 1 mwe = 100 g/cm^2

of the material, with a strong dependence on the number of protons in the nucleus (i.e., the atomic number, Z). The resulting dependence on Z of the θ distribution is the basis for the 'scattering method' or 'muon scattering tomography'.

1.2. OBJECTIVE

As this is the first IAEA TECDOC devoted to muon imaging, it aims to provide the reader with an overview of examples of modern muon imaging systems and methods and to illustrate their application for a diverse set of uses and fields.

1.3. SCOPE

The scope includes a general introduction to the principles of muon imaging, illustrated with case studies. Explanation of all technical details is outside of the scope of this document, but the numerous references provide further detail.

1.4. STRUCTURE

Section 2 describes the principles of the main muon imaging techniques, their range of applicability, the main detection technologies employed, and how 2D and 3D images are in general extracted. Sections 3 through 6 are dedicated to specific application areas. Section 3 illustrates case studies of interest for civil engineering, where muography is employed in the detection of defects or cavities, or for monitoring the stability of built structures. Section 4 provides examples of industrial applications of both muography and muon scattering. Section 5 is devoted to applications of muography to volcanology, with an overview of the main ongoing activities in Japan, Italy and France. Examples of the application of muography to archaeology are given in Section 6. The following Sections describe uses of the scattering method for the identification of special nuclear materials. Section 7 is devoted to security applications, such as prevention of smuggling of nuclear material at border controls. Section 8 illustrates several case studies of nuclear waste characterization, while Section 9 provides examples of applications to nuclear safeguards and nuclear material control; i.e., prevention and timely detection of diversion of nuclear material from peaceful use. Section 10 concludes this document with a summary of its key points and some thoughts on future perspectives.

2. OVERVIEW OF MUON IMAGING

This Section introduces the two main general categories of muon imaging methods and their typical areas of application, the most popular particle detection technologies, and some algorithmic considerations on how to go from raw data to 2D and 3D images, which are discussed further in later Sections.

2.1. MUON IMAGING METHODS

The two electromagnetic phenomena of absorption by energy loss and Coulomb scattering affect all muons passing through matter; they can be separately exploited by the two general classes of muon imaging: muography and muon scattering tomography (MST), illustrated in Fig. 1.

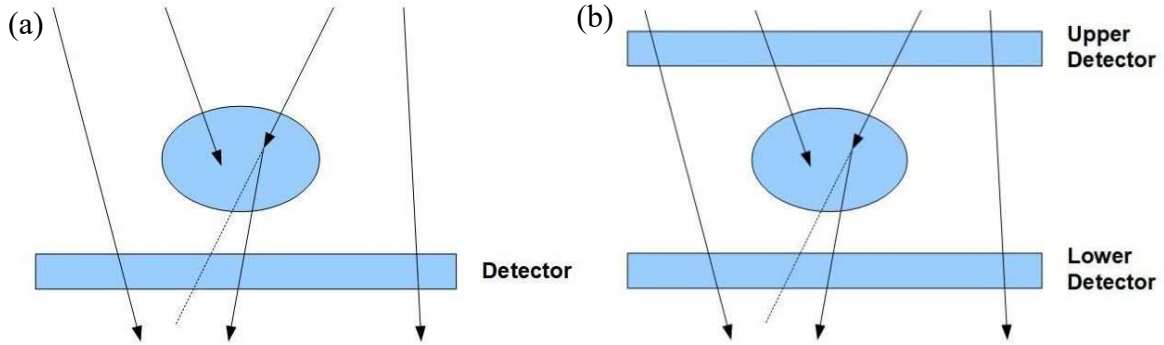

FIG. 1. These two sketches illustrate the typical detector configurations, with respect to the object to be imaged. (a) muon transmission radiography (muography), where the fraction of muons surviving energy loss is measured, and (b) muon scattering tomography (MST), where the observable of interest is the root-mean-square of the deflection angle (courtesy of A. Giammanco, Université catholique de Louvain).

Both techniques require a large statistical sample of muons. Muography is in general suitable for very large targets, whereas MST is better suited to small and medium sized targets. Muon scattering tomography requires reconstruction of muon trajectories ahead of and behind the target: this is impractical for mountains or large buildings. In contrast, muography needs only a single 'tracker' (see Sections 2.1.1 and 2.1.2) after the target. The thicker the target, the fewer muons pass through. This reduction in count rate is a loss of information for MST, whereas for muography, it forms part of the information. Nevertheless, MST is uniquely sensitive to Z, and for small targets it is often the best method.

Muography and MST rely on absorption and scattering of muons, respectively, but these processes present reciprocal challenges: when choosing the absorption/transmission method, scattering tends to smear the image; when applying the scattering method, the loss of muons during the traversal of the object to be imaged depletes the statistics. Moreover, both effects depend on the muon momentum, a parameter that is not measured on an individual basis and whose spectrum has large modelling uncertainties.

The following subsections provide practical details on the two classes of muon imaging.

2.1.1. Muography

Historically, muography was the first technique to be exploited, with the earliest known example dating to the 1950's (a measurement of the overburden of a tunnel using a Geiger counter mounted on a rail [5]).

Muography is the method of choice, in general, when it is impossible or impractical to track the trajectory of a muon both before and after the object of interest. Examples of fields of application include archaeology (where it was first applied in the 1960's, famously leading to the conclusive exclusion of the presence of hidden chambers in the Second Pyramid of Giza, in Egypt [6]), volcanology and general geosciences, and civil engineering.

Figs 2 and 3 illustrate two typical uses of muography.

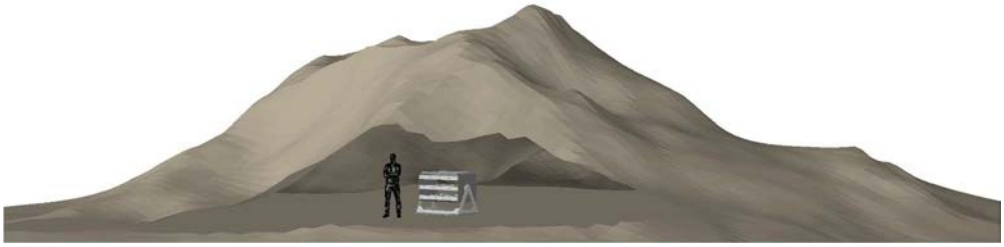

FIG. 2. Muography has been used in various studies to map the overburden of natural or artificial cavities such as caverns or tunnels. In this configuration, the muon detector exploits the fact that the muon flux is maximum for angles close to the zenith (reproduced from Ref. [2] with permission courtesy of Elsevier).

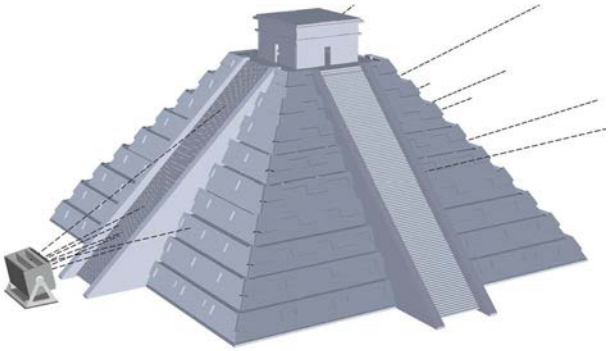

FIG. 3. Muography has been employed to search for hidden chambers in pyramids in Egypt and Mexico, and for several other archaeological uses. When the muon detector cannot be placed underneath the object of interest, as in this example, longer data-taking campaigns are needed to accumulate sufficient statistics because of the strong reduction of the muon flux as a function of zenith angle (reproduced from Ref. [2] with permission courtesy of Elsevier).

A muon detector measures muon flux arriving only within the detector's acceptance. By comparing to the 'free sky' flux, the probability of muon absorption along any particular line of sight can be determined (also known as 'muon transmission'), which is directly related to the opacity (see Section 1). Where target thicknesses along lines of sight of the detector have been determined (e.g., cases in which the surfaces of the target are precisely known), the opacity along each line of sight can be transformed to a measurement of average density, ρ, along that line. Conversely, when a target's average ρ is known, the boundaries of a target can be determined using such methods.

The statistical precision of muography depends on the number of observed muons, N, via the formula (deduced from Poisson counting statistics): $\Delta L/L_0 = 1/\sqrt{N}$, where L is the path length and L_0 is the mean free path. Consequently, the relative uncertainty of the opacity scales linearly with the density and the thickness of the object to be imaged and inversely with the square root of the data collection time (which is directly proportional to N if one neglects small, time-dependent variations in flux).

Most muon detectors for muography take the form of a hodoscope, or 'tracker'. A hodoscope is an instrument composed of various layers, each of them sensitive to the point of passage of a charged particle, from which a trajectory can be reconstructed. However, other configurations are possible. For example, as illustrated in Fig. 4, some examples exist of muon detectors hosted in narrow boreholes, which imposes limitations in size and favours cylindrical symmetry. This type of set-up was originally proposed in a simulation study [7] in the 1970's that compared the relative performance, in terms of geometrical acceptance, of a cylindrical detector in a borehole (which may be drilled specifically for this purpose) to that of a traditional hodoscope geometry (which requires the existence of an accessible tunnel at a convenient location).

FIG. 4. A borehole can be used to host a small-sized muon detector with cylindrical shape (reproduced from Ref. [2] with permission courtesy of Elsevier).

2.1.2. Muon scattering tomography

The first proposal [8] to exploit Coulomb scattering of muons dates to 2003, making this technique almost half a century younger than the muography method. Since that seminal paper, several applications of the MST method have been proposed where distinguishing higher-Z from lower-Z materials is important, including the prevention of smuggling of nuclear material using cargo scanning and the interrogation of the content of nuclear waste casks. Attempts are also being made to use MST (sometimes in conjunction with muography) to identify low-Z materials such as drugs or explosives [9].

Muon scattering tomography relies on the knowledge that when muons or antimuons pass through matter they sometimes get close enough to a nucleus to experience a significant electromagnetic interaction. This phenomenon has been known for more than a century, when a series of crucial experimental observations by Geiger and Marsden, using α particles instead of muons, were explained by Rutherford [10] with his eponymous $1/\sin^4(\Delta\theta/2)$ law.

The nuclei of different elements have different electric charge (Z, the atomic number in units of the proton charge) and, therefore, different strengths of electromagnetic interaction with muons. The larger the electric charge of the nucleus, the stronger will be the electromagnetic force that it will exert on the muon when it passes by. The principal idea behind the MST

method is to correlate the root-mean-square deflection with the type of material, small for light (low Z) elements and large for heavy elements such as Pb ($Z = 82$), U ($Z = 92$) or Pu ($Z = 94$). Fig. 5 illustrates this principle.

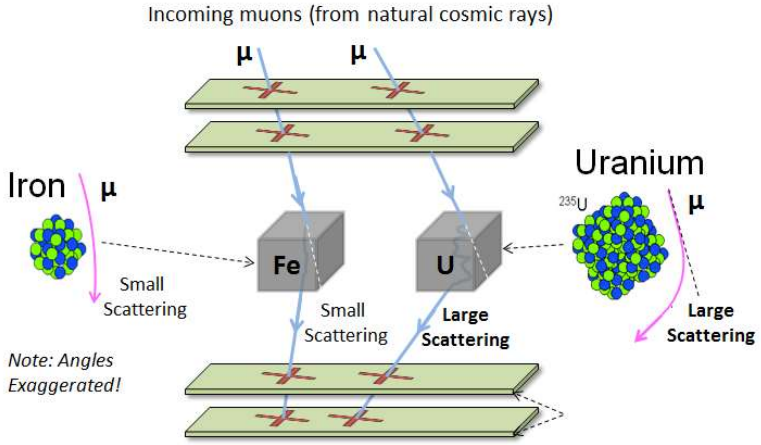

FIG. 5. Illustration of the ability of muon scattering tomography (MST) to discriminate between different materials. The atomic number is Z=26 for Fe and Z=92 for U (courtesy of B. Locke and M. Hohlmann, Florida Institute of Technology).

Most of the materials of interest for the nuclear sector are heavy. Therefore, the intrinsic capability of discriminating between materials by Z makes MST a promising technique for applications such as nuclear waste characterization, nuclear security and safeguards, and material control. A few companies are active in the development of 'muon portals' for cargo scanning, as illustrated in Fig. 6, while others specifically focus on the interrogation of nuclear waste, see Fig. 7.

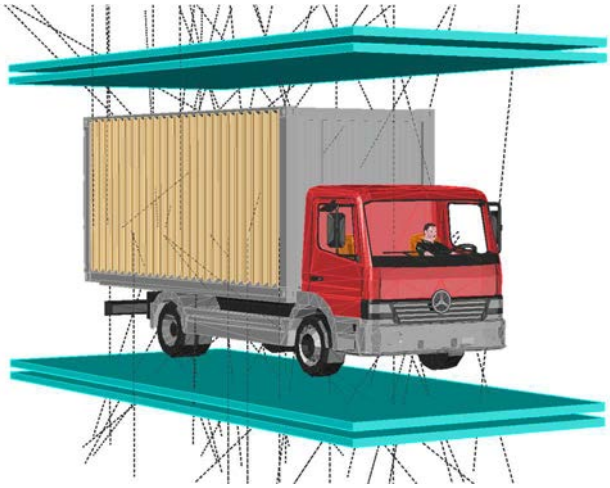

FIG. 6. Muon scattering tomography (MST) can be used for cargo scanning (reproduced from Ref. [2] with permission courtesy of Elsevier).

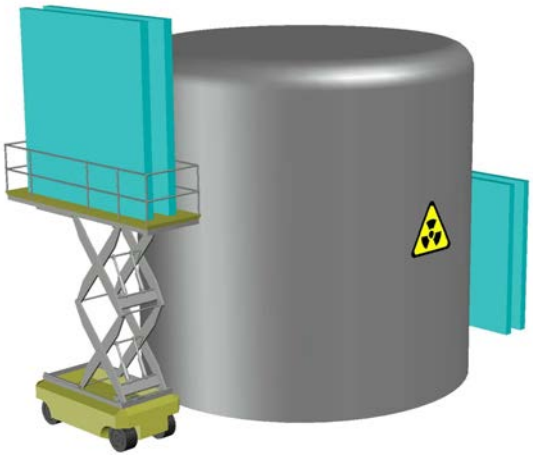

FIG. 7. Muon scattering tomography (MST) is used for the interrogation of nuclear waste casks (reproduced from Ref. [2] with permission courtesy of Elsevier).

The MST method requires reconstruction of the muon's trajectory both before and after it passes through the object to be imaged. Therefore, a typical MST apparatus comprises a tracking device on top of the object and a second detector underneath, as in Fig. 6. Other arrangements may be more appropriate in specific cases, as illustrated in Fig. 7. Both trackers separately reconstruct a muon trajectory. If both trackers register a muon within a narrow time window, it is assumed that they see the same muon. The two muon trajectories are extrapolated within the object to be imaged, and various algorithms may be applied to deduce the place or places where the muon scattered off a nucleus. More information is provided in Section 2.3.3.

The precision of the MST method in estimating the path length, L, of a given material is given by $\Delta L/L = \sqrt{(2/N)}$, where N is the number of observed muons [11].

2.1.3. General considerations about imaging methods

Not only the size but also the composition of the objects of interest determine whether muography or MST is most appropriate. Table 1 gives a compilation of the relevant properties of a few materials. Broadly speaking, when interested in the mass density (ρ) one uses muography, while MST is mostly used to discriminate between Z of materials via its scaled scattering density (λ).

While muography and MST are used in the vast majority of muon imaging undertaken with atmospheric muons, a few variants are employed in specific uses presented in this publication. One variant of muography is the absorption method, in which the same physical mechanism is used as in standard muography but, as in the MST method, instrumentation has to be deployed both upstream and downstream of the volume of interest. The image obtained from absorption can be considered as a sort of 'negative image' of the one obtained from transmission[2]: the projected density is deduced by how many muons detected by the upper tracker get absorbed by the object before reaching the lower detector. Examples of applications of this method are given in Sections 3.1 and 9.1.2.

[2] The reader has to be careful that the terms 'transmission method' and 'absorption method' are used interchangeably in the relevant literature, to indicate what we are here calling muography.

TABLE 1. ATOMIC NUMBER (Z), MASS DENSITY (ρ), RADIATION LENGTH (X_0) AND SCALED SCATTERING DENSITY, $\lambda=\rho/X_0$, FOR A FEW REPRESENTATIVE MATERIALS

Material	Z	ρ (g/cm^3)	X_0 (g/cm^2)	$\lambda=\rho/X_0$ (cm^{-1})
Air (sea level)	N: 7, O: 8	1.225×10^{-3}	36.7	3.3×10^{-5}
Water	O: 8, H: 1	1	36.1	0.028
Quartz (SiO_2)	Si: 14, O: 8	2.65	27.1	0.10
Al	13	2.7	24.0	0.11
Fe	26	7.9	13.8	0.57
Cu	29	8.9	12.9	0.70
W	74	19.3	6.8	2.9
Pb	82	11.3	6.4	1.8
U	92	19.0	6.0	3.1

Note: The radiation lengths of air, water, and metals are taken from Ref. [12], the density of air at 15 °C under conditions typical at sea level comes from Ref. [13], the density of quartz was chosen as representative of silicate minerals, which constitute 90% of the Earth's crust, and its radiation length has been estimated, based on its chemical composition (SiO_2), using a formula from Ref. [12].

Another case where one needs two muon trackers is monitoring of the relative alignment of sub-structures of a large object such as a building. This technique, presented in Section 3.3, employs the fundamental property that multiple Coulomb scattering affects the width but not the mean of the angular distribution (see Section 1.1) of muons. Some teams are considering advanced analysis techniques, including machine learning [14], to combine the relative merits of more than one technique.

2.2. PARTICLE DETECTION TECHNIQUES

Although a large variety of particle detection techniques have been developed in nuclear and particle physics, not all of them fulfil the requirements of long-term stability, low cost, and ruggedness that are often required for muon imaging applications. On the other hand, the low event rates characteristic of muon imaging mean that data acquisition and front-end electronics are not a technological challenge. Detector geometries and technologies can be optimized for particular uses, and a wide variety of systems have been built, with only a few common features between them. One such common feature is the inability to determine muon momentum on a per-particle basis. The standard way to do so would be to employ a magnetic field to deflect the trajectory of the muons, but this would make the apparatus quite expensive and heavy.

At the time of writing this report, the majority of teams active in this area appear to have settled on just three families of detectors, based on scintillating materials (Section 2.2.1), on gaseous detectors (Section 2.2.2), and on emulsion films (Section 2.2.3), although some exceptions exist (Section 2.2.4). In all three main categories, the basic physical mechanism that allows the detection of a muon passing through a sensitive layer is the ionization of atoms along the muon's path (see Section 1.1).

2.2.1. Scintillator detectors

Scintillating materials emit light by fluorescence when their atoms relax after being excited by the passage of a charged particle (e.g., muon). This light is collected by a photomultiplier and the resulting electronic signal yields information on the amount of energy released by the

impinging muon[3] by ionization in the scintillating material. A variety of such materials are in use in physics laboratories and radiation detection applications, including crystal, plastic, and liquid scintillators. Plastic scintillators are very popular in muon imaging (and especially muography) as they are generally regarded as robust, reliable, and simple to operate. They are most appropriate for uses where spatial, and consequently angular, resolution is not crucial. Fast response plastic scintillators are suitable for use in harsh environments, and systems based around these can be made at reasonable price to performance ratios. Moreover, plastic scintillators are easily shaped into various geometries (e.g., from square to rectangular to triangular bars), allowing easy customization of detector geometry. Some teams are using scintillating materials in the form of thin fibres [15].

2.2.2. Gaseous detectors

In many detectors, the sensitive material is in gaseous form. A muon leaves a trail of electron–ion pairs in its wake as it crosses the gas volume. These electrons and ions are collected by applying an electric field, causing them to drift towards the electrodes where they induce an electric signal. Depending on the potential difference between the electrodes, qualitatively different phenomena affect the electrons and ions in traversing the gas. This leads to a classification of gaseous detectors [16] as ionization chambers, proportional counters, and Geiger-Mueller counters, depending on the voltage.

A variety of geometrical arrangements are in use. Cylindrical geometries, where thin wire anodes (~100 μm) collect the electrons created by ionization are commonly used. Multi-wire chambers apply the same principle, but – as the name suggests – several wires share a common gas volume. In another common geometry, both anode and cathode are planar and parallel to each other.

Gaseous detectors use fewer, simple, electronic channels (thanks to gas amplification that compensates in part for the low natural flux of muons). High resolution, large area detectors can be built often at a cheaper price than scintillator detectors. Therefore, position sensitive layers made of assemblies of adjacent gaseous detectors can be quite affordable.

2.2.3. Emulsion detectors

Emulsion detectors are composed of thick photographic plates with very uniform, fine grains that record the track of a charged particle. After development of the photographic plates, the muons that passed through them can be seen under a microscope. Emulsion detectors were some of the earliest particle detectors developed. They still play an important role in large-scale neutrino experiments.

Nuclear emulsions have resolutions determined by the size of the emulsion grains, and are frequently of the order of microns. Multiple films of emulsions can be assembled to form thin tracking layers, which can achieve angular spatial resolutions of the order of few milliradians.

A crucial characteristic from the point of view of muography is that nuclear emulsion detectors do not need any power supply, making them an excellent choice for poorly accessible locations. See for example Ref. [17] where pre-assembled nuclear emulsion detectors were put in place with the help of a helicopter. Moreover, the cost of such systems is relatively low, and they can allow competitive angular resolution of 3 mrad in thin layers (of 1 mm), which is markedly

[3] Here, and in the following subsections, the specific response of these detectors to the passage of a muon is presented, but the same physical mechanisms are at play for any other electrically charged particle.

different from other tracking detectors that typically require a meter scale base to achieve similar performance. However, some important limitations have an impact on their prospects for a broader adoption in the community, the most important of which are probably the following:

- First, there is no timing information, as emulsion film starts recording particle tracks from inception and all tracks recorded during the full period of exposure are superimposed. This makes them unusable for MST, and it also limits their applications in muography as it excludes any possibility of monitoring the evolution through time of the observed objects, which is a serious limitation for the study of dynamical systems such as active volcanoes.
- Second, very specific equipment is needed to analyse the nuclear emulsion plates. The OPERA[4] (see Ref. [18]) neutrino experiment developed automated, motorized optical systems and pattern recognition to reconstruct neutrino track candidates in a reasonable amount of time (typically hours per cm^2). However, few laboratories have such systems, which limits access for muon applications;
- The level of sensitivity to high temperatures.

Nevertheless, emulsions have demonstrated excellent performance for muography experiments in a wide range of difficult environments, recording data over months.

2.2.4. Other detection techniques

Several other particle detection techniques are commonly employed in nuclear and particle physics, but the three detector families outlined so far account for the vast majority of muon imaging setups.

There have been proposals to use semiconductor position sensitive detectors (e.g., silicon microstrip or pixel detectors) in muon imaging. The main obstacle to their usage is the large cost per unit area, but their compactness and relative radiation hardness make them appealing options for monitoring highly radioactive waste [19] as well as for applications in space [20].

One muography team proposes the usage of atmospheric Cherenkov imaging in volcanology [21], exploiting the Cherenkov effect; i.e., the emission of electromagnetic radiation (Cherenkov light) when a muon passes through the atmosphere at a speed greater than the phase velocity of light in air. While the method has the disadvantage of a large momentum cut-off that limits the available statistics, it comes with negligible background contamination. Statistics are further reduced by the fact that data cannot be collected in daylight. The main obstacle to broad acceptance of the method is, however, the cost of dedicated Cherenkov telescopes.

A different application of the Cherenkov effect is exploited by other teams as a particle identification mechanism for background discrimination, using water (or other suitable media) to produce Cherenkov light. This technique, combined with one of the detection methods described in the preceding subsections, is a relatively cost-effective method to increase the signal-to-background ratio, appropriate for large-volume experimental setups.

[4] Acronym for Oscillation Project with Emulsion-tRacking Apparatus.

2.3. IMAGING METHODS

The raw data observed by the detectors consist of a collection of 'hits' (i.e., localized signals) that are interpreted as crossings of the muons with the sensitive elements of the detectors, whose positions are connected into 'tracks' (i.e., reconstructed trajectories of individual muons).

The following subsections explain how the directions of large samples of tracks can be used, on a statistical basis, for imaging purposes.

2.3.1. 2D imaging in muography

In most applications of muography, both the size of the object to be imaged and its distance from the point of observation are orders of magnitude larger than the size of the detector. In these conditions, the outcome of a single detector (irrespective of having a classical hodoscope or borehole layout) is intrinsically bi-dimensional, as the only property of importance for the observed tracks is their direction of arrival (i.e., the crossing point of the muon through the front of the detector brings no useful information). A direction in space can be parameterized by only two numbers, typically the zenith (θ) and azimuth (ϕ) angles.

The muon rate measured as a function of those two angles, $R(\theta,\phi)$, can be used to extract a 2D opacity map. To do so, it is necessary to compare the observed rate with the 'free sky' (FS) rate, $R_{FS}(\theta,\phi)$ (i.e., the muon rate that would be observed in the absence of the object to be imaged), to extract the effective transmission map, $T(\theta,\phi)$, by $T(\theta,\phi) = R(\theta,\phi)/R_{FS}(\theta,\phi)$.

Ideally, the determination of $R_{FS}(\theta,\phi)$ needs to be such that all biases deriving from detector inefficiencies or modelling uncertainties cancel out in the ratio. This can be trivial when, for example, the detector can be rotated about the ϕ direction[5] so as to have no obstacle in its field of view while spanning the same θ range. In some other cases (e.g., see Fig. 2) a simple rotation would not permit unobstructed fields of view, but the same detector setup can take control data from a different location, for example at the Earth's surface (to observe the free sky), or at a different location from where the field of view contains only precisely known density distributions.

While all the examples in the preceding paragraph assume that the detector can be moved and need separate data collection periods for the object of interest and the free sky[6], another solution is to use a portion of the field of view of the detector (in the very same dataset as used to study the object of interest) as a control region and extrapolate the free sky muon flux from that region to the rest of the (θ, ϕ) map. To do so, one has to correct for two important effects: the strong dependence of the muon flux on θ, and the acceptance effects that make the probability of reconstructing a muon's path dependent on its direction and entry point in the detector. For example, for a typical hodoscope configuration, the probability is greater close to its axis, while for a cylindrical borehole detector the cylindrical axis is a blind spot. The first effect can be

[5] Small differences in muon flux between different ϕ orientations are present, due to the fact that more muons travel in an easterly direction than in a westerly direction ('the east–west effect') caused by the effect of the Earth's magnetic field on the positively charged primary cosmic rays entering the atmosphere. This is, however, a small effect that can be safely neglected in muography applications.

[6] Those expedients make an important implicit assumption: that data taken at a certain moment in time are exactly comparable with those taken at different times with a different detector orientation or location. Several periodic and aperiodic time-dependent effects on the muon rate and spectrum exist on a variety of time scales (ranging from within a day to across a decade) due, e.g., to the effect of temperature on the atmospheric density and to solar activity. These effects are usually neglected.

corrected by the use of muon flux simulations or data from other experiments, while the second demands a detailed detector efficiency map as a function of (θ, ϕ). When at least two identical hodoscopes are available, one of them can be oriented towards the free sky to provide $R_{FS}(\theta,\phi)$, while simultaneously taking data in the same θ range as the other. This avoids any bias from the modelling of the muon flux and time-dependent effects, but local detector inefficiencies of an instrumental nature would not cancel out and still need to be accurately measured. The solution chosen by the MURAVES experiment (see Section 5) is to alternately move one of their three hodoscopes to a backward-pointing position [22].

The spatial resolution achievable in a 2D opacity map depends on the angular resolution (which is the same for both θ and ϕ) of the tracking device, which in turn depends on the spatial resolution of the detector layers. Muography trackers typically have angular resolutions, Δθ and Δϕ, ranging from a few to a few tens of milliradians. Where the tracker size is insignificant compared to target dimensions, spatial uncertainty, Δr, for a structure at distance L can be derived from the angular resolution by $\Delta r = L\Delta\theta$. For applications studying the internal structures of volcanoes (see Section 5), typically, $L \approx 1$ km and $\Delta\theta \approx 30$ mrad, so that $\Delta r \approx 30$ m. This performance of muography is better than many standard geophysical methods. A limiting factor on the resolution, for such very large objects, is the multiple Coulomb scattering suffered by muons before being recorded by the detector, as described in Section 2.1.2. The effect builds up as muons progressively lose energy through matter. For this reason, it is customary for hodoscopes that are used to study very large structures to employ large quantities of Pb or other dense materials as 'momentum filters' within the detector set-up itself to ensure that low-momentum muons are absorbed before generating hits in the layers of the detector. The optimal thickness of this kind of passive material is calculated case by case based on the trade-off between resolution and statistics.

2.3.2. 3D imaging in muography

To achieve 3D imaging with muography, data from more than one viewpoint can be processed, either observing the object simultaneously from different points of view, or by sequential measurements after moving one tracker (Fig. 8). The latter approach minimizes cost but assumes there is no dynamic process that would affect the target on the measurement timescale, and that the detector stability and environmental conditions remain constant or very similar.

As mentioned before, imaging with a single muography set-up is intrinsically two dimensional. However, a back-projection algorithm has been developed [23] to derive 3D information from a single observation point when the detector size is not negligible compared to the distance and size of the target object (cf. the case described in Section 2.3.1). Different sides of the detector see the target from different angles, providing a stereoscopic view of the target. Whereas 2D muography uses only the information on the direction of arrival of muons, this approach also measures the impact points on the detector. Although the resolution along the rock depth is modest, and only suitable for high-contrast uses (e.g., finding a void surrounded by rock), this back-projection algorithm needs only a single measurement site, in contrast to the aforementioned 3D methods, which can be impractical/impossible at some locations.

Another way to achieve 3D imaging using a single muon detector is to combine muography with additional data from other geophysical survey methods, such as gravimetry, seismotomography, or geoelectric data. Ground penetrating radars and magnetometers are popular tools in near-surface surveys, including archaeology. All these methods are standard in geosciences but are typically affected by their reliance on model assumptions to solve degeneracies (i.e., existence of non-unique solutions) of their strongly non-linear inversion problems. Their combination with muography naturally breaks those degeneracies, as muography is intrinsically directional.

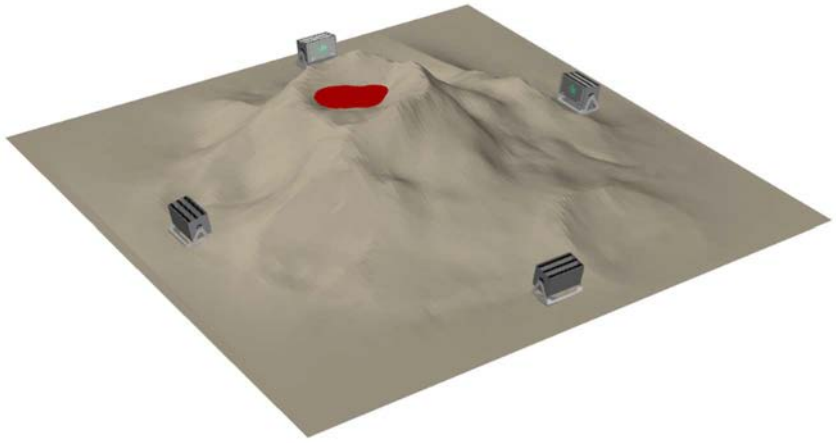

FIG. 8. Although the muography method is intrinsically bi-dimensional, 3D imaging can be easily achieved by combining data from two or more points of view (reproduced from Ref. [2] with permission courtesy of Elsevier).

2.3.3. 3D imaging in muon scattering tomography

As stated before, three-dimensional imaging is a natural output of the MST method. Muon trajectories are reconstructed in three-dimensional space in the two trackers and extrapolated within the volume occupied by the object of interest, which is divided into 'voxels' (i.e., discrete volumes assumed to be of homogeneous material composition). Some of the most common image reconstruction methods developed in the MST literature are described below.

A simple but fairly effective imaging method, named Point of Closest Approach (POCA), relies on the assumption that either each muon scatters only once within the volume between the two trackers, or that all scattering interactions of a given muon are confined within a single voxel. The muon trajectories measured by the two trackers are extrapolated up to their point of closest approach, as the name implies, and the angle between the two trajectories is recorded for the corresponding voxel. The root-mean-square of the scattering angle distribution for a given voxel is then related to the properties of the material in that voxel.

The trajectory of a cosmic ray muon inside the inspected volume is unknown. Instead, only an incoming track and an outgoing track of the particle are measured and an approximation of the particle's path inside the inspected volume based on these measurements is needed. Commonly, both the incoming and the outgoing track are approximated as straight lines. These two straight lines in general do not intersect in 3D space. Instead, their closest approach is used as the scattering vertex. The distance of closest approach represents the zone where the muon was scattered, and the point of the closest approach (POCA), which is the middle of the line of the closest approach, represents an approximate location of the scattering point. These concepts are illustrated in Fig. 9. The simple – and popular because of its simplicity – approach to image reconstruction is to assign the scattering signal based on the scattering angle measurement to

the voxel that contains the POCA. While this approach works very well in simple cases, it is only as good as the simplified assumption of a single scattering point for multiple Coulomb scattering. It can help to discover the presence of a strong scatterer, for example, a shielded chunk of a special nuclear material. It is much less efficient in understanding the material properties of extended objects.

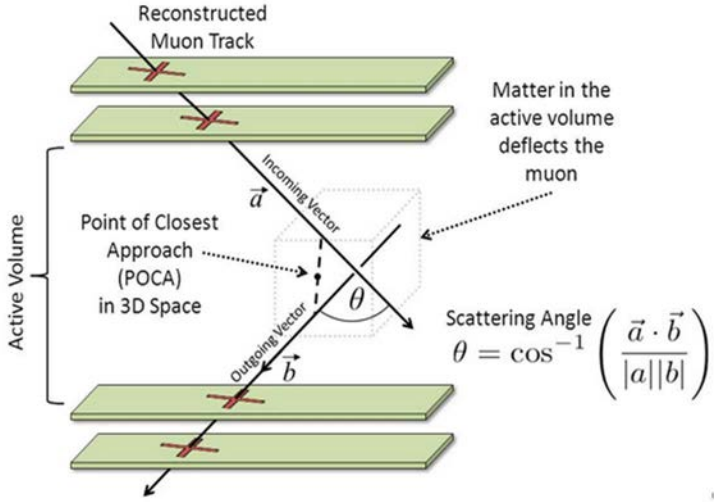

FIG. 9. Concept of the POCA in muon tomography image reconstruction (courtesy of K. Borozdin, Decision Sciences).

The main deficiency of POCA based methods is the misplacement of the measured signal in space. Albeit somewhat crude, the single-scattering approximation yields very good results in many cases (especially for objects that are not very large) with 3D spatial resolution of a few mm^3. One well known way to overcome this is to use the power of tomography to allocate the signal properly by using information coming from different directions from multiple probes. As more information is collected, the scattering can be assigned to the regions of the image where the scattering events really take place. This idea is implemented mathematically in the maximum likelihood / expectation maximization (MLEM) technique [24]. It is an iterative technique that converges to the right solution through a series of images, iteratively representing the distribution of the matter in space that is more likely to cause the observed scattering of the muons in the volume. This technique is significantly more complicated than POCA and requires a more powerful computing engine to converge to the solution in real time. Another issue with MLEM is its tendency to over-rely on any variation in data, including statistical fluctuations. This can be overcome with sufficiently long exposures, as any statistical fluctuations become small and negligible compared to the real signal, which can be recovered by MLEM and used for image reconstruction. However, in short scans, often required in practical situations, MLEM can become a mechanism for noise amplification, obscuring instead of revealing the real solution.

The choice of algorithm must be made to fit the requirements at hand for any given problem. Moreover, different problems demand different figures of merit for algorithm optimization, where the interests may be:

- The smallest observable difference in *Z* between different materials;
- The smallest spatially resolvable feature in the object;
- Minimizing the data collection time needed to reject a null hypothesis.

A common weakness of MST derives from the dependence of the scattering angle on muon momentum. Moreover, the absorption of muons by the object causes a selective bias as it also depends on muon momentum. These effects, usually corrected by means of simulations, induce some reliance on the modelling of the muon momentum spectrum, which is relatively poorly known, especially in the low-momentum regime. It would be ideal if the momentum of individual muons could be determined in situ to minimize model dependence. Use of a magnetic spectrometer would be impractical or too expensive for most applications, but some MST setups are designed such to give indirect access to momentum. One can add a Fe or Pb slab of well-known dimensions into the system as a 'momentum filter' (Section 2.3.1) whose purpose is to cause further muon scattering. One can then exploit the knowledge of the size and material of the slab, and the scattering angle distribution after the target as measured in the bottom part of the apparatus, to extract the average momentum distribution. One variant of this method can also take advantage of the strong correlation between momentum and the goodness-of-fit of the muon track to a linear trajectory [25].

Other algorithms, as well as POCA and MLEM variants, are under development, including machine learning (see Section 8.3.4). Some variants also combine scattering information with absorption. While some targets are small enough to be scanned in a single measurement, nuclear casks (see Section 8), given their size, require multiple measurements. This can, however, bring additional benefits; e.g., resolving ambiguities and improving resolution.

3. CIVIL ENGINEERING AND UNDERGROUND APPLICATIONS

This Section illustrates applications of muon imaging to civil engineering and the modern built environment via a variety of case studies.

3.1. IMAGING OF CONCRETE STRUCTURES

One potential application of muon imaging concerns the in-situ investigation of concrete structures. Defects within concrete structures can result in weakening of the entire building with potentially major consequences in the mid or long term. Due to the thickness of some structures, and the impracticalities involved in transporting them for laboratory investigation, muon imaging via a portable detection system offers an interesting and appealing alternative and also facilitates large area scanning. This possibility was recently tested at CEA-Saclay with a dedicated concrete slab of dimension $2 \times 1 \times 0.5$ m^3 which was scanned in several muon imaging modes as shown in Fig. 10.

The MST mode of data collection, which requires the volume of interest to be sandwiched between two detector systems, is usually the method of choice for low opacity systems but suffers in this application from an important blurring of the reconstructed image from multiple scattering within the slab.

Furthermore, the strict requirements on the relative alignment of the upper and lower detector systems on both sides of the structure is also an obstacle for large scale deployment in the real world. Muography, which is a natural choice for very large structures, is also limited in this application, as it implicitly selects the upper range of the muon momentum spectrum, which is populated only by a small fraction of the muon distribution.

The third imaging method, and main focus of this study, is the rarely used ‘absorption mode’, which is particularly sensitive to low energy muons. In this mode, the detection system consists of a muon telescope placed upstream of the structure, with an additional layer downstream acting as a veto. The muon image is then reconstructed with muons whose extrapolated direction is within the acceptance of the downstream layer, but which are not detected by it. As in the case of MST, the absorption mode requires instruments on both sides of the slab. However, the alignment constraints are much less onerous than for MST, and large areas can be scanned by simply moving both parts of the detector system. Moreover, the downstream veto layer does not need any particular capability in terms of spatial resolution, so, in principle, it can be built from large and relatively cheap scintillators to increase the scanning area.

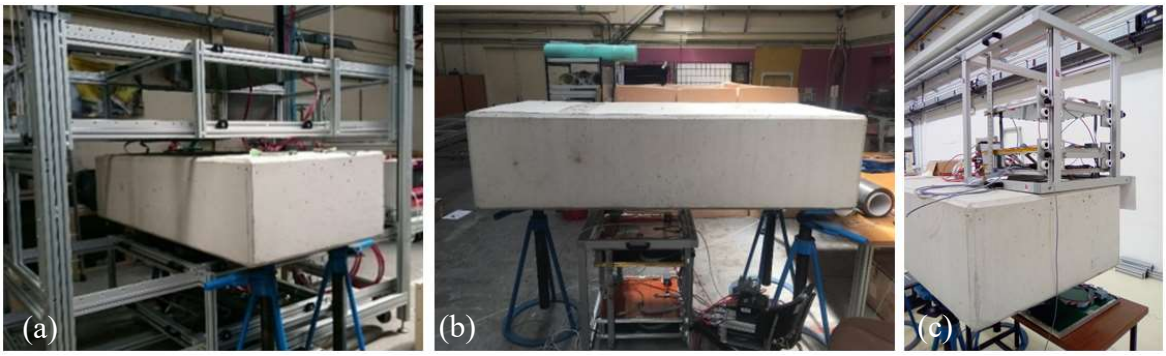

FIG. 10. A concrete slab tested with muon instruments in (a) scattering, (b) transmission and (c) absorption modes (courtesy of S. Procureur, CEA-Saclay).

In the configuration used at CEA-Saclay, the muon telescope consisted of three 50 × 50 cm² Micromegas detectors [26] with a 2D readout, with a fourth identical detector for the downstream veto. The concrete slab was purposefully made with several defects: in particular, two voids, one of size 150 mm and the other of 100 mm. These two defects were placed on two corners of the slab on the same side (in length), but invisible from the outside to ensure a blind analysis.

Data were first accumulated in two opposite corners (for 8 hours each), to make sure that at least one measurement is made on a region without defects. The two images, 'M1' and 'M2', were first smoothened to mitigate statistical fluctuations, as follows: for each position (x, y) in the image, muons are counted in a square of side length S, with S tuned so as to maximize the significance of the deviation from the null hypothesis. Finally, these muon counts, integrated around each position (x, y), are divided between image M1 and image M2. This procedure creates a strong statistical correlation between neighbouring pixels. The resulting ratio image (M1/M2) is found to yield an accurate estimation of the size of the defect.

The result is shown in Fig. 11a. A clear excess at about the 8σ level[7] appears, which indicates that the defect is in the corner imaged by M2. To confirm this result, a second acquisition of 59 hours was taken in the same corner, with a detector position shifted by 170 mm along y with respect to the first measurement. The analysis reveals an excess of greater than 14σ shifted by 170 mm (Fig. 11b). An estimate of the size of the void indicates it to be of order 200 mm in extent, which favours its interpretation as the larger void.

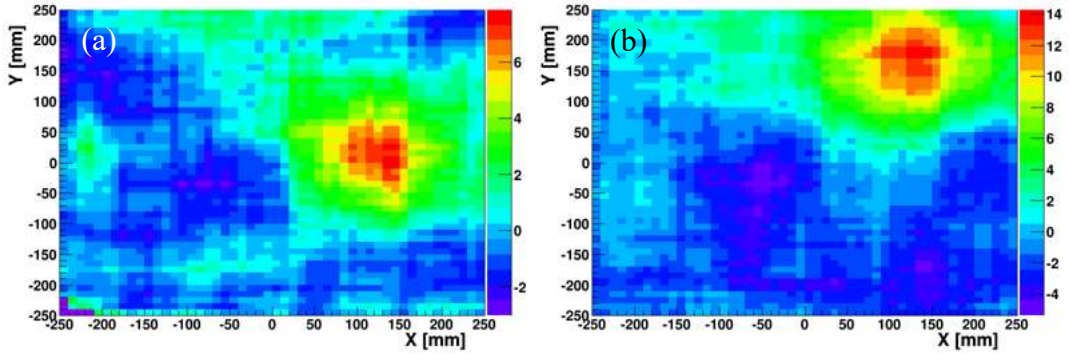

FIG. 11. Image of a concrete slab using muon absorption (a) before and (b) after shift of the detector position (courtesy of S. Procureur, CEA-Saclay).

Once this first void was identified, the corner hosting the second, smaller void could be determined unambiguously. An acquisition of 21 hours led to a 6σ feature, with a size estimate of 150 mm, proving that this void was indeed smaller. Several simulations were performed in parallel with the CRY cosmic muon shower generator [27] to estimate the mean time to reach a 5σ level detection for these two voids. The estimates, 3 and 10.5 hours respectively, are comparable to the experimental measurements. These times may appear long for practical implementation but can be significantly decreased by the use of larger detection systems (both for the telescope and for the veto). According to simulations, both these times could be approximately halved with a 1m² instrument.

[7] In physics research, it is customary to indicate the level of disagreement with a null hypothesis (in this case, a perfectly homogeneous concrete volume) by converting the p-value into an equivalent number of Gaussian standard deviations (popularly indicated by the symbol σ).

3.2. IMAGING OF REINFORCED CONCRETE STRUCTURES TYPICAL FOR BRIDGES

Roads and bridges are key infrastructures all around the world. Transport and trade rely on them, and they enable individual mobility. Like other infrastructure, bridges are subject to aging that can lead to safety issues and accidents. The collapse of the Morandi Bridge in Genoa in August 2018 has attracted much attention. However, this catastrophe is only one example for many potential accidents that might happen in the future if underlying issues are not addressed. Large numbers of bridges in, e.g., Germany[8] and France, are in no better state than the Morandi Bridge [28]. The monitoring of bridges to carry out maintenance in time to avoid these accidents relies on non-destructive testing (NDT). Typical techniques of NDT for bridges include ground-penetrating radar, ultrasound and X-rays.

In 2019, the German Bundesanstalt für Materialforschung und –prüfung in Berlin and the University of Glasgow carried out a series of tests to investigate muon tomography as a method for in-situ bridge inspections. To this end, the same reinforced concrete reference block ('Radarplatte') was imaged by muon tomography using the Lynkeos[9] Muon Imaging System (MIS) at the University of Glasgow, as well as by radar, ultrasound, and X-ray laminography at the German Bundesanstalt für Materialforschung und –prüfung.

A $1.2 \times 1.2 \times 0.2$ m^3 object, called the 'Radarplatte', was made for testing and development purposes. Four different targets (Fig. 12) typical of reinforced concrete structures as found, e.g., in bridges, were placed within it. Reinforcement bar mats covering about half the area and overlapping by about 25% were placed near the top and the back of the Radarplatte and covered by about 30 mm of concrete. The upper mat was of 150 mm mesh and the mat at the back was of 100 mm mesh. Between these mats, a tendon duct (65 mm diameter) was placed and covered with 90 mm of concrete. A Styrofoam block (50 mm thick) was used to simulate a void and was placed at the bottom of the Radarplatte.

The MIS used for the investigation consists of four detector modules each containing two orthogonal layers of scintillating fibres. The four detector modules are split into two sets above and two sets below the object: the upper ones reconstruct incident muon tracks and the lower ones reconstruct the outgoing, scattered tracks (Fig. 13). Each module has an active area of 1×1 m^2. The limiting factor for the horizontal resolution of the MIS is the 2 mm diameter of the detectors' scintillating fibres, which are triangularly distributed in two sublayers. This permits an effective resolution of better than 2 mm where muons pass through neighbouring fibres. The angular acceptance of the detector is limited to tracks that are nearly vertical. This restricts the vertical resolution of the reconstructed image to ca. 4 cm. The volume between the top and bottom detectors is divided into voxels of typical size of $3.4 \times 3.4 \times 10$ mm^3. The tomographic image was reconstructed from 23 million tracks taken over 50 days of continuous data collection.

Radar data from a guiding radar antenna with a centre frequency of 2 GHz were recorded along lines 5 cm apart and parallel to the edges of the Radarplatte. Depth slices were generated at depths of 5, 12 and 17 cm, and each slice was averaged over 1 cm in the z-direction. The ultrasonic data were collected using an automated scanning system developed by the German Bundesanstalt für Materialforschung und –prüfung. A grid of 2×2 cm^2 was used and two data

[8] GERMAN ROAD RESEARCH INSTITUTE (BASt), Bridge Statistics (2020), https://www.bast.de/BASt_2017/DE/Statistik/Bruecken/Brueckenstatistik.pdf.
[9] http://www.lynkeos.co.uk

sets with orthogonal polarizations (*x* and *y*) were recorded. The InterSAFT software developed at University of Kassel [29] was used for data processing.

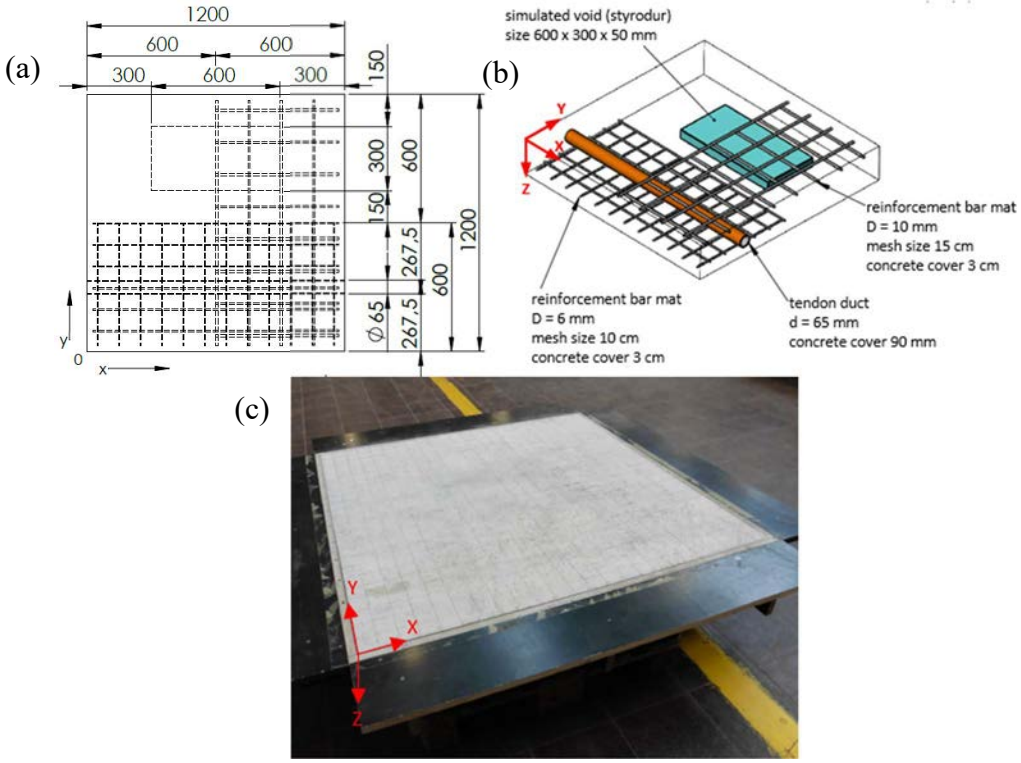

FIG. 12. The reference concrete block 'Radarplatte'. (a) Design top view, (b) perspective view, and (c) picture after concreting (courtesy of R. Kaiser, Lynkeos Technology Ltd).

FIG. 13. The 'Radarplatte' reinforced concrete block inside the Lynkeos MIS at the University of Glasgow (courtesy of R. Kaiser, Lynkeos Technology Ltd).

X-ray laminography data were collected using the HEXYTech equipment of the German Bundesanstalt für Materialforschung und –prüfung. The radiation source and detector are synchronously moved parallel to the stationary object. Several hundred positions of the X-ray source were typically used and transmitted X-rays were recorded by a detector. The

experimental setups, procedures and data analysis techniques used for all four comparative measurements are described in detail in Ref. [30].

Fig. 14 shows the results for muon tomography, radar, ultrasound and X-rays at 5 cm, 12 cm and 17 cm depth. These depths were selected because they correspond, respectively, to the embedded structures: thicker rebar grid, tendon duct, and combination of Styrofoam and thinner rebar grid.

3.2.1. Comparison of the results from different imaging techniques

X-ray laminography leads to the best imaging results. It shows the irregularities in the rebar grids and it is the only technique that resolves the structure of the tendon duct. However, the resolution of muon tomography clearly exceeds the resolution of ultrasound and of radar images for all structures, and also shows the irregularities in the rebar grids.

A closer inspection of the muon tomography images reveals some artefacts. Shadows of objects above and below the targeted depth slices are seen due to inherent limitations of the technology that result from the limited angular coverage (especially the geometrical acceptance of incident muons of between –30° and +30° with respect to the vertical). There is also a high-density band running vertically towards the left edge of all images, which represents a support structure that held the sample in position during measurement (Fig. 13) and partly shadowed it. The images' edges are noisier and more sensitive to misalignment, also due to limited acceptance of the system.

Comparison of muon tomography with X-ray laminography images shows similarities, such as shadowing effects from above and below, edge effects, different signature of low- and high-density objects. The resolution of the images as well the low noise level are distinct advantages of active X-ray technologies. Nevertheless, the quality of the muon tomography images is surprisingly good for a first ever experiment using a new, non-optimized technology.

Both radar and ultrasound image the Styrofoam 'void', but with lower resolution. Radar also clearly detects the rebar grid, but the reconstructed thickness is about three times too large. The resolution of ultrasound is insufficient to image the rebar grid. The tendon duct is imaged as a horizontal void by radar and ultrasound. While muon and X-ray tomography show shadows of the tendon duct at 5 cm depth, this is not the case for radar and ultrasound. The same is true for the Styrofoam block at 5 cm and 12 cm, indicating that the strengths of radar and ultrasound lies in the depth measurement, while their horizontal resolution is clearly worse.

Only X-ray laminography and muon tomography image all structures within the Radarplatte and do so at the correct size. Currently, muon tomography does not match the resolution and noise level of X-ray methods. On the other hand, it does not require permits and radiation safety measures on site.

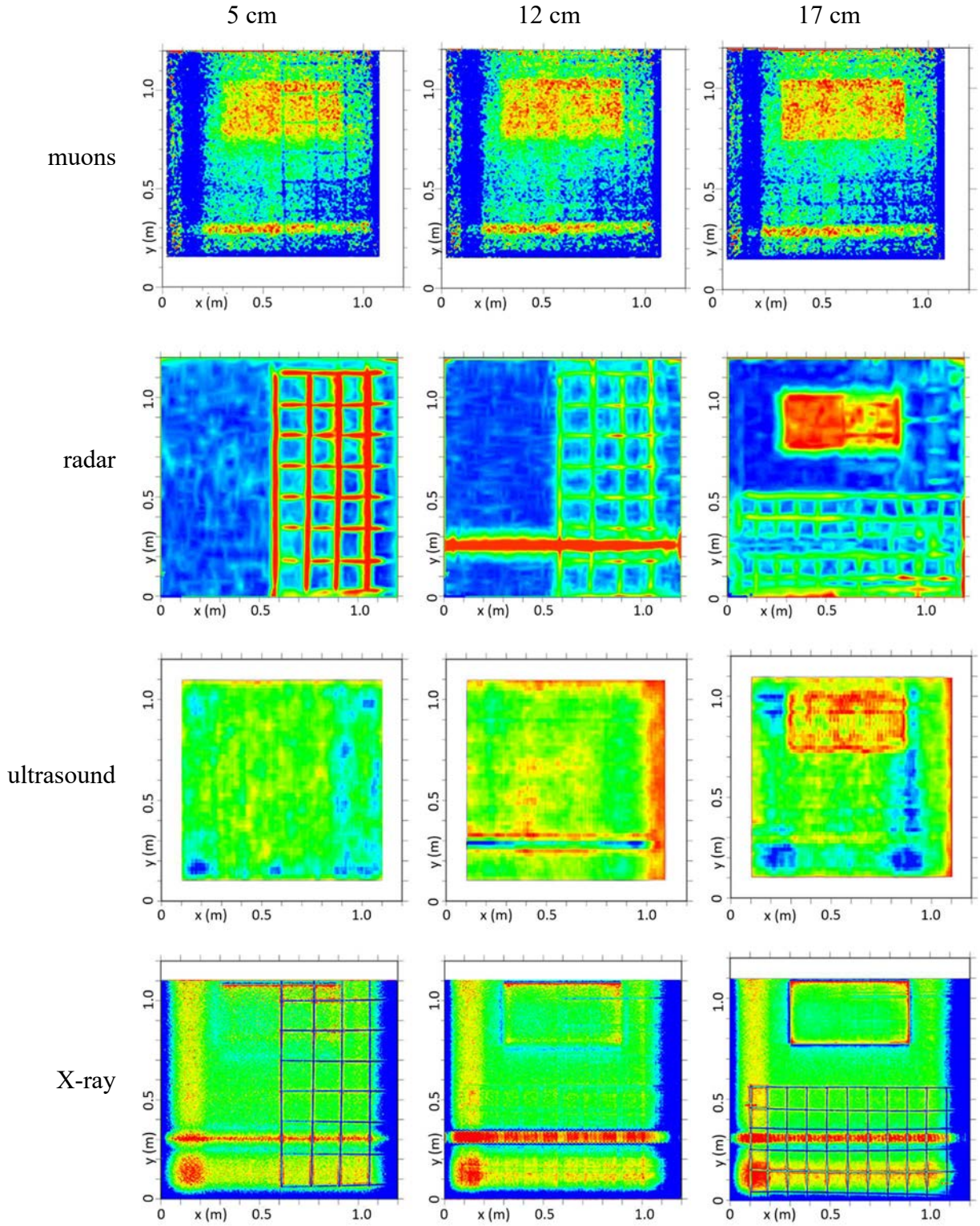

FIG. 14. Images of the Radarplatte test object different depths, taken with the four techniques (courtesy of R. Kaiser, Lynkeos Technology Ltd).

3.3. MONITORING OF AN HISTORICAL BUILDING

In high-energy physics, cosmic ray muons have been used for many years for detector alignment, and reconstructed tracks used to estimate the relative position and orientation of detector elements. A relatively new application for checking alignment in large mechanical equipment and for stability monitoring of historical buildings has been proposed [31–33].

Monte Carlo techniques were applied to study the feasibility of monitoring the structural alignment of a mechanical press [31]. Uncertainty values obtained were comparable to those of existing alignment methods. The major disadvantage of muon detection-based alignment techniques, in that case, was the limited flux at the Earth's surface, and the wide angular distribution around the zenith direction. Therefore, rather large acquisition times are required to attain low statistical uncertainties.

For certain alignment measurements, flux limitation is not a limiting criterion; e.g., monitoring of modern buildings, towers or historical palaces. The relative shift between different parts of the building usually occurs on a very long timescale. In particular, historical buildings usually undergo slow deformation processes that require precision monitoring on over a time scale of months or even years.

Another limiting feature of the tomographic technique is the stochastic nature of the deviations of the muon trajectories, a result of the angular scattering suffered by muons traversing materials. Therefore, statistical distributions are used to extract by statistical inference the quantities of interest, and a large number of events are required for sufficient precision.

On the other hand, the high penetration of cosmic muons can overcome the problem of physical and optical separation structures, such as walls or floors, and still measure relative position. Indeed, cosmic ray muons suffer only small trajectory deviations when crossing walls or floors of buildings. Current commercial systems, such as laser scanners and theodolites, require optical transparency between different reference points. As an entire building is continuously irradiated by muons, over angular ranges of several tens of degrees from the zenith, muon detectors distributed across multiple positions in a building could enable simultaneous monitoring of an entire building’s stability.

The principle behind a system for monitoring the stability of buildings through the detection of cosmic ray muons can be summarised in the following steps:

(i) Tracking of the cosmic ray muons in two positions within the building, one vertically above the other;
(ii) Extrapolation of the tracks to an intermediate common plane and comparison of their intercepts and inclinations;
(iii) Monitoring of the system over a given time interval.

As an example, the monitoring system proposed in Ref. [34] consists of two telescopes, one above the other, inside a building. Each muon telescope is comprised of a set of three detection planes/layers, each 4×4 m^2 in area and separated by 5 m, and is able to measure the position of the crossing cosmic ray muons. Both telescopes, referred to as ‘lower’ and ‘upper’ telescopes, are mechanically anchored to the building structure, and can be placed in different parts of the building. Their initial positions and inclinations are measured with standard instrumentation such as a mechanical inclinometer. For each cosmic ray muon, the points of passage through the three layers of a telescope are fitted with a straight line and this is done for

both telescopes. From the reconstruction of a sample of cosmic muons, the relative position x_D (or similarly y_D) and the relative inclination θ_D between the two reference frames of the two telescopes can be calculated. Having measured (x_D, θ_D) at a given 'reference' time each successive measurement of the same quantities provides an indication of the stability of the relative position/inclination of the two telescopes. Since the telescopes are anchored to the building, relative movement implies structural deformation.

An historical building, the Palazzo della Loggia in Brescia, was studied to determine the performance to be expected from such an approach. The palace roof had been monitored for 10 years by measuring the elongation of metallic wires across the structure. Seasonal deformations (a few mm) superimposed on a general collapse of about 1 mm per year were detected.

Masonry structures and the structure and composition of the two telescopes were modelled using GEANT4 [35]. The proposed muon monitoring system was simulated and compared to that of conventional mechanical monitoring systems. Three configurations were simulated, with the two telescopes positioned vertically one above the other at different distances: Δz = 350 cm, Δz = 880 cm and Δz = 1300 cm. Due to differences in the geometrical acceptances of these configurations and the angular distribution of the cosmic muons, in order to collect the same statistics, the time intervals were varied: the closer the telescopes, the shorter the time required. The collection and reconstruction of 500 muon tracks corresponds to a data collection period of approximately 1.5 h, 7.5 h and 16 h for the three Δz configurations, respectively, assuming 100% muon detection efficiency. Resolution of the relative position x_D and inclination θ_D of the two telescopes assuming detection efficiency of 30% are summarised in Fig. 15a (see Ref. [11] for details). The system can detect displacements of ~0.3 mm, ~1.3 mm and ~3 mm and misalignments of ~0.3 mrad, ~0.6 mrad and ~0.8 mrad within a data collection period of 24 hours. Simulations demonstrated that the displacement monitoring of the three inspected points in the Palazzo della Loggia's roof through the reconstruction of cosmic ray muons could provide the required resolution and with a timescale characteristic of known deformation phenomena. To estimate the error when measuring displacements and misalignments under different conditions, a dedicated Monte Carlo simulation would be needed.

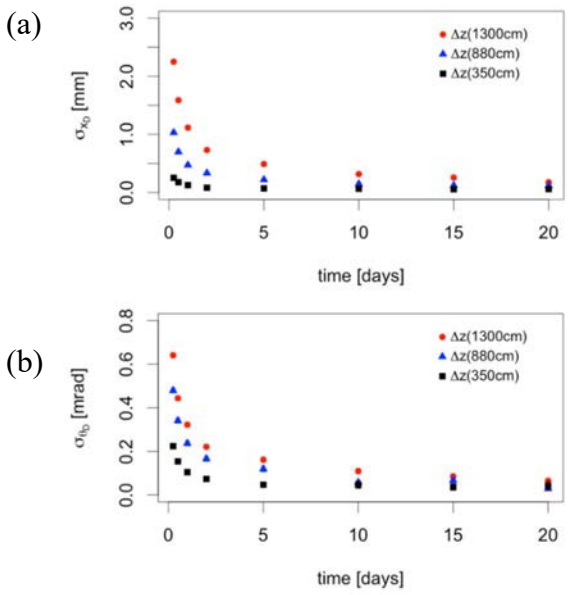

FIG. 15. (a) Simulated resolution versus data collection time of the relative position x_D and (b) inclination θ_D of the two telescopes for three configurations (reproduced from Ref. [34] with permission courtesy of Elsevier).

3.4. IMAGING OF RAILWAY TUNNELS

Much of the railway infrastructure in the United Kingdom dates back to the Victorian era when there was a rapid expansion in the railways, particularly between 1850 and 1900. During this period, many railway tunnels were built. In order to accelerate tunnel construction, vertical shafts from the surface were often used. After tunnel completion, the construction shafts were capped at the surface and tunnel roof with little sign of their presence. The locations of these now concealed shafts were often not recorded or have been lost in the 150 years or more between construction and the present day.

If unmanaged, these 'hidden shafts' are an ongoing hazard to the train-going public and local communities. Examples of accidents caused by these unseen hazards include:

- The Clifton Hall tunnel shaft collapse, in 1953, in Swinton, Greater Manchester, when three semi-detached houses collapsed into a hidden shaft, killing five people [36];
- A shaft collapse above the Strood and Higham railway tunnel in December 1999 caused the derailment of four carriages; the destabilised ground collapsed again six months later. The tunnel was closed for a month and ongoing disruption lasted a year.

Muography is a suitable tool to identify such hidden shafts. In summer 2018, a team from the Universities of Sheffield, St Mary's and Durham were granted access to a disused railway tunnel at Alfreton in the UK. This tunnel has three full-height open construction shafts that run all the way from the tunnel to the surface, so this is an ideal location to perform a 'proof of principle' experiment.

A cosmic ray muon telescope with two horizontal layers of EJ-200 plastic scintillator was constructed. The upper layer has six independent rectangular bar detectors ($90 \times 15 \times 4$ cm^3), and the lower layer has three independent square paddle detectors ($30 \times 30 \times 4$ cm^3). Within each layer, detectors are placed with their longest side along the tunnel's width and their shortest side vertical. Each paddle/bar is coupled to a photomultiplier tube. With the top layer fixed 76 cm above the bottom layer, a 100° field of view along the tunnel axis, and a 76° field of view along its width are enabled. The telescope was designed to fit inside a Ford Transit van and was capable of running for 50 hours from a single charge of a rechargeable battery.

Prior to deploying this instrumentation in the tunnel, a series of simulations assuming the detector configuration described above were conducted to provide estimates of significance as a function of overburden and run time as seen in Fig. 16. These simulations, coupled with information on the tunnel overburden (average ~30 m) from previous surveys of the tunnel, e.g., with light detection and ranging (LIDAR), indicated that short runs, of order 20–30 minutes at each point, would be sufficient to achieve a high level of statistical significance between open shaft and no shaft.

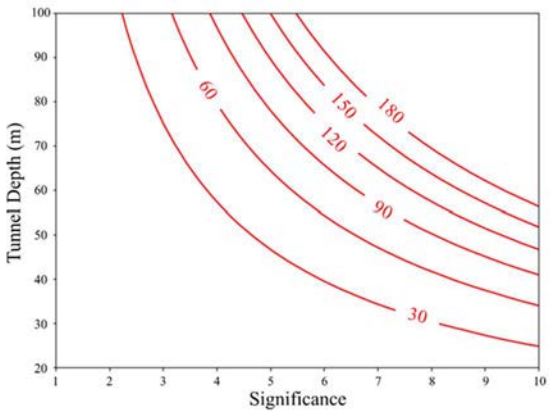

FIG. 16. Significance, in number of standard deviations between the open shaft and no shaft hypotheses, as a function of tunnel depth for different run times, in minutes (red numbers on curves), as derived from simulations (courtesy of L. Thompson, University of Sheffield).

Data were taken along the full ~800 m tunnel at 5 m intervals, and data collection runs were either 20 or 30 minutes in duration. Data from the full scan of the tunnel are shown in Fig. 17, which shows the muon flux rate as a function of distance along the tunnel.

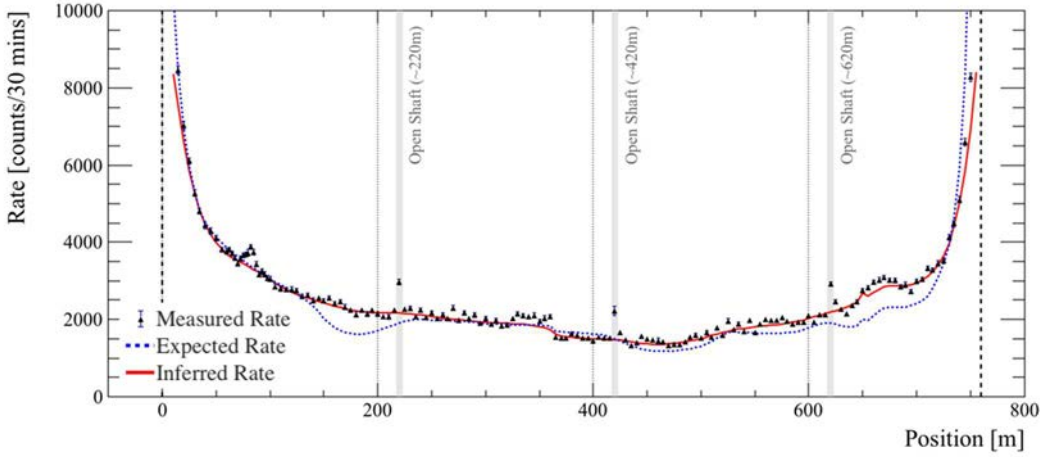

FIG. 17. Comparison of the observed muon flux rate with both the expected (derived from topographical information) and inferred rates (courtesy of L. Thompson, University of Sheffield).

Fig. 18 shows the observed rate compared with the 'expected rate', which is the rate predicted by simulations incorporating measurements made of the tunnel overburden by independent surveying methods. Given the configuration of the instrumentation, even directly beneath a void, the field of view always contains some angular bins which do not contain that void. Advantage is taken of those bins as redundant data that can also be used to estimate the overburden; this is reported in the 'inferred rate'. The agreement between the empirical and inferred rate data is generally good. As expected, there are significant deviations at the open shafts (Fig. 18b) where the difference between observed and inferred rates exceeds 10σ. Also visible in Fig. 18a is a clear anomaly around the 80 m position. A full discussion of the results can be found in Ref. [37].

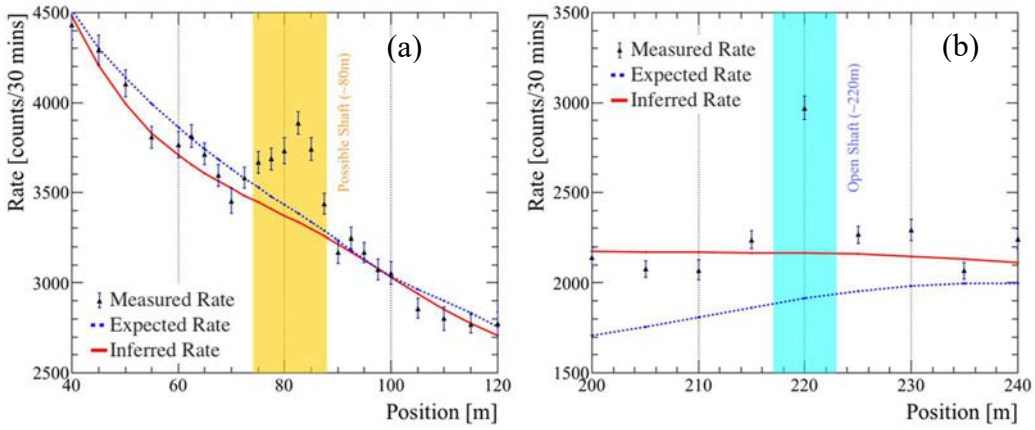

FIG. 18. Comparison of the observed muon flux rate with the expected and inferred rates at (a) 80 m and (b) 220 m, under an open shaft (courtesy of L. Thompson, University of Sheffield).

In late 2018, these results were reported back to the UK's rail authority, Network Rail. At this time, Network Rail shared concerns of a hidden void at the 80-m position, which had not been provided at the time of the original muon tomography survey. Subsequently, the team were contracted to perform a second series of measurements to take further data around this area of interest and, if possible, estimate the physical features of the void.

In summer 2019, the team subsequently collected data for four days with the original system and with an additional system based on tubes of liquid scintillator and photomultiplier tubes, that offered a finer granularity (see Section 2.2.3). Data were taken with fine binning both parallel and perpendicular to the tunnel axis in order to provide 2D imaging of the suspected void. Results from this second field survey are given in Fig. 19. These new data were able to accurately measure the position of the hidden void and its extent (~3.5 m in diameter). Furthermore, the muon flux rate observed, when compared with simulations, indicate that, at 1σ confidence, there is the equivalent of only 5 m of rock above the tunnel lining, indicating that the hidden shaft may be almost a full-height void. Since these activities the university teams have spun-out a company[10] and have been contracted by Network Rail to image, to date, a further three in-service railway tunnels.

In summary, muon attenuation tomography has proven to be a powerful tool to identify and measure density anomalies in critical civil infrastructure.

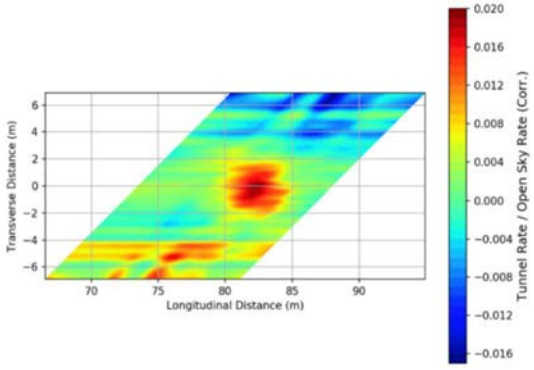

FIG. 19. Two-dimensional scan of the 80-m anomaly (courtesy of Geoptic Infrastructure Imaging Ltd[10]).

[10] http://www.geoptic.co.uk

3.5. SINKHOLE EARLY WARNING SYSTEM

A major geotechnical problem globally is the presence of sinkholes, which are invisible and carry great potential risks of catastrophic failure and collapse, often with the potential for loss of life. Muon imaging near critical infrastructure can be used to monitor the surrounding subsurface to provide an early alarm of the creation of a sinkhole.

Sinkhole creation usually begins with the dissolution of a layer of salt or limestone underground. Slowly over time, the cavity grows laterally, propagating upwards to form wide underground chambers with spans that can reach metres to tens of metres with a thin roof comprised of weak and poorly cemented sediments. Once the opening span induces tensile stresses on the thin roof layer which it cannot sustain, the roof may spontaneously rupture, leading to collapse and exposure of the large sinkhole underneath.

Sinkholes are present in many places in the world. In Europe, there are many locations where sinkholes have appeared, including southern Italy, southern France, Spain, central Greece, Germany (Hamburg) and Portugal. There are also large natural limestone sinkholes in South Wales and the Peak District in the UK, as well as in Florida in the USA. Examples of the dangers that sinkholes pose include:

- 20 cars swallowed, and two residential buildings evacuated due to a large sinkhole in the centre of Florence, Italy;
- A bus fell into a large sinkhole that opened up in the centre of Lisbon, Portugal.

A major geotechnical problem over the past two decades has been the collapse, without early warning, of large sinkholes in the soft sediments found along the western margins of the Dead Sea [38]. Water usage has led to the formation of a large number of sinkholes. This risk is a major infrastructure challenge. It affects people's safety and the economics associated with a major transportation route.

Fig. 20 depicts the results from simulations of the formation of sinkholes in progress that can be detected within a period of 3 days, 1 week and 2 weeks. The simulation shows that a muon imaging system can detect a cavity of diameter 15 m and height 10 m at a distance of 25 m before it opens to form a sinkhole. These results indicate that muon tomography is a suitable tool to provide an early warning system for sinkhole creation.

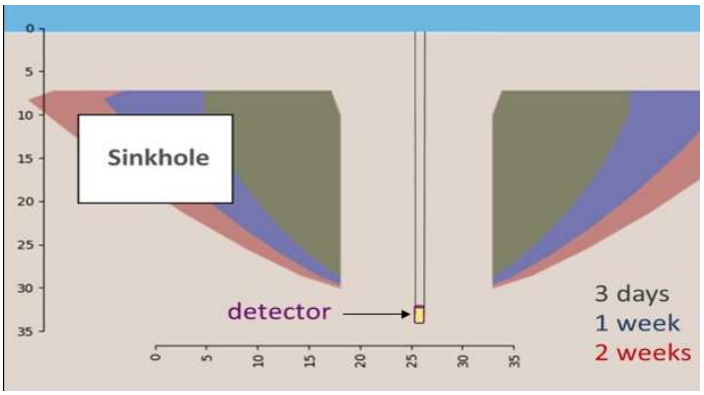

FIG. 20. Results from simulations of sinkhole detection using muon tomography. The shading of each region reflects the time required to detect the cavity (green = 3 days), (blue = 1 week), (red = 2 weeks).

3.6. TUNNEL BORING MACHINES

In spite of precautionary measures, the natural variability of geological features and instabilities induced by the driller may require expensive, real-time adaptations to drilling operations in tunnel boring projects.

The direct relationship between muon absorption and overburden density, makes muon tomography promising as a real-time density analysis method for the geology lying ahead of a tunnel-boring machine (TBM). A picture of such a TBM and an artistic view of the TBM digging operation are displayed in Fig. 21.

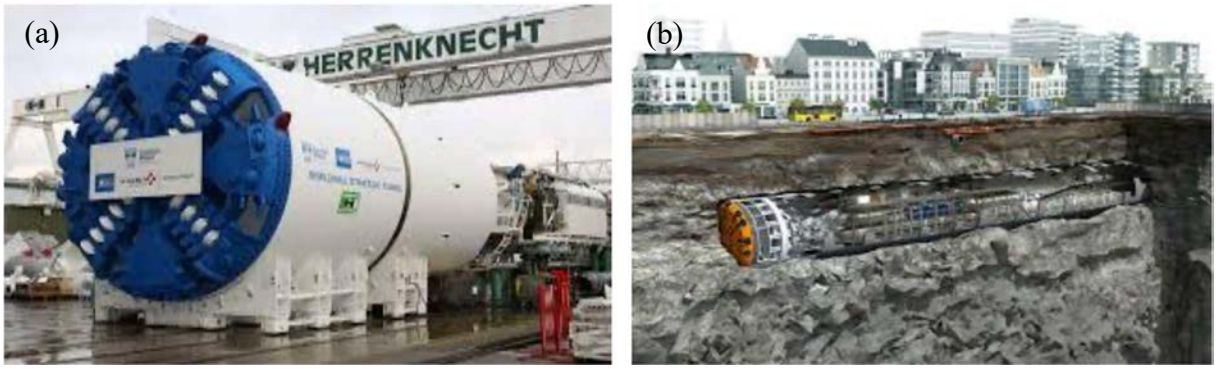

FIG. 21. (a) Picture of a Tunnel-boring Machine (TBM) of the Herrenknecht company during its construction phase, (b) Artistic view of a TBM while digging an urban tunnel (courtesy of J. Marteau, Institut de physique des deux infinis).

During the 'Grand Paris Express' subway system project, a muon telescope was used in two different experiments to test its applicability:

(i) Initially, it was placed alongside the TBM. Fig. 22(a) shows the muon telescope with its detection planes protected by a blue tarpaulin during this stage;
(ii) Within the TBM for the rest of the drilling operation (Fig. 23).

Data interpretation remains challenging as muon events are Poisson distributed through time. Flux can be estimated by averaging point events over a limited time window, but this may lead to misinterpretations of natural fluctuations of the muon events. Examples of apparent density reconstruction are given in Fig. 22(c/d).

Numerical routines were developed to model muon flux variations for different operational boring parameters through heterogenous densities: e.g., different trajectories, depths, and speeds. For case (i) above, good matches to experimental values were obtained. A blind analysis of the TBM's reconstructed time dependent position places strong constraints on the time and spatial resolution of the method. For case (ii), as the telescope advances at an irregular pace, the system collects muon flux crossing the same geological objects from different directions as a function of time, allowing 3D density estimates. An example of a 3D reconstruction using an inhomogeneous Poisson likelihood of the apparent density distribution of the ground is presented in Fig. 23. The algorithms for this particular reconstruction, removing systematic noise from the buildings, caves etc., are patented.

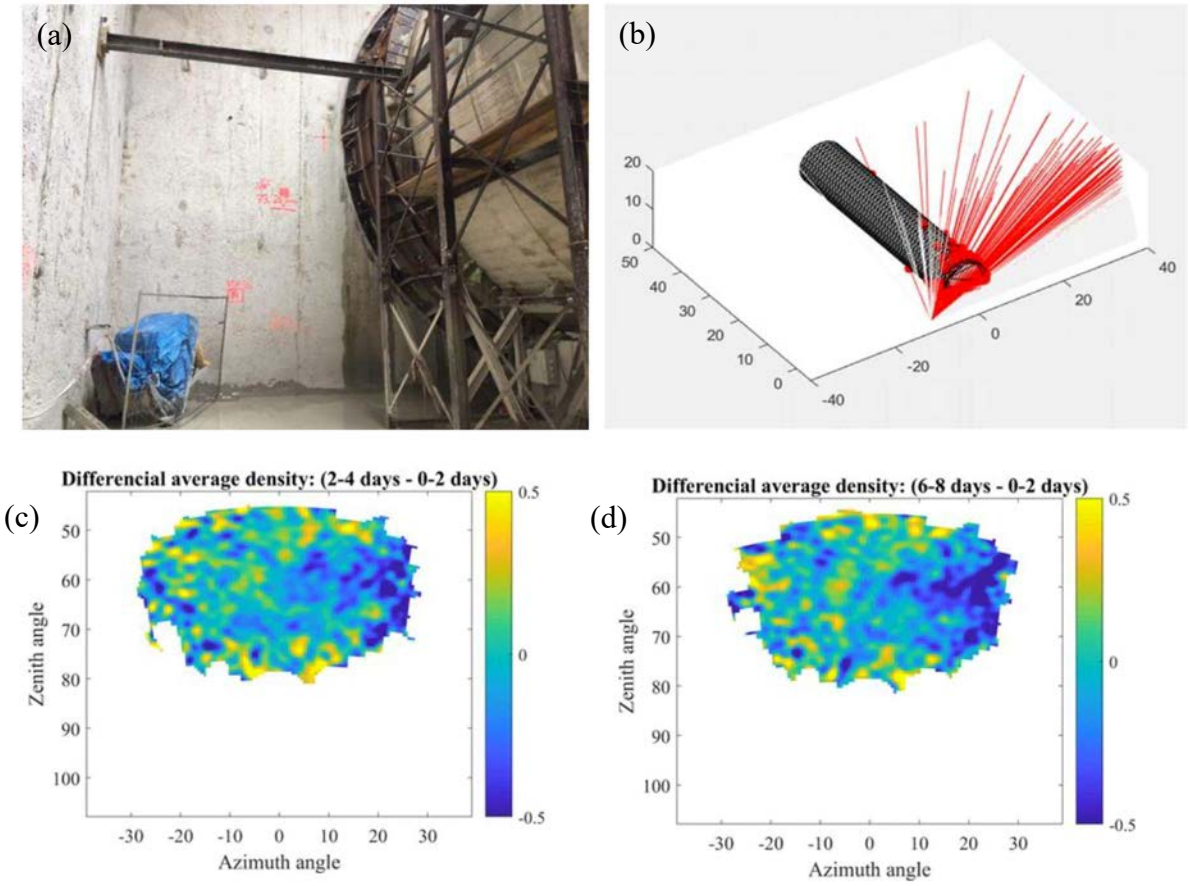

FIG. 22. (a) Picture of a muon detector in the assembly pit of a TBM of the 'Grand Paris Express' future line 15. (b) Muon trajectories within the muon detector acceptance. Apparent density reconstructed on a 2-day time average, 4 days after the TBM started drilling (c) and 8 days after the start (d). The blue colour scale corresponds to a negative density anomaly (tunnel void) (courtesy of J. Marteau, Institut de physique des deux infinis).

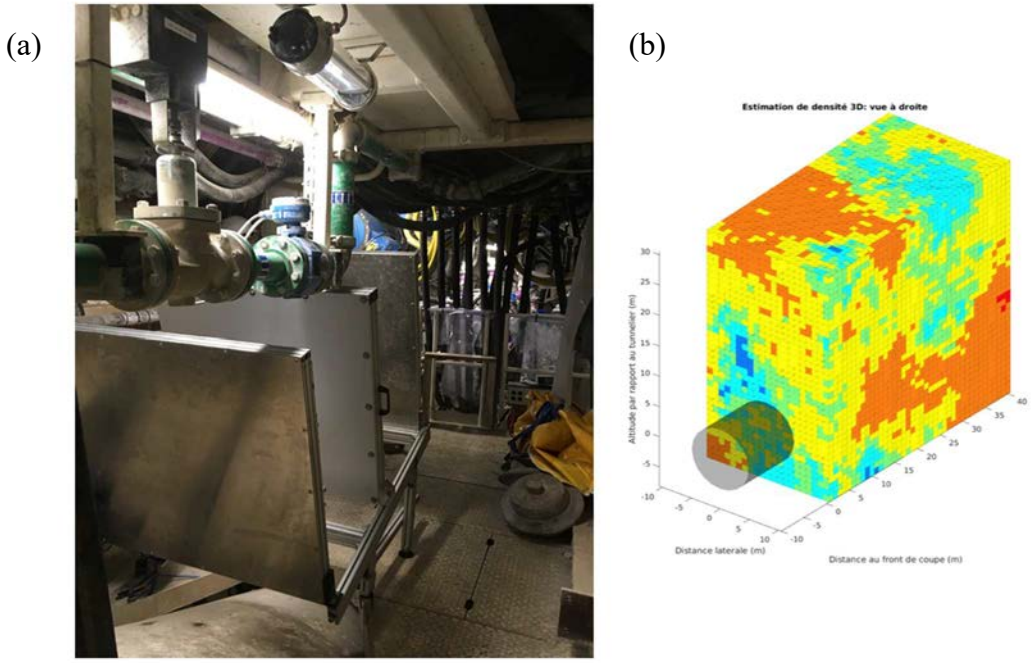

FIG. 23. (a) Picture of the muon detector inside the TBM. (b) Example of online 3D apparent density reconstruction averaging the last 50 m of the TBM movement (courtesy of J. Marteau, Institut de physique des deux infinis).

4. INDUSTRIAL APPLICATIONS

Industry is one of the fundamental pillars of economic activity worldwide. The industrial sector processes raw materials to manufacture finished goods ready for consumption by the end user or by other industries. The implementation of the manufacturing processes requires the deployment of large production plants with specialized equipment and personnel. Companies working in the direct transformation of raw materials such as minerals, petroleum, rubber, etc, usually need to produce chemical reactions involving extreme temperature and pressure conditions. The equipment used to transport the raw materials, to host the reaction, to supply energy, and to remove the products, usually operates under these hostile conditions making difficult both the monitoring of the process and maintenance of the equipment.

The processes implemented in industrial plants present a large heterogeneity, although many elements and features of these production infrastructures are common. These facilities often include equipment devoted to containing chemical reactions such as vessels, cauldrons, blast furnaces, etc, and auxiliary components to bring or remove materials, such as pipes, ducts, chimneys, and torches. The dimensions of these structures range from a few cm to several m, while most of their components are made of metals such as steel, Pb, and others, and also carbon-based such as refractory in the case of the walls of cauldrons, blast furnaces, and similar equipment.

A large fraction of the operation costs in many of these plants is directly related to the inefficiencies of the production procedures and the maintenance of the equipment. The former can present many different forms according to the specifics of each procedure, although it is frequently a consequence of incomplete knowledge about the processes. The latter is needed because of the gradual deterioration of the equipment due to exposure to environmental agents such as humidity, extreme temperatures and pressures.

Many companies implement strategies to mitigate these effects based on the careful monitoring of the processes and the equipment. Several NDT techniques are employed to perform this monitoring. There is a plethora of different technologies such as ultrasounds, X-rays, thermography, etc., that can serve this purpose (see Section 3.2). All of them present limitations in the achieved resolution, capability to penetrate the material, or exposure time. In many cases, the techniques are complementary and can be combined to improve the results. Many of these techniques require stopping production during ‘technical stops’ for maintenance. Depending on the kind of factory, these stops can last from a few hours to several days. The cost of stopping production can represent a large fraction of the total maintenance spending.

Muon imaging emerges in this context as a suitable NDT technique that offers large penetration power and the possibility to operate without stopping production since no artificial source of radiation nor physical contact with the equipment are needed. Due to the variety of different situations and problems in the industry, the needs and requirements are strongly dependent on the application.

In the following Sections several paradigmatic cases are shown to illustrate the potential of muon imaging in industrial contexts. The examples are grouped into two blocks attending to the kind of technique being applied: MST or muography.

4.1. INDUSTRIAL APPLICATIONS OF MUON SCATTERING TOMOGRAPHY

Muon scattering tomography requires the installation of muon detectors before and after the target (see Sections 2.1.2 and 2.3.3). This technique offers better resolution than muography and in general the exposure times needed to exploit the technique are much reduced. On the other hand, the installation of two detectors might be challenging in some industrial environments adding technical complexity to the general application of the technique.

4.1.1. Process monitoring: measurement of the metal–slag interface in furnace ladles

Heavy industry processes raw minerals in order to obtain pure metals. This procedure often involves heating of minerals beyond their fusion points until the mixture is in the liquid state. The segregation of materials takes place as a consequence of density difference. This mixture is often dumped into furnace ladles in order to be transported to different parts of the plant where they are usually emptied onto jigs. The total amount of pure metal in the ladle is an important parameter since a ladle with less metal than expected will result in unfilled jigs, while an excess of metal will leave waste in the ladle that will become solid and useless. The determination of the exact level of metal in the mixture is, however, a complicated task since light elements form an upper layer of slag that completely shadows the liquid metal. Since this layer is opaque, no optical method can provide a solution. The resolutions needed by the industry depend on the particular case to be considered but usually range in between one and a few centimetres.

Muon scattering tomography can be applied to this situation by considering a system of two muon detectors in an L-shape configuration as sketched in Fig. 24. The position of the detectors needs to guarantee that a fair number of muons cross the two detectors and the metal–slag interface. A cylindrical furnace ladle with diameter 240 cm and height 200 cm has been simulated together with two rectangular muon detectors with a surface of about 1 m^2. The ladle has an external steel shell and an inner refractory wall, both of thickness 10 cm. The densities of these materials have been considered to be 8.5 g/cm^3 and 3.5 g/cm^3. The content of the ladle has been simulated as melted steel with a density of 6 g/cm^3 and an 8 cm-thick layer of slag with density 2 g/cm^3. The muon detectors have an intrinsic spatial resolution of 4 mm. Cosmic muons have been simulated using the CRY cosmic ray shower generator [27], and GEANT4 [35] has been used to simulate the crossing of the particles through the ladle and the detectors.

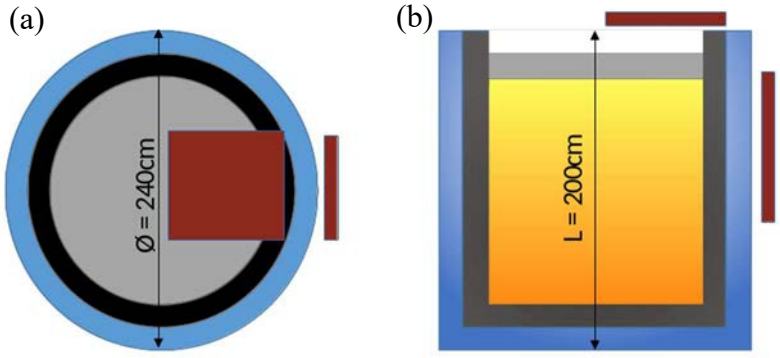

FIG. 24. Top view (a) and front view (b) of a simulated cylindrical furnace ladle with diameter 240 cm and height 200 cm together with two rectangular muon detectors, red rectangles, with a surface of about 1 m^2 (courtesy of Muon Systems[11]).

[11] https://muon.systems/en

A total of 17,000,000 muons have been simulated corresponding to an exposure time of about 60 minutes. A preliminary analysis using the POCA algorithm has been applied to determine the most probable scattering centres. Centres in the slag layer have been filtered out by selecting deviation angles higher than 50 mrad. A statistical analysis has been performed to determine the exact position of the interface, yielding a level of resolution of the order of 1 cm. It needs to be emphasized that this result has been obtained using a generic, simple algorithm, indicating a large margin for improvement if dedicated, more sophisticated algorithms are employed.

The result obtained is competitive with other techniques currently used in industry. Many factories do not perform a measurement of the metal–slag interface position and just assume this uncertainty and the resulting inefficiency as an inherent cost of the procedure. Some other plants implement mechanical procedures mainly consisting of the insertion of a temperature-resistant bar in the mixture. This technique is used in cases where the interface location has to be determined in the furnace itself. The spatial resolution obtained using this precision is relatively poor and requires stopping production to physically insert the probe from the upper part of the furnace.

The application of muon imaging to this problem poses two challenges:

- The first is related to the exposure time needed to collect a muon dataset with enough statistical power. This factor is highly dependent on the particular kind of furnace or furnace ladle being considered. The sizes and densities of the materials involved, and the needed spatial resolution determine the exposure time. Most of the applications require exposure times of the order of several tens of minutes;
- The second challenge is related to the installation of the muon detectors in the complicated environment around the furnace ladle and their adaptation to operate in relatively high temperature conditions. A suitable packaging for the muon detectors is needed to protect them from the temperature, dust and other environmental factors.

4.1.2. Preventive maintenance: measurement of the thickness of the walls of rotary furnaces

Rotary furnaces are frequently used by the chemical industry in order to transform materials through the calcination process. The rotation of the furnace guarantees the homogeneity of the mixture and maximizes the efficiency of the reaction. The sizes and types of these furnaces vary depending on the specific reaction being exploited. For instance, plaster powder is usually produced in rotary furnaces in which anhydrite is dehydrated and mixed with natural plaster and other additives. This reaction occurs in horizontally located, cylindrical furnaces with typical lengths of ~20 m and diameter of ~2.5 m. The structure of these furnaces consists of two concentric steel drums with a thickness of ~ 9 cm each. A gas at high pressure and temperature flows in between the two. The reaction takes place inside the inner drum as sketched in Fig. 25. The walls of this inner drum are rapidly degraded due to the temperature and the corrosion. Technical stops are executed every 3 months in order to check the drum's integrity. This process entails cutting a section of the furnace to allow a human operator to penetrate and measure the inner wall thickness with an ultrasound-based NDT. If the thickness is less than 1.5 cm, the drum is considered faulty, and replacement takes place. The process of cooling down, opening, inspecting and warming up can take up to 2 weeks and has a huge cost.

This application results very appealing for scattering muography, since a very large penetration power is needed in order to cross the whole furnace, and because of the impossibility to have physical access with the furnace at all. The simple rotary furnace in Fig. 25 has been simulated

within GEANT4 together with 2 muon detectors with a surface of 2 m^2 and a spatial resolution of 4 mm. Muons generated with the CRY program have been generated and propagated through the structure. The POCA algorithm has been applied to these data in order to obtain a measurement of the thickness of the walls. A statistical analysis of the POCA points and their angular deviations has been performed and a resolution of 1 cm has been achieved for exposure times of the order of 1 hour. In order to scan the full length of the furnace about 10 hours are expected.

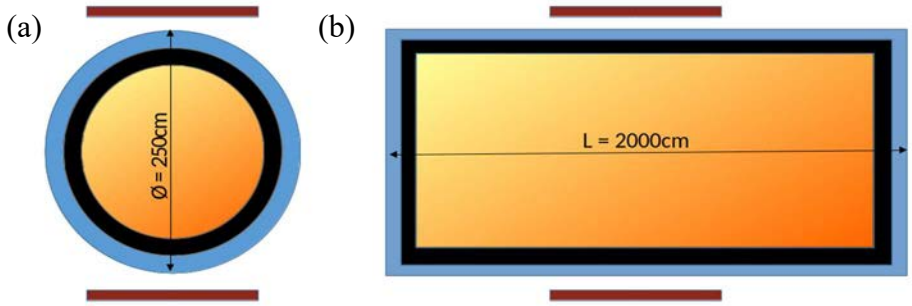

FIG. 25. Top view (a) and front view (b) of a rotary furnace with two rectangular muon detectors, red rectangles, located at the top and bottom of the furnace (courtesy of Muon Systems).

No other NDT technique has been able to solve this problem without stopping production and accessing the inside of the furnace.

The main challenges that muon imaging encounters on this kind of application are related to the size of the detectors and their location. Relatively large detectors are needed to accumulate enough statistics in a reasonable amount of time. On the other hand, locating the detectors above and below the furnace would require installing metal supports that can hold the detectors close enough to the furnace.

4.1.3. Preventive maintenance: measurement of the thickness of insulated pipes

Many industries in the heavy and oil sectors use pipes to transport gases and liquids as a part of their productive process. For instance, a medium size petrol refinement plant can have up to 200 km of pipes in operation conditions. The walls of these pipes frequently experience a reduction of their thickness as a consequence of corrosion processes. A degradation of the walls beyond a critical point seriously compromises the integrity of the pipes and the whole facility. Regular inspections of the pipes are planned and organized during the technical stops of the plant for risk evaluation and assessment. Several NDT techniques are available in the market to perform this task. Some of the most popular include gamma radiography and ultrasound-based tomography. The resolutions required by the industry strongly depend on the topology of the pipe and can range from a few mm to a few cm. Many pipes are thermally insulated from the environment by a layer of rock wool that prevents the heat from escaping. These insulation layers make some of the NDT techniques unable to solve the problem.

The use of muon imaging as an additional NDT technique for the preventive maintenance of pipes has been explored and documented [39]. Several tests have been performed in the laboratory using segments of real insulated pipes as shown in Fig. 26(a). The pipes have been placed in between two gaseous muon detectors with a surface of about 1 m^2 and an intrinsic spatial resolution of 4 mm. A data collection of about 30 minutes has been performed and the POCA algorithm has been applied to produce the images in Fig. 26(d). The insulation layer

around the pipe becomes transparent once a minimal angular deviation is required for the scattering centres. More sophisticated statistical algorithms have been applied achieving resolutions of the order of 2 mm in the thickness of steel-pipes, assuming a wear with azimuthal symmetry.

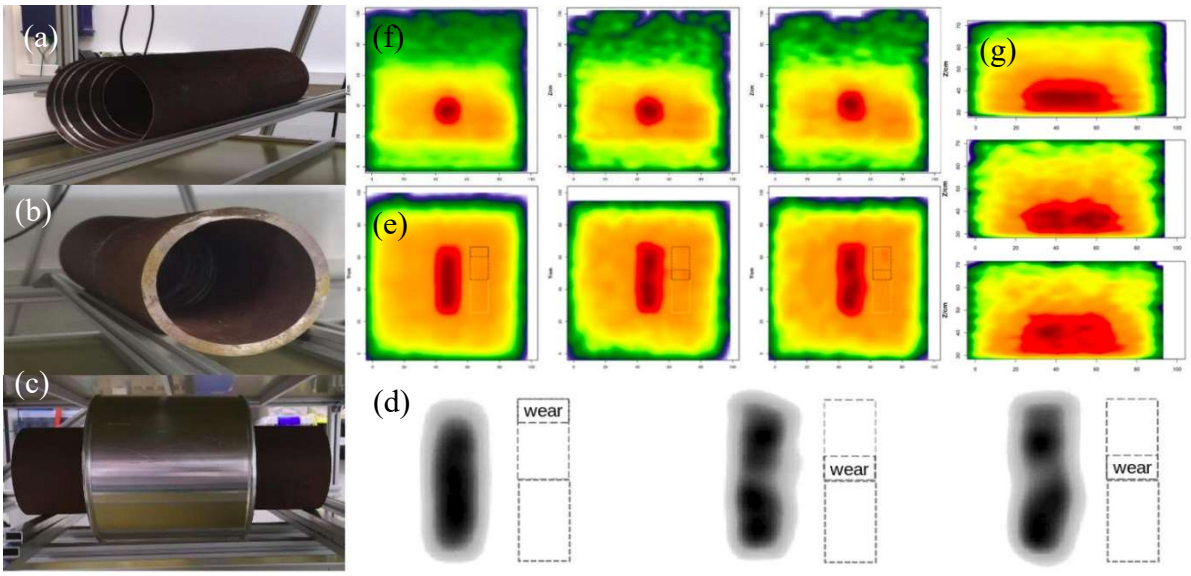

FIG. 26. Pictures of three test steel tubes with artificial wear located (a) at the beginning of the pipe, (b) in the middle of the pipe, and (c) the same as (b) but with an insulator wrapping the wear zone. Black and white reconstructed images (d) of the top view of the three wear cases (a–c). Colour reconstructed images of (e) the same top view together with (f) front and (g) side view (courtesy of Muon Systems).

4.1.3.1. Comparison of techniques

Gamma radiography can be applied in the case of small (up to 80–100 cm) pipes. The spatial resolution achieved by this technique is usually satisfactory for most of the applications, although it entails several drawbacks. Gamma radiography requires production to stop because of safety reasons. In addition, qualified personnel are required to perform the testing due to the restrictions in operating with dangerous radiation. The technique might also have insufficient penetration power in the case of large, thin pipes. Ultrasound-based NDT techniques provide medium-quality spatial resolutions but require physical contact with the pipes, which in most of the cases involves stopping the production. This technique is not suitable for insulated pipes since the rock-wool of the insulator absorbs most of the sound waves in the pipe.

Muon radiography presents two clear advantages:

- Maintenance can be done while the factory is in operation without additional costs related to the use of radioactive sources;
- It can inspect large pipes due to its great penetration power.

The spatial resolution achieved by muography is usually limited and probably inadequate for small pipes with wall thickness of a few millimetres. On the other hand, muography for pipe inspection poses similar challenges to those in other applications: keeping exposure times low enough to be practical and adaptation of the detectors to operate under factory conditions. In particular, the detectors ought to be mounted in a portable system that allows for easy inspection of large sections of pipes in a short amount of time.

4.1.4. Preventive maintenance: inspection of the inner structure of blast furnaces

Blast furnaces (BFs) are employed in the iron and steel industry to produce pure metals from the melting of raw minerals. The structure of a BF includes an external steel-shell, an inner thick refractory layer of different materials, and the burden. Energy is provided to the mixture by chemically produced flames at the bottom of the BF. The temperature of the burden can vary from 900 to 1300 °C severely damaging the surrounding refractory lining. The sector spends large amounts of money in the preventive maintenance of the BF, including the determination of the wear suffered by the refractory lining. A failure in this determination could compromise the integrity of the BF and eventually could lead to severe accidents with large economic, environmental and commercial costs.

The sizes of the BF can vary according to the different models used by the companies. The height of the structure is in the range 15–20 m. Most of the wear is expected in the hearth of the BF, which has a height of 3–5 m and a diameter of 6–10 m. The materials of the BF structure and the burden itself have a large density. Muon scattering tomography appears to be appealing as the total amount of material is large enough that muons are expected to suffer large deviations but not a huge attenuation. Experimental studies [40] on materials extracted from a BF have shown that it is possible to determine their density with 10% precision. Detailed simulations of a blast furnace have been studied and documented [41]. Muon detectors with a surface of 2 m^2 were located as shown in Fig. 27. The POCA and MLEM algorithms were used to determine the position of the refractory walls and some test loads located within the burden.

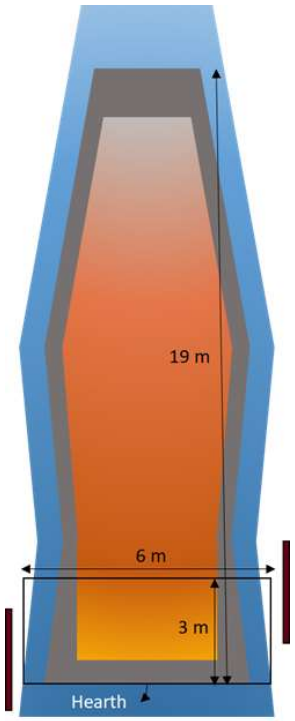

FIG. 27. Blast furnace front view with a hearth zone of 3 m height and a diameter of 6 m. Two rectangular muon detectors, red rectangles, located to the left and right of the furnace (courtesy of Muon Systems).

Other currently employed NDT techniques to measure the wear of the refractory include the use of acoustic waves applied on the external shell of the BF and the analysis of temperature profiles after drilling the walls. Both techniques have to be applied during technical stops since they require physical contact with the BF. Muon imaging can be applied while the BF is in operation, provided the muon detectors can operate in conditions of high temperature and a

dirty atmosphere. The size of the detectors has to be large in order to guarantee a sufficient number of muons crossing most of the components of the BF. The achieved spatial resolution for the refractory lining would be greatly improved if the momentum of the muons could be measured by the detectors themselves or by auxiliary detectors with this capability.

4.2. INDUSTRIAL APPLICATIONS USING MUON TRANSMISSION RADIOGRAPHY

Muography can be used for applications where exposure time is not a constraint, and the data collection can last for a long period of time. This is the case in applications such as the monitoring of internal changes of density of a given target, e.g., due to emptying of tanks or pipes, material deposition, fluid drains, leaks, etc. This monitoring technique assumes that the muon detector is stable during the full data collection series, which may last months, with constant detection efficiency and a large duty cycle. The monitoring capability depends also on the atmospheric parameters (barometric and temperature effects) which has to be corrected for, since they affect both the muons' fluence and the background contamination.

4.2.1. Production optimization: monitoring of a blast furnace

Blast furnaces are operated in cycles in which raw material is loaded through the throat according to production requirements. Understanding the dynamics of the loading process, the distribution of the materials and their later evolution can provide important input to optimize the efficiency of the BF. In this application, a muon detector was put on the side of the BF for more than one month during which several interventions in the BF led to abrupt changes in its load. This has been identified by a sharp increase in the detected muon flux and recorded as a function of time (Fig. 28).

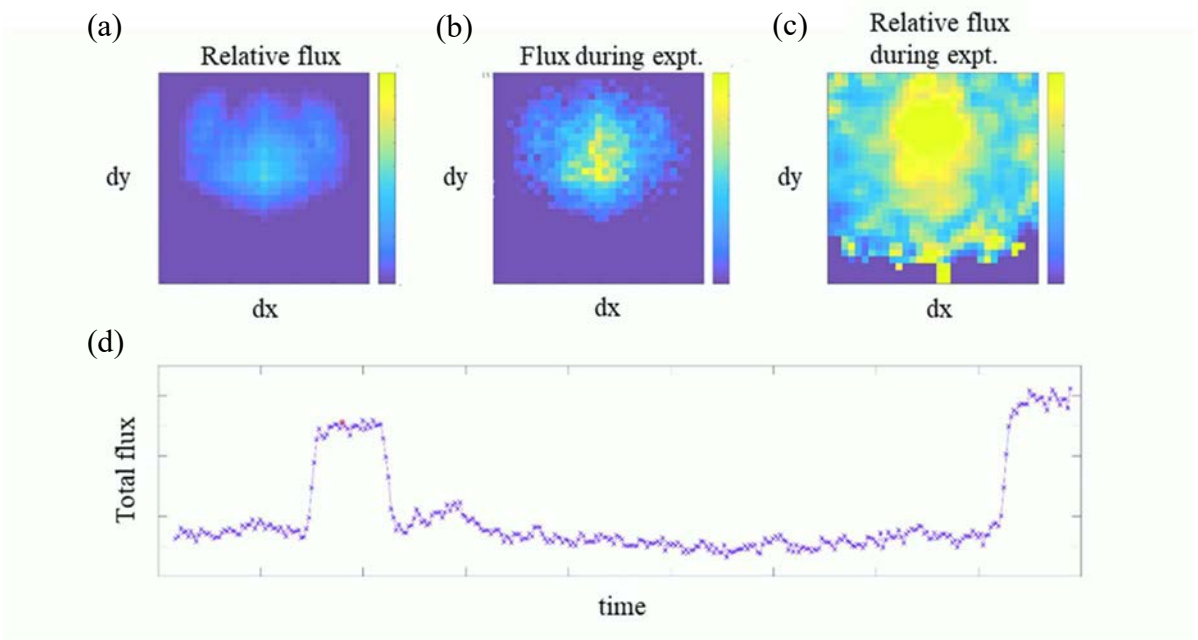

FIG. 28. Muon flux measurement as a function of time inside a BF in France. The top pictures show, for a given time t in the (dx, dy) scatter plot form, the raw reference muon flux (a), the raw measured muon flux (b) and the ratio of the two fluxes (c); (d) displays the integrated flux, corrected for the detector acceptance, as a function of time (courtesy of J. Marteau, Institut de physique des deux infinis).

The sharp increases recorded indicate quick unloading of part of the BF. Smaller variations of the recorded flux reflect both atmospheric changes and target variations. A sensitivity of about 10% can be achieved on the density variations inside the BF for an exposure time of one month.

This technique requires long periods of data collection during which the detector conditions have to be as uniform as possible. Dedicated calibrations accounting for environmental changes such as pressure and temperature are, therefore, needed for an optimal result.

4.2.2. Preventive maintenance: monitoring of a nuclear evaporator

Nuclear evaporators (NE) consist of large tanks where the nuclear materials from power plants are chemically separated into U, which may be recycled for future energy production, and the fission products which constitute a major part of nuclear waste (Fig. 29). The efficiency and safety of the NE operation depend on the parameters controlling the chemical reactions and on the NE itself being in good working order. Muography can be used to monitor the inner density of the apparatus as a function of time, providing information about the fluid levels in the burden, the presence of deposits or structural changes in the walls of the tank.

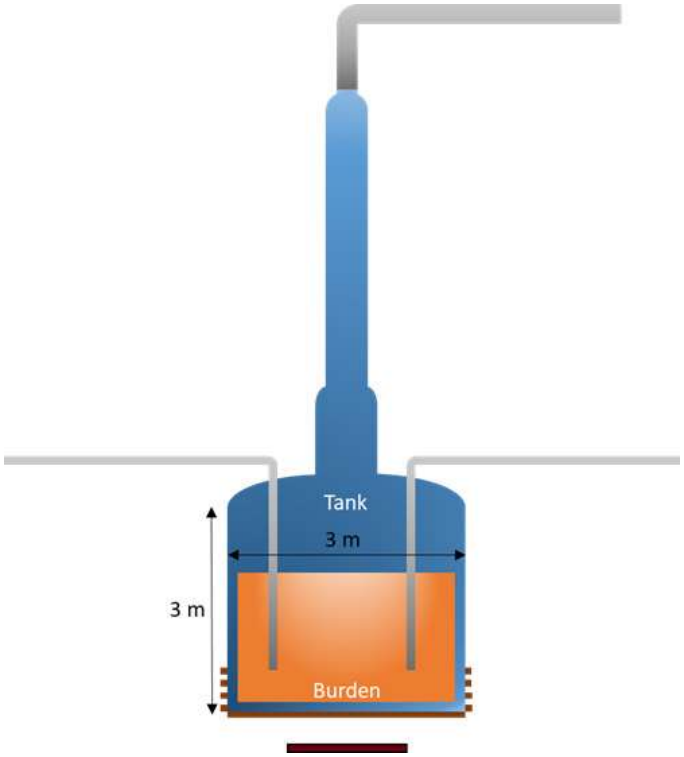

FIG. 29. Diagram of a nuclear evaporator with a muon detector installed below the base of the tank. The detector operates at high temperatures due to the proximity to the heat source (courtesy of J. Marteau, Institut de physique des deux infinis).

In this application, a muon detector was put directly below the NE, in a place where it had to be operated at high temperature (>50 °C) and in the presence of a permanent halo of low energy gamma rays. Fig. 29 shows a simplified diagram of the setup used for this test. An analysis was performed using the so-called inter-event distance, defined as the time elapsed between two consecutive muon events recorded in the detector. Fig. 30 displays the inter-event distance for different states of the NE cycle. Fig. 30(a) and (c) correspond to the NE operation in standard conditions. Fig. 30(b) shows a reduction of the inter-event distance indicated by an increase of the muon flux and a change in the standard conditions. A detailed analysis of the results showed a perfect correlation in time with the NE duty cycle of partial/total renewal of the inner tank fluids. Possible extensions of the monitoring process are under study to detect smaller changes in density inside the cell due to possible malfunctioning of the NE resulting in excessive deposits.

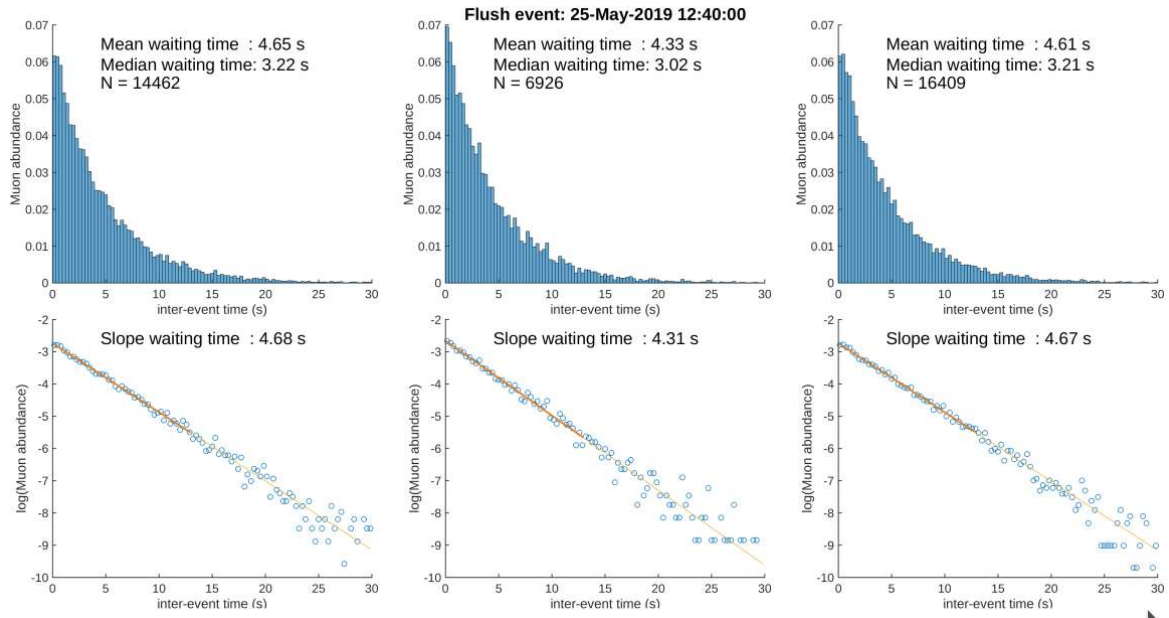

FIG. 30. Inter-event distance for different states of the NE cycle. (a) and (c) correspond to the NE operation in standard conditions. (b) presents a reduction of the inter-event distance indicating an increase of the muon flux and a change in the standard conditions. Such a method correlated with atmospheric parameter corrections may be developed to reach the few percent sensitivity level relevant for industrial requirements (courtesy of J. Marteau, Institut de physique des deux infinis).

5. VOLCANOLOGY

Volcanoes are structures of enormous importance from the geophysical point of view. For more than twenty years they have been adopted as a reference case study for muography. Although this technique applies only to the most superficial part of the Earth's crust, this very shallow region of our planet has the most direct effect on human life. The information that can be acquired from the Earth's interior is always indirect, and thus has to be collect various kinds of independent information to comprehensively interpret the phenomena visible at the Earth's surface. For this aspect, acquiring information that is independent of what is collected by conventional methods is important. A volcano is one of the most dynamic geological features of our planet and eruptions are hazardous for human activities, particularly when they occur near large cities. For this reason, various research institutions have focused their attention on different specific processes of this natural phenomenon. Magma movements, magma chamber growths, and eruption processes have been inferred, modelled and interpreted with seismic, gravimetric, geodetic, electromagnetic, and geochemical techniques. During the course of these studies, techniques have become more accurate when it comes to forecasting the start of a volcanic eruption. However, the magnitude and duration of eruptions still cannot be predicted. In general, the magnitude and duration of an eruption is determined based on whether or not the magma ascends to the surface. Muography offers us a new source of information about this question.

Volcanoes are usually very large structures for which muography is the only realistically practicable muon imaging technique. Muography complements traditional survey methods by offering directional sensitivity to the density distribution, allowing thus the imaging of the in-depth structure. Moreover, muography can be used on dangerous volcanoes that cannot be accessed to carry out the traditional field surveys. The choice of the muon detection and tracking system is different from case to case, often because of the expertise gained by the different groups involved in each measurement. Unfortunately, in most cases of interest in volcanology, narrow structures in the deepest part of very large, massive targets (from a few hundreds of metres to a few kilometres thick) have to be resolved, even at low elevation angles where the atmospheric muon flux is extremely weak. The rate of muons surviving after traversing the upstream material is very small compared to the typical free-sky rates (see Section 2.3.1) and can be overwhelmed by background. Reducing the effects due to background sources is therefore one of the main concerns of muography in this field, considering that these uncertainties do not decrease with increasing amounts of collected data.

Many volcanic edifices have been selected as test laboratories by the muography community due to their intrinsic geophysical interest and for their destructive potential. Monitoring and study of the behaviour of active volcanoes may mitigate risk to nearby populations. Because muography is still under development, the choice is often, but not always, guided by logistical assessments; e.g., proximity of a high energy physics group developing muon tracking detectors or nearby presence of a relevant volcanological institute providing logistical support for the installation of the detectors and the implementation of the measurement campaigns. This explains why this kind of application is more frequent in countries like Japan, Italy and France, where both communities are well developed. Recently there has also been substantial activity in Colombia in this area.

The size of muon tracking systems currently employed at volcanoes usually allows muography to be performed with data collection of several months, sufficient to register enough muon tracks to investigate inner volcanic structures and to provide information on the angular distribution of the rock density, which is essential for volcanologists to understand the volcano's

history. Nonetheless, modifications of the internal configuration due to magma movements of hydrological dynamics can be observed within even shorter times, thus allowing the exploitation of this technique for quasi-on-line monitoring of underground activity.

5.1. ACTIVITIES IN JAPAN

The first applications of muography in the field of volcanology were proposed and carried out in Japan between the end of the last century and the beginning of the current. Japan has been at the forefront of muography since the 1990's [42]. As volcanoes are very dynamic, several systems timestamp the observed muons in order to determine density variations through time: evolution in the muon flux through a volcano over time may precede eruption.

5.1.1. Magma ascent and descent in Mount Asama

A major breakthrough in this area was the first application of muography to forecast the eruption sequence of Mount Asama in central Honshū, the main island of Japan, during its unrest in 2009. The data from the muography campaign on Mount Asama demonstrated that the variation of muon flux transmitted through the crater region correlated with rise and fall of magma. The Japan Meteorological Agency used this data as an input for eruption forecasting. Muography imaged a volcanic plug formed at the top of the vent of Mount Asama as well as the empty magma pathway underneath in two and three dimensions. Further consecutive muographic observations showed that the surface part of this plug had been blasted apart but magma didn't ascend to the surface when a subsequent eruption occurred five years later [43]. The time-sequential images were interpreted as an over-pressurised-vapour-driven eruption and thus, it was concluded that recurrent eruptions would not take place. This was correct and no eruption occurred. This achievement was reported to the Japanese Commission of Volcanic Eruption Prediction.

5.1.2. Magma ascent in Satsuma-Iwojima

Motion of a column of magma was also measured in another a Japanese volcano, Satsuma-Iwojima, during two eruptive episodes in 2013. The system used here had six layers of position-sensitive scintillator planes (1.7×1.7 m^2) each alternating with 10 cm thick Pb plates to reduce background. Time-sequential muographic images taken from Satsuma-Iwojima volcano in Japan captured the ascent of the magma convecting towards the surface, corresponding with observation reports of volcanic glow in 2013 [44]. The magma convection clarified with muography [45] indicates that measurements of land deformation alone could underestimate the magma supply rates [46], and as indicated by the muographic data, this eruption occurred recurrently.

5.1.3. Plug formation in other Japanese volcanoes

In Sakurajima volcano, also in Japan, plug formation processes were imaged. Sakurajima is one of the most active volcanoes in the world and is situated close to a large city; the distance between the city centre and the active craters is only 10 km. Since 2011, more than 8,000 eruptions have occurred, and volcanic activity continues. The past volcanic studies explained the eruption type of this volcano as one with recurrent plug formation followed by explosion [47]. A Japan–Hungary collaboration used muography to image its highly defined internal structure [48] and the gradual growth of the volcanic plug underneath the newly activated crater [49]. Some of the volcanic vents are not recurrently activated. The vent underneath the Japanese Showa-Shinzan lava dome has been tightly plugged with magma [50] and has not been active

since 1944. A similar type of plug can be also seen inside the Japanese Usu volcano and was muographically located inside the mountain right below the region where land deformation occurred in the years 1977–1980 [51].

In 2016, a test was conducted to perform a muographic study of the Unzen lava dome aboard a helicopter. Airborne muography is not restricted by the topography of the mountain and can approach to a within few m of the volcanic surface. The volcanic spine structure was imaged inside the lava dome generated during the 1991 Unzen eruption in Japan using this method [52]. Muography as a tool to interpret the volcanic eruption processes is being realized also for other volcanoes in Japan, Italy and France, at Kirishima, Japan [53], Etna, Italy [54], Stromboli, Italy [55], Vesuvius, Italy [56], La Soufriere, France [57], and Puy de Dome, France [58].

5.2. ACTIVITIES IN ITALY AND FRANCE

One of the most recent measurements was conducted at Mount Stromboli [55, 59], a stratovolcano of the Aeolian archipelago, Italy. The term 'Strombolian', used in volcanology to describe volcanoes with emissions of huge amounts of gas and continuous eruptive activity, was derived from the characteristics of this volcano. The first muographic image of this volcano was obtained by collecting data for five months with an emulsion detector (Fig. 31), which as a passive measurement system is particularly appropriate to overcome the logistical difficulties in the decidedly hostile environment.

FIG. 31. The nuclear emulsion detector installed at Mount Stromboli in Italy (courtesy of V. Tioukov, Istituto Nazionale di Fisica Nucleare).

The pros and cons of using nuclear emulsion detectors were outlined in Section (2.2.3). Due to their limitations, they are not suitable for online monitoring of a volcano's activity. Two muographic experiments were performed on Stromboli using the emulsion technique but with different internal modules. In the first measurement, reported in Ref. [55], four layers of emulsion were mounted as two doublets with 5 mm of Fe in between. Such a structure provides good tracking purity and efficiency as well as excellent angular resolution. After five months of exposure and following emulsion processing, imaging of crater of the volcano to a spatial resolution of ~6 m and the identification of a low-density zone 200 × 50 m^2 wide close to the North-East crater area was reported.

Similar to other muographic measurements of objects on a km scale, this set-up suffers from multiple Coulomb scattering, which deflects low momentum muon trajectories and constitutes the most important source of blurring for the muographic imaging. To overcome this limit, a second installation on the Stromboli slope was created by the same team with a modified module geometry [59]. The new detector was composed of 120 plates, 0.25 × 0.3 m^2 wide,

assembled into 12 piles of 10 emulsions interleaved with 9 Pb plates, 1-mm thick, encapsulated inside 6 tracking modules, which acted as mechanical protection and soft insulation from the environmental conditions. Thanks to micron-level spatial resolution, the emulsion tracking system can detect scattering of low momentum tracks crossing the 1 mm Pb absorber plates and so to reject most of the muons with momentum below 1 GeV/c, thus cleaning the signal of most of the scattered background events [60]. Fig. 32 shows the muon 'hit map' reconstructed using one of the six nuclear emulsion tracking modules.

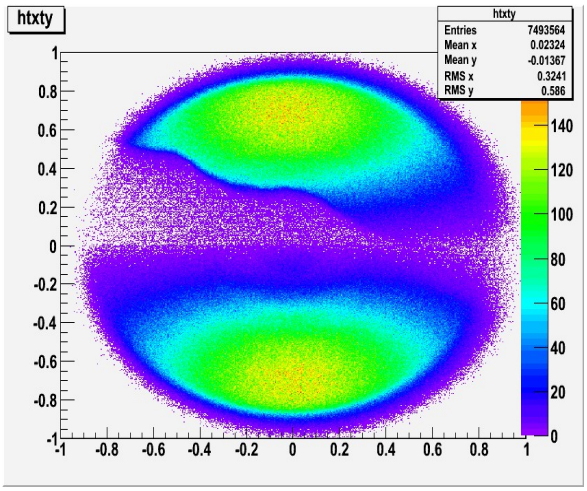

FIG. 32. Muon hit map at the Stromboli volcano reconstructed using one out of six emulsion modules (courtesy of V. Tioukov, Istituto Nazionale di Fisica Nucleare).

5.2.1. MU-RAY and MURAVES projects at Mt. Vesuvius, Italy

A study of Mount Vesuvius, a stratovolcano near Naples, Italy, is on-going. Vesuvius is well known for the 79 A.D. eruption that devastated Herculaneum and Pompeii due to the collapse of a giant cloud of ash and gases. This was witnessed by Pliny the Younger, and the term 'Plinian' is used in volcanology to indicate this very dangerous class of eruptions. Today more than 500,000 people live around Vesuvius in a region classified as a 'red zone', where a high risk of pyroclastic fallout exists if a new sub-Plinian eruption occur [61]. The proposal for a muographic study of Vesuvius was thus mainly motivated by hazard concerns due to the dense urbanization all around this volcano [62]. The first 2D muographic image of Vesuvius was produced by the MU-RAY research and development project [63] during a preliminary campaign carried out using three *x–y* tracking modules. This measurement confirmed an important source of background of low energy muons coming from directions outside the detector's acceptance but scattered inside the acceptance through multiple Coulomb interactions within the volcano's outer layers. This results in an anomalous muon rate coming from directions at very low zenith angle, where the flux of high energy muons traversing the volcano and entering the detector's acceptance becomes particularly low. To reduce this background source, the MURAVES[12] project [56], an upgraded and slightly larger-scale implementation of the MU-RAY detector, added a 60 cm thick Pb absorber after the original tracker and a fourth *x-y* tracking module downstream to tag muons with energies below approximately 1 GeV, which are slowed down, deflected and possibly stopped in the Pb block (Fig. 33). This was complemented by time-of-flight circuitry to reduce another source of background coming from muons scattered within the soil and entering inside the detector's acceptance from the back side.

[12] Acronym for Muon RAdiography of VESuvius.

FIG. 33. The first full 1 m^2 muon detector system (red) installed in 2019 in the Vesuvius muographic observatory created by the MURAVES collaboration (courtesy of L. Bonechi, Istituto Nazionale di Fisica Nucleare).

The MU-RAY collaboration has developed tracking planes made of plastic scintillator bars of triangular cross-section, that permit a better spatial resolution (~3 mm) than using bars of rectangular cross-section for a detector of the same overall size and number of readout channels. Light signals produced by muons within the scintillators are converted to electrical pulses by means of low power state-of-the-art light sensors. Signals are collected by custom front-end electronic boards and the resulting digital data written to memory. These types of detectors, based on low power electronics, are very robust and can be operated in harsh environments, possibly powered by batteries and photovoltaic panels. Currently, the entire muographic laboratory set-up on the slopes of Vesuvius by the Italian research institutes Istituto Nazionale di Geofisica e Vulcanologia and Istituto Nazionale di Fisica Nucleare is powered by a 5.4 kWp photovoltaic island system with a 15.7 kWh battery pack, which is sufficient to operate a set of detectors of such size, a custom temperature regulation system based on Peltier devices and the status of the detector is accessible remotely.

5.2.2. TOMUVOL collaboration at Puy de Dôme, France and Mount Etna, Italy

The TOMUVOL collaboration in France has undertaken a study of Puy de Dôme [58–63], a lava dome almost 1500 m high, which is part of a long volcanic chain. Thanks to existing detailed geophysical data and to its ease of access, this site represents an excellent location to test the performance of the muographic methodology and to further develop both instrumentation and data analysis techniques. In 2013, the TOMUVOL[13] and MU-RAY collaborations carried out a joint measurement campaign at the Puy de Dôme [64] using their detector prototypes, based on two different technologies with complementary merits. The TOMUVOL muon telescope was composed of planes of glass RPC (Resistive Plate Chamber) detectors originally developed by the CALICE[14] collaboration, which was a new detector designed to be operated at future high-energy linear colliders for particle physics research. Both telescopes, deployed at approximately 1.3 km from the summit of the volcano, were composed of 1 m^2 tracking layers without the ability to identify particles but with a positional resolution of a few mm and energy threshold of a few hundred MeV. As neither of the two prototypes had

[13] Acronym for TOmographie avec des MUons atmosphériques des VOLcans, i.e., volcano tomography with muons.
[14] Acronym for CAlorimeter for LInear Collider Experiment.

a dedicated time-of-flight-based discrimination system, time resolution was relatively poor: tens of ns, and hundreds of ns for MU-RAY and TOMUVOL, respectively. The MU-RAY tracker had three *x*-*y* detection modules and a 3-cm thick steel plate that both acted as an absorber to screen muons with momentum below an effective threshold of 70 MeV/*c* and induced showering for particles other than muons. TOMUVOL had four tracking modules and no absorber. With these configurations, the background contribution was found to exceed the signal level at opacities larger than 500 mwe. The same level of background was observed by both teams. This revealed the main source of background [65] came from the lowest energy muons, including those with momenta greater than 70 MeV/*c*, scattering on the slopes of the volcano. Three other sources of background could be eliminated:

(i) 'Fake' muons (i.e., hadrons, electrons or positrons), which would be filtered by MU-RAY's absorber;
(ii) A combinatorial component (e.g., from detector noise, or a shower of cosmic particles coming orthogonally to the detector axis that accidentally align so as to fake a muon track), which would be drastically reduced by TOMUVOL's larger number of layers;
(iii) Muons entering from behind the detector.

The design of the detectors was later improved providing a higher momentum threshold and time-of-flight measurement capability that could identify the soft and backward muons crossing the detectors, thus allowing more robust muographic imaging of kilometer-scale volcanoes.

5.2.3. MEV project at Mount Etna, Italy

Mount Etna, near Catania, Italy (height > 3 km, diameter ~40 km at the base) is the largest and highest active volcano in Europe and erupts through four summit craters as well as from vents and fissures on its flanks. The geometry of the conduits that supply the four craters remains largely unknown. Etna's great size is a challenge for muography. A few teams have performed feasibility studies using various approaches, targeting different craters. In 2010, the South-East Crater, (height 240 m, diameter ~500 m at the base) was studied by an early version of the DIAPHANE telescope (see Section 5.2.5) [66].

Preliminary results have been reported from the extinct Monti Rossi crater using the MEV (Muography of Etna Volcano) project [54]. This team developed a high-resolution telescope with three layers (1 m^2 each) of scintillators. These were used as a reference for future studies of the active Northeast Crater. Use of large quantities of Pb to reduce background (see the approach taken in Sections 2.3.1 and 5.1.2) is unfeasible for the summit of Mt. Etna, where access of heavy equipment is limited. The MEV project was created in 2016 with two objectives:

(i) To make the first high-resolution muography of the summit crater complex of Etna;
(ii) To establish a volcano monitoring network using muography.

The MEV collaboration included physicists, engineers, geologists, and volcanologists and was conducted with the approval of the 'Parco dell'Etna' authorities. The detector was designed for long-term measurements near the summit of Etna. It consists of three *x*-*y* position-sensitive planes, with a sensitive area of 1 m^2, enclosed in a custom designed container to guarantee water- and light-tight operation. Two solar panels are mounted on the upper side of the container and charge two batteries. The overall power consumption is 10 W. The container is mounted on a modular frame made of scaffolding tubes which facilitate transportation of an assembled telescope to the measurement site using a truck with a mechanical arm. Alternatively, the

modular internal Al structure, which holds the position-sensitive plates parallel, can be assembled in the field. Each module is under 50 kg, so can be hand carried along with the electronics. During summer, the external container is not required. The frame is supported by adjustable legs, making it adaptable to uneven terrain. The prototype is characterized by custom-made electronics which, together with an innovative read-out channel compression system, reduces power consumption and make it suitable for operation in extreme conditions. The system, which also included muon time-of-flight measurements for background rejection, was transferred in August 2017 to the base of the North-East crater of Etna.

Three data acquisition campaigns, from August to October 2017, from June to November 2018 and from July to October 2019, have been performed and the analysis of the collected data is currently underway. At the end of October 2019, the telescope was brought back to the Department of Physics of the University of Catania for maintenance and to evaluate the effects of the long stay at high altitude on individual components of the telescope. The acquired and processed data will is now being interpreted and will be used by volcanologists for the study of the fumaroles characterizing the Northeast crater (Fig. 34). The first preliminary results were presented in 2018. Further hardware development to improve the detector's efficiency and background rejection are under consideration. Further information about the MEV project can be found in Refs. [67–70].

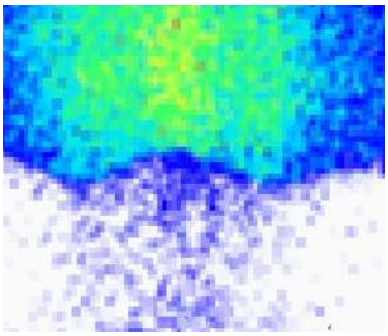

FIG. 34. Muography of the Northeast crater of the Etna volcano acquired in 2018 by the MEV (courtesy of D. Lo Presti, Istituto Nazionale di Fisica Nucleare).

5.2.4. ASTRI-Horn telescope at Mount Etna, Italy

Yet another approach has been taken on Mount Etna, using Cherenkov light detection [71, 72]. Such systems have negligible backgrounds, which compensates for their poorer statistics due to the larger intrinsic momentum threshold ($p > 5$ GeV for Cerenkov radiation vs. $p \sim 4$ GeV for atmospheric muons). The ASTRI-Horn telescope is a prototype built as part of the Cherenkov Telescope Array project for astrophysics [73]. It was placed at Serra La Nave, 5 km from the South-East Crater, but there are plans for the construction of dedicated movable telescopes, in order to reach different observation points.

5.2.5. DIAPHANE collaboration at La Soufrière, Guadeloupe and Mount Etna, Italy

The first French collaboration using muography in 2007 was built around an interdisciplinary project involving particle physicists[15] and geophysicists[16]. The project focused on the structural and dynamical characterization of an active volcanic dome of La Soufrière of Guadeloupe in

[15] Institut de physique des deux infinis de Lyon, CNRS–Institut national de physique nucléaire et de physique des particules and the University of Lyon

[16] IPGI, Institut national des sciences de l'Univers du CNRS, University of Paris, Observatoire des Sciences de l'Univers de Rennes, CNRS-INSU and University of Rennes

the Lesser Antilles which underwent a phreatic eruption in 1976. This eruption was the external manifestation of the intense activity of this volcano's hydrothermal system. Indeed, this volcano receives a large amount of water (10–12 m of rain per year) which 'soaks' the entire dome and exists in the form of an unstable liquid–gas equilibrium. The structural imaging of the dome may identify the most mechanically weak zones of the dome while the dynamical imaging gives information on the possible phase transitions and vaporization.

Changes within hydrothermal systems affect density distributions close to the surface. Hydrothermal fields that accompany moderately active volcanoes can cause sudden explosive events, extremely dangerous for humans especially if there no precursor signal is identified. Muographic time series from different observation points have been used in the study of the Soufrière's hydrothermal has been extensively studied by the DIAPHANE collaboration from 2010 on [57, 72–76]. Data is taken several identical muon telescopes consisting of three scintillator layers with absorber, using time-of-flight to reject background events (Fig. 35).

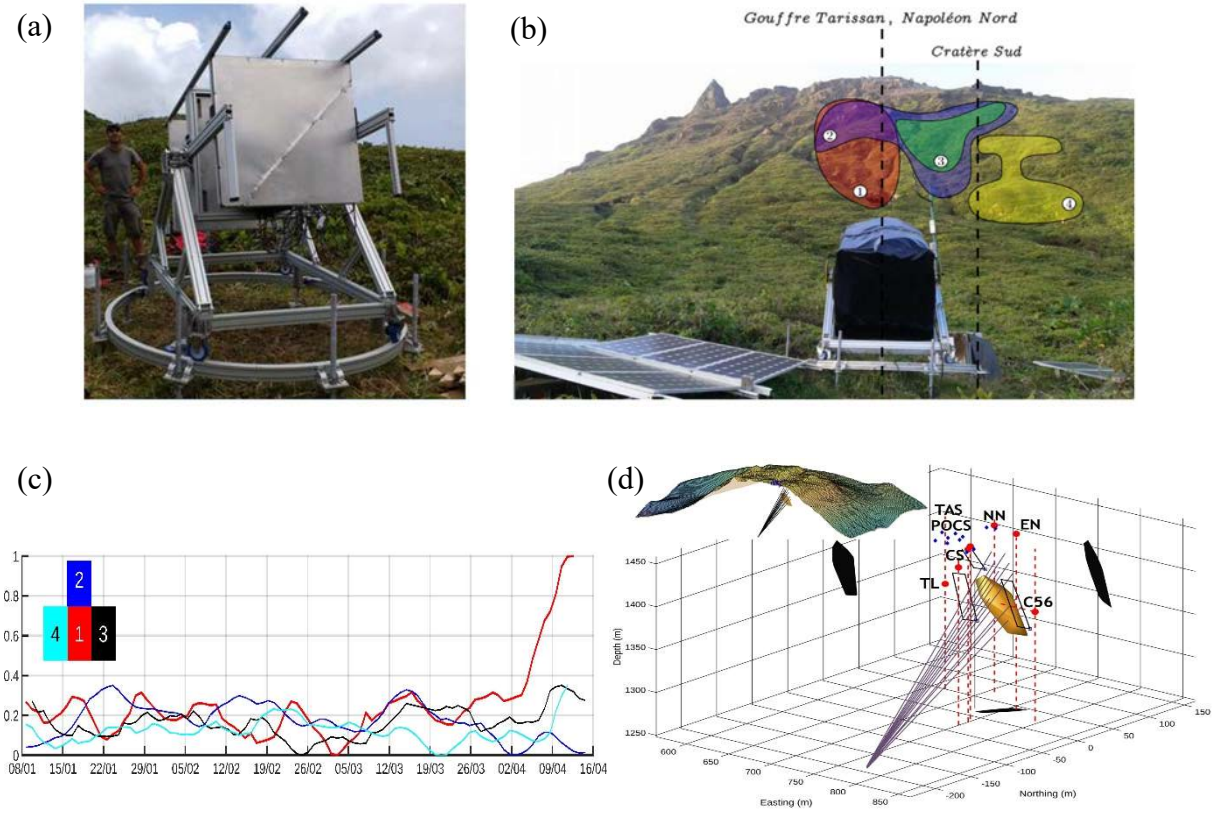

FIG. 35. (a) One of the six muon trackers installed at la Soufrière de Guadeloupe by the DIAPHANE team and (b) identification of separated angular regions showing different behaviour of muon transmission variations in time; (c/d) muon-seismic coupled observation of a sudden variation in an internal volume of the Soufrière's dome (CC BY by the authors of Ref. [72]).

In a recent study [74], a combination of muographic and seismological data was used to detect a hydrothermal spot 50–100 m below the summit, at timescales of a few hours to a few days (Fig. 35(c/d)).

By measuring the time variations of muon flux attenuation, the collaboration could isolate specific regions inside the volcano showing similar time behaviour. This allowed interpretation of the observed variations as vaporization or movement related to groundwater dynamics.

6. ARCHAEOLOGY

Among all the potential applications of muon imaging, archaeology is probably the field which has elicited the largest interest from the general public. From the pioneering work of L. Alvarez in the late 1960s to the discovery of several voids in Khufu's Pyramid 50 years later, archaeology has spectacularly illustrated and popularized the muon's ability to 'see behind the walls'. Beside the natural interest to unravel mysteries of ancient civilizations or historic sites, muon imaging indeed offers an outstanding potential for many archaeological studies with particularly appropriate features:

- Non-destructive imaging, particularly adapted to the context where structures may be fragile or unstable;
- Relatively direct interpretation: whereas electric, acoustic, thermal or gravimetric measurements often require complex corrections and interpretations, many structural details can already be seen in a raw muography image;
- Possibility of in situ measurements in public places: as the source of radiation is natural, only the detector is required, which makes it radiologically safe for people around;
- Possibility to scan large structures;
- High sensitivity to density variations, and thus suitable for void detection.

On the other hand, the specific conditions of archaeological sites provide strong demands on muography equipment. These requirements are often similar to the ones encountered in the volcanology applications (Section 5); i.e., transportability, compactness, robustness, low electric consumption, autonomy, large area for deep structures, good spatial resolution, noise rejection, etc. The instruments need to resist harsh conditions, like humidity, sandstorms and various intruders, from cable-eating mice to tourists (see, e.g., Fig. 36). They need to also be operated for long times to accumulate statistically significant results. Typical uses concern relatively large objects, for which muography is the most suitable method. However, muography measurements can also be performed in lab on smaller objects like artefacts. In this case the scattering mode, MST, is more favourable and provides very good spatial resolution.

FIG. 36. View of a detector after 9 months of data acquisition in Khufu's Pyramid, showing degradation due to mice (courtesy of ScanPyramids[17]).

[17] http://www.scanpyramids.org/

Because of the advantages listed below, most of the applications of muons in archaeology focus on the imaging of large structures which are out of reach of methods based on artificial radiations. Some representative and illustrative examples are listed below.

6.1. PYRAMIDS

In the late 1960s, L. Alvarez et al. [6] identified what was in his opinion the most promising site for muography, namely the Khafre pyramid of Giza. In contrast to the neighbouring Khufu pyramid, far fewer corridors and chambers were known. The configuration of this pyramid was also optimal for a muography measurement, with a single room (the Belzoni Chamber) located at the centre of the pyramid. Alvarez and his team received authorization to bring large spark chambers from the USA, and the whole apparatus was installed in 1967 [75]. Facing numerous difficulties, ranging from the Six-Day War to the somewhat delicate operation of these early particle detectors, the team recorded several years of good data. Unfortunately for them (and certainly also for the rise of muography), no voids were detected, though this was a major piece of information for Egyptologists.

A similar experiment was conducted in the 2000s by the team led by A. Menchaca on the Teotihuacan pyramid in Mexico. This pyramid has a very similar configuration to the Khafre one, with a corridor leading to a central room at the base of the pyramid. For three years, their multiwire proportional chamber detector accumulated data, which could reconstruct the external shape of the pyramid. A lower density zone was identified (and announced by the media as at risk of collapse), but no additional rooms were found [76].

Following these prestigious predecessors, an international mission started in 2015 to investigate several Egyptian pyramids of the fourth dynasty, under the supervision of the Egyptian Ministry of Antiquities, Cairo University and the Heritage Innovation Preservation Institute[18]. In addition to thermal measurements, surveys by drones and photogrammetry, the ScanPyramids mission employed the three main technologies nowadays used in muon imaging (see Section 2.2):

- Nuclear emulsions, manufactured by Nagoya University, Japan [77] consisting of 30×25 cm² independent tiles arranged in large mosaics of several m². Being extremely compact, they provide an angular resolution between 2 and 14 mrad. As explained in Section 2.2.3, these detectors do not require a power supply. However, because of their fragility and sensitivity to the environment (temperature and humidity), they were only used inside the pyramid. During the measurement campaigns they were regularly replaced by new films, and sent back to Japan for development, scanning and offline analysis with a dedicated high-speed scanner and computer farm;
- Plastic scintillators from KEK, Japan [78] arranged in planes of 1.2×1.2 m² surface, with a 1.5 m lever arm (the distance between the first and last plane) which compensates for the modest single-plane resolution of scintillators, resulting in a 7 to 10 mrad resolution. This type of detector is particularly robust and insensitive to the environment, and has relatively small power requirements (300 W). In contrast to the nuclear emulsions, the telescope provided online reconstruction and imaging through a single PC;
- Gaseous detectors from CEA, France [79] arranged in several telescopes of 50×50 or 50×100 cm² and flushed with a non-flammable, Ar-based mixture. The detectors were built using the resistive bulk Micromegas technology with a multiplexing scheme to reduce the number of electronic channels. They provided a 0.8 to 4 mrad resolution with a lever arm of 60 cm ensuring reasonable compactness. As was the case with the scintillators, they

[18] http://www.hip.institute/

allowed for online reconstruction with a nano-PC and an overall consumption of 35 to 70 W. They were also the only detectors to be operated both inside and outside the pyramid.

After a successful test with the Nagoya equipment in the Bent Pyramid during which the upper Chamber was detected from the lower one, all the instruments were deployed on Khufu's Great Pyramid in 2016 (Fig. 37). Several emulsion mosaics were installed in the Descending Corridor and in the Queen's Chamber with the scintillator telescope, while the Micromegas detectors were positioned around the edges of the pyramid to complement the observed zones.

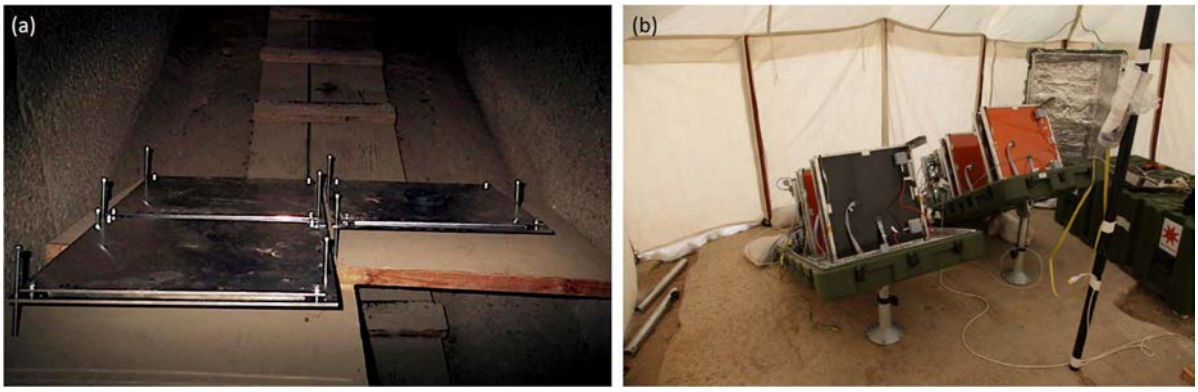

FIG. 37. Installation of (a) emulsions plates in the Queen's Chamber and (b) Micromegas detectors on the East side of the pyramid (courtesy of ScanPyramids).

Because of the extraordinary dimensions of this pyramid, several months of acquisition were required in each position to accumulate enough statistics. Gaseous detectors experienced the most challenging conditions, with temperatures reaching 45 °C and frequent sandstorms. Several high voltage feedback loops were successively implemented, until a complete stabilization of the gain was obtained [80]. In October 2016, the first two voids were announced by the collaboration [81]: a corridor-shape one detected from the Descending Corridor by the nuclear emulsions in the vicinity of the North face Chevrons, and a small void on the North-East edge detected by the gaseous detector system.

In early 2017, a first analysis of the Nagoya emulsions from the Queen's Chamber revealed a large excess of muons around the Grand Gallery. Less significant excesses consistent with approximately the same region were found with the plastic scintillator and gaseous detector systems. Dedicated measurements therefore took place in spring and summer 2017 where all three detector systems successively obtained a 5σ signal of a large void in the core of the pyramid [82]. Simulations based on a 3D model confirmed that these observations point to the same zone located above the Grand Gallery, and precise triangulation could be achieved using the data from the nuclear emulsions and gaseous detector systems (Fig. 38).

After the 2017 campaign, additional measurements were scheduled starting from 2018 to better define the dimensions and shape of this 'Big Void'. In particular, new emulsion films and an improved version of the Micromegas telescopes were installed in the Grand Gallery itself; i.e., the closest accessible zone to the new void. It is worth mentioning that the Grand Gallery is a major part of the circuit inside the pyramid and leads to the famous King's Chamber. As such, the instruments had to operate in a highly touristic, narrow place, a condition that only a technique using natural radiation could cope with. To achieve this, the gas consumption was reduced by a factor of 12 after intense research and development on the detectors and a better understanding of gas contamination [83]. As a result, it was calculated that a single tourist releases more non-oxygen gas (CO_2) than the Ar purge gas required for two 0.5 m² telescopes.

A 20-litre pressurized bottle can now provide three years of autonomous operation for a small telescope. Combined with the complete gain stabilization of the detectors, achieved in an environment of changing temperature, pressure and humidity, ScanPyramids has triggered a major step forward in the widespread use of gaseous detectors for muography.

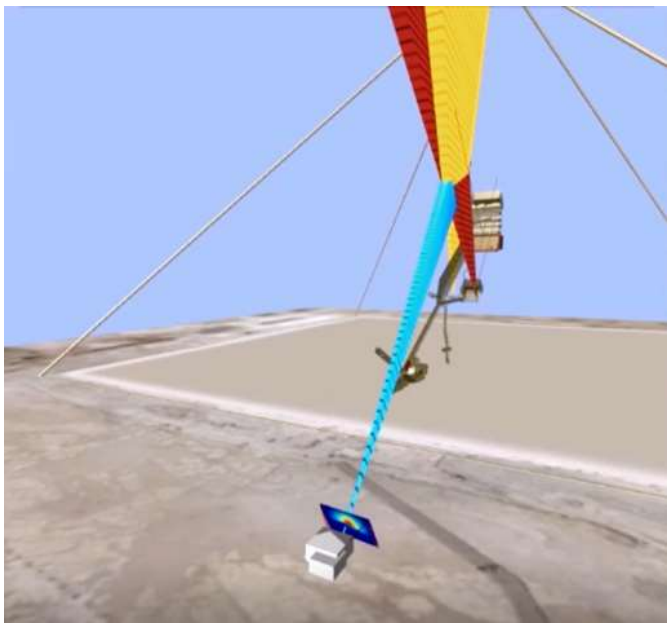

FIG. 38. Triangulation of the Big Void using Nagoya and CEA data. A wire-frame outline of the pyramid is shown, together with some of the internal structures and the positions of the two cameras (courtesy of ScanPyramids).

6.2. TUMULI

Tumuli are ancient funeral constructions which were erected to cover burials, tombs and structures associated with them (e.g., corridors, supporting walls etc). Many examples of tumuli are present worldwide, particularly in Europe. In Northern Greece, for instance, the discovery in 2012 of a monumental tomb, under a tumulus in Amphipolis, known as the Kasta tomb or the Amphipolis tomb, has triggered interest in a variety of imaging techniques, including muography, to perform systematic investigations on all known tumuli. Indeed, these are monuments of the past that have to be preserved and usually re-examined, since other valuable structures could be hidden within a tumulus, besides the main tomb.

Thus, the geophysical problem is set regarding the investigations of the interior of tumuli. The aim is to locate the burials and the other ancient structures under the embankment. From recent discoveries, tombs are usually located near the periphery of the tumulus at ground level or lower, accessible by a ramp, which is also buried, and used to build them. As in the case of pyramids, muography may complement the few geophysical methods used to look for the monuments inside, like resistivity sounding, magnetic profiling, seismic waves, etc. This has been done for example within the ARCHé project, a French–Greek collaboration[19], to scan an almost unexplored tumulus near Thessaloniki, the Apollonia tumulus (see Fig. 39). This tumulus is roughly 100 m diameter and 25 m high. A picture of the tumulus and the van containing the muon detector is displayed in Fig. 40.

[19] Institut de physique des deux infinis de Lyon, France; Laboratoire d'Annecy de Physique des Particules, France; AstroParticule et Cosmologie, Université Paris Diderot, France; and the University of Thessaloniki, Greece.

FIG. 39. Picture of the Apollonia tumulus near Thessaloniki in Northern Greece, and the muon detector van facing it (courtesy of J. Marteau, Institut de physique des deux infinis).

One of the major challenges is the fact that the bulk of such structures may be quite wide but not very tall. The largest proportion of the muons traversing the structure is, therefore, nearly horizontal, which is the least intense part of the flux. First results on this particular tumulus revealed large heterogeneous sub-structures compatible with the existence of a travertine fault on which the tumulus was built.

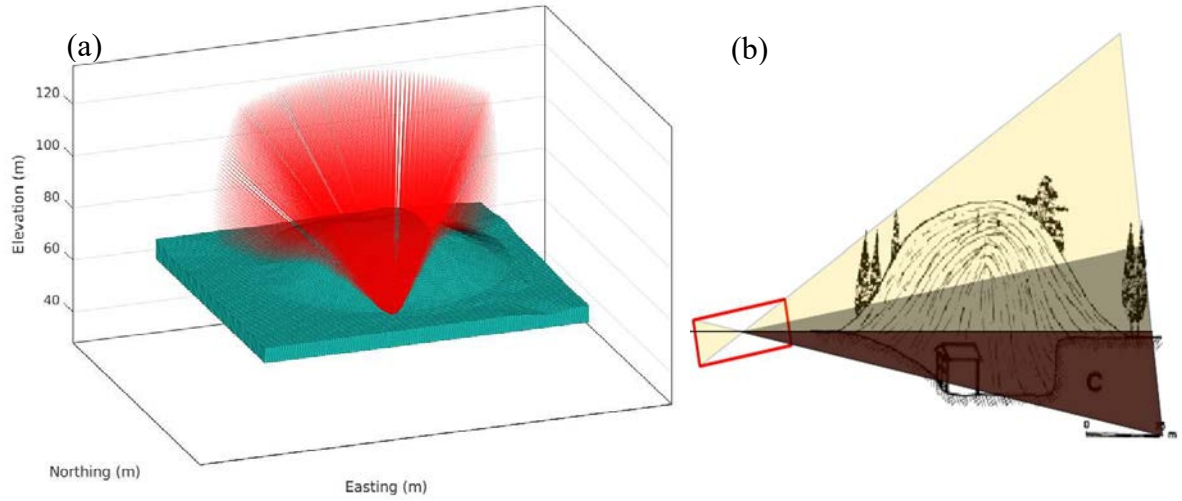

FIG. 40. (a) Drawing of the muon trajectories reaching the muon detector at the Apollonia tumulus near Thessaloniki. (b) Sketch of the detector acceptance divided into the forward muons side (in yellow) and the backward muons side (in brown). Since the muons are generated above the horizon, the forward muons cross the target before reaching the detector and may be used for analysis. The backward ones reach the detector without having crossed the target and are not exploitable for imaging. However, they may serve as a reference sample (courtesy of J. Marteau, Institut de physique des deux infinis).

6.3. UNDERGROUND MEASUREMENTS

Identification and localization of artificial structures or voids in underground sites are a typical class of problems that can be addressed successfully by muographic studies focused on archaeological sites. In reality, the identification of walls of ancient buildings or stone manufactured goods hidden underground is usually a non-trivial task for muography due to the small differences in densities between the structures of interest and the material (soil) filling the surrounding volume. Usually the localization of walls (if near the surface), is performed more efficiently by means of electromagnetic techniques (i.e., ground-penetrating radar or geoelectric surveys), which are sensitive to the differing electrical properties of the various structures. On the other hand, underground cavities, tunnels and rooms completely empty or only partially filled with soil, represent optimal targets for muography, which can be exploited as a complementary technique to the more traditional ones. Apart from archaeological interests, the localisation of underground cavities can also be relevant to the safety of excavations; e.g., the structural characteristics of the overburden of an access route needs to be known in order to

provide adequate structural reinforcements. Another reason motivating the localization of large underground voids in the proximity of passageways (e.g., for tourism exploitation), is the study of particular areas of sites where anomalous concentrations of radon gas occur, due to fracturing of the rocks. In these cases, a possible explanation could be unknown additional artificial tunnels and cavities that may facilitate the release and flow of this gas from the surrounding rocks.

In general, muography becomes extremely powerful when the depth of the sites to be imaged is greater than 10–20 m and other techniques are at the limit of applicability. Other sites where muography may be most advantageous are those characterized by a very uneven top surface that could also have a layer of thick vegetation, as those conditions are particularly challenging for other methods. Particular types of terrain, either too moist or too dry, can also hinder the use of electromagnetic techniques, while muography can be used without problems.

Between 2017 and 2020, the Muon Imaging for Mining and Archaeology (MIMA) team[20] carried out measurements on an archaeological site, the Bourbon Tunnel in Naples, and inside a mining complex, the Temperino mine near Livorno, which is of interest from the archaeological point of view. These are described in the Sections below.

Motivated by the interest to demonstrate the performance of muography in the fields of archaeology and geology, the collaboration developed a dedicated hodoscope, the MIMA detector [84], to allow muon track reconstruction with high efficiency. This detector was designed to fulfil the requirements for in situ measurements. Additionally, background suppression capability could be necessary in some applications, in particular to identify low energy muons. The MIMA hodoscope is a compact and lightweight muon telescope, with a geometrical factor[21] of the order of 1000 cm^2sr and a mass of 60 kg including mechanics and electronics. This tracker consists of three independent *x-y* tracking modules stacked inside a thin $50 \times 50 \times 50$ cm^3 Al box. At least three modules are required for a clean reconstruction of real muon tracks, allowing the rejection of fake events triggered by random noise signals, the identification of possible multiple tracks appearing in the same event and so on. This hodoscope is usually mounted on a dedicated altazimuth platform which can precisely define the detector's orientation.

6.3.1. Bourbon Gallery

Following a previous experiment [85] with the MU-RAY prototype detector (see Section 5.2.1), a larger, 1 m^2 system developed for applications in volcanology and therefore less practical for installations in narrow, confined spaces, the MIMA detector was tested for a measurement inside the Bourbon gallery inside Mount Echia, Naples, Italy. This measurement was performed with two aims:

(i) Verifying the results of two previous muographies performed with the MU-RAY detector;
(ii) Testing the new detector in a real field campaign in an almost uncontrolled area.

[20] An Italian collaboration between INFN, Florence and the Departments of Physics and Astronomy and of Earth Science, University of Florence.
[21] This term refers to the proportionality factor between the detector counting rate and the intensity of incoming particles.

Several lessons have been drawn from this experience, which allowed for the implementation of some simple solutions for an optimized data collection. The main adaptions made were due to the presence of high humidity underground:

- The electronic boards had to be protected from condensation;
- An automatic restart of data acquisition at system reboot was implemented, due to electrical power cuts.

The first results obtained at the Bourbon tunnel by MU-RAY and MIMA [86] clarified the need for a precise digital terrain model around the installation's location. The interpretation of the angular distribution map of muon transmission is strictly dependent on the geometry of the target volume. After taking into account all the relevant geometries in the simulations, from the comparison between the measured and simulated muon transmission maps, a confirmation of the existence of two unmapped voids was possible (Fig. 41).

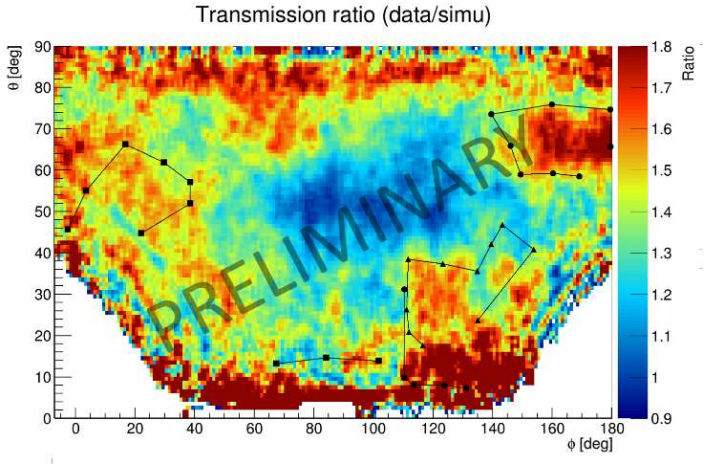

FIG. 41. Relative muon angular transmission map (ratio between measured and simulated angular transmission maps). Because of the uniform composition of the 'Mount Echia' tuff hill, a constant rock density was assumed in the simulation. Values of the relative muon transmission larger than 1 are interpreted as the positions of possible voids (red/orange areas in the figure). Black points/lines report the boundaries of the known voids and of one of the unmapped voids, whose 3D geometry had been already reconstructed in a previous measurement by MU-RAY (the upper right void). The large muon flux at high elevations corresponds to the second unmapped void (courtesy of L. Bonechi, Istituto Nazionale di Fisica Nucleare).

Two different algorithms to provide a localization in three dimensions were tested:

(i) A three-dimensional reconstruction algorithm based on triangulation was implemented exploiting multiple two-dimensional muon angular transmission maps measured from different points of view [87];
(ii) Later, an innovative algorithm based on muon track back-projection, exploiting only the information from a single measurement to find the distance of detected voids from the detector (described in Section 2.3.2), was successfully tested on the data collected by MIMA.

The distance of an unmapped void was estimated and found to agree with a preliminary triangulation based on the two measurements performed with the MU-RAY detector [23].

6.3.2. Big Quarry cavity, Temperino Mine

In order to test and further develop the muon imaging algorithms in archaeology, the MIMA collaboration identified the Temperino mine in the 'San Silvestro' archaeo-mining park in

Campiglia Marittima, near Livorno, Italy, as an optimal testing ground [86]. In this site a tourist passageway runs for approximately 350 m at a depth of 40–50 m underground and several other mapped and unmapped cavities and tunnels are located within the rock layers above. A large known cavity, the so called 'Big Quarry', is located 20 m approximately above the tunnel and develops at the interface between two very different materials with very different densities: marble and skarn. The Big Quarry was taken as the reference void to be studied from the tunnel underneath. This site has an interesting conformation to test the capabilities of the muographic technique and to develop the imaging algorithms.

Several muographies have been performed so far at this site, three of which were dedicated to the study of the Big Quarry [88]. Thanks to an accurate comparison of the measured muon transmission maps with the results of simulations, it was possible to convert muon transmission maps into average density maps, providing useful information for geologists. The analysis of these maps and comparison with available geological information allowed the identification of candidate voids. The signal corresponding to the Big Quarry was identified thanks to a comparison with a geometrical reconstruction that had been performed using a 3D laser scanner. This signal was studied using the back-projection method introduced before. From this analysis it was found that this method may provide multiple solutions. The correct one can be selected by making a first estimation of the distance of the Big Quarry from the detector with a simple triangulation of the low-density regions seen from three installation points. Three other large voids, besides the Big Quarry, were found. A three dimensional reconstruction was obtained and compared from the results of the laser scanner survey (Fig. 42). The muographic reconstruction of the Big Quarry agreed pretty well with the cloud of points obtained by means of the laser scanner. The average difference in the cavity size with the two methods (muography and laser) is of the order of 1 m (Fig. 43), over the whole volume.

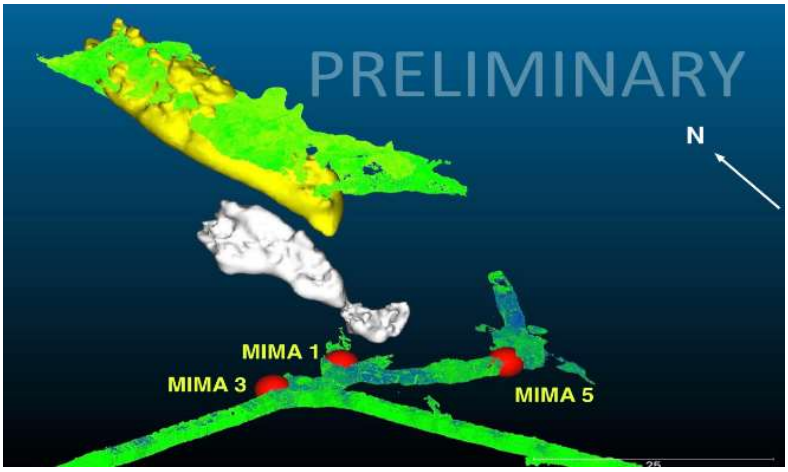

FIG. 42. 3D muographic reconstruction of voids detected near the Big Quarry at the Temperino mine; the reconstructed volume of the Big Quarry is drawn in yellow, while two unmapped voids are shown in white. The green point clouds refer to the 3D laser scanner survey performed inside the Big Quarry and in the galleries underneath. The three red spheres refer to the three MIMA installations in the zone of the Big Quarry (courtesy of D. Borselli, Istituto Nazionale di Fisica Nucleare).

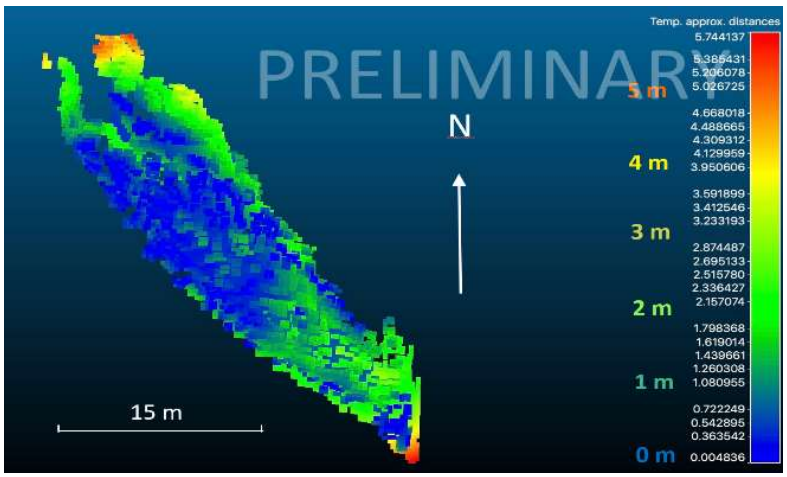

FIG. 43. Distance between the 3D laser scanner and muographic cloud points describing the Big Quarry, a large cavity 20 m above the detector at the Temperino mine; the average difference is about 1 m (courtesy of D. Borselli, Istituto Nazionale di Fisica Nucleare).

Ref. [89] demonstrated the possibility to obtain a 3D reconstruction of voids by using a single set of muon tracks reconstructed from a single point of view through the back-projection method described in Section 2.3.2. The localization and geometrical reconstruction of large existing voids is important in itself but can also be used as input for the initialization of true 3D reconstruction algorithms (stratigraphics) of the density distribution in the volume under observation.

6.4. SEISMIC STUDIES OF TEMPLES AND BURIAL MOUNDS IN ASIA

Muography has been applied to confirm the existence of a void in an ancient Hindu temple called Prambanan, Central Java, Indonesia. These muographic images were combined with seismic simulations to evaluate the earthquake resistance of this building by inputting the waveforms and amplitude of the 2006 Athens earthquake, and it was confirmed that the structure is sufficiently strong to withstand such an earthquake [90]. Muography could also be applied to the Borbudor site, South Central Java, Indonesia, which is currently sinking, by imaging the foundation underneath the structure.

Damage to large scale heritage sites sometimes records past seismic activities. By combining muography data with our historical knowledge about the construction time, one can obtain unique, specific information about past earthquakes, and by imaging the internal structure; e.g., the angle and shape of the slip surface, and the magnitude of these earthquakes can be inferred [91]. Whilst most historic seismic activities have been studied by analysing ancient documents, if megalithic heritage sites can be used in the same way, one will obtain additional information about the cycle of large earthquakes that will be useful to apply towards predicting future large-scale earthquakes and their effects. Recently, a muographic study was conducted of the 6th century Imashirozuka imperial burial mound, Japan, that was originally built as a megalithic tomb. It collapsed about one millennium later in the 1596 Fushimi earthquake. Results implied a problem in the design of the foundation of the tomb [92].

7. SECURITY APPLICATIONS (BORDERS AND FACILITIES)

Customs and border control agencies around the world regulate and facilitate international trade. While their specific priorities differ from country to country, all of them require technical capabilities to detect a variety of threats and contraband materials hidden in the cargo. Materials of interest typically include narcotics, explosives, alcohol, tobacco products and even human beings, as well as nuclear and radioactive material. Modern technical capabilities at the border often include radiation portal monitors (RPMs) and X-ray scanners.

X-rays provide useful imaging information for many types of cargo, but their penetration and hence detection capability is limited for more dense objects and especially large, heavy metal parts or machinery. In contrast, high-energy cosmic ray muons are very penetrating and can go through all kinds of cargo. Furthermore, muon scattering is sensitive not only to material density, like X-rays, but also to the atomic number of materials. Different materials can therefore be discriminated by muon scattering. The combination of material discrimination [93–95] and high penetration make cosmic ray muons a sensitive material probe useful for border security applications [96–98].

Initially MST was proposed as an advanced technology to detect nuclear material smuggling and to address the threat of nuclear terrorism, by scanning cargo containers for fissile materials [8]. Later the capabilities of muon scanning systems have been expanded to detect and visualize differences in density that could indicate various kinds of threats and other contraband in cargo containers and vehicles.

The advantages of various border systems currently available need to be considered when designing an inspection regime: RPMs provide quick screening times on the order of seconds, are relatively cheap to maintain, and have close to 100% operational availability; whereas X-ray systems have comparatively high maintenance costs, much less operational availability, and such scans require more time and generate ionizing radiation fields. Both RPM and X-ray systems can be deployed as fixed or mobile systems. MST systems are large and fixed but require no radiation generator to function, meaning that their reliability is expected to be high (similar to an RPM), but a screening time on the order of 1–30 minutes is typically needed to obtain analysable images for most applications.

7.1. STATE OF THE ART

To determine the scattering angle, one needs to measure the trajectory of every charged particle both before and after it goes through the inspected volume. The particle trajectories are reconstructed using positions provided by position-sensitive particle tracking detectors located above and below the detection volume. Many types of particle detectors have been proposed and used for muon tomography. Border control application requires a scalable, large-area system able to inspect sea containers, trucks and other vehicles. Such a system has been developed by Decision Sciences[22], specifically for the maritime, land border crossing, defence and critical infrastructure sectors. A recent version of the system called DISCOVERY has a detector footprint of 732 × 2195 cm^2 and is therefore suitable for inspection of large objects (Fig. 44). Large area detectors, consisting of Al drift tubes, provide a robust and economical technology for measuring incoming and outgoing particle trajectories.

[22] https://decisionsciences.com/our-product.

The detectors provide information on particle trajectories. The image reconstruction consists of two basic steps: statistical calculation of the relevant signal and placing the signal into the appropriate location.

Section 1 describes multiple Coulomb scattering, the concept of radiation length and its relation to *Z*. Muon scattering tomography is usually applied to measure the radiation length or some proxy parameter (e.g., scattering density) related to it. This measurement can be done by calculating the product of scattering angle and particle momentum. In fact, there are two scattering angles in perpendicular planes *x* and *y* that provide independent information. Additionally, the deflection of each particle can be measured.

FIG. 44. The muon tomography system DISCOVERY deployed at the US–Mexico border crossing (courtesy of K. Borozdin, Decision Sciences).

While based on the same principles of the physics of the particle interaction with matter and following the same general approach, image reconstruction methods differ significantly in how they allocate the signal to specific places in the image. Because of the deficiencies of the POCA based and MLEM techniques (see Section 2.3.3), other image reconstruction methods have been developed to both calculate the signal based on the measured tracks and allocate this signal to a voxelated three-dimensional grid to produce the image. The median has been proposed as a statistical measure, being more robust against outliers. Because of the uncertainties in the real particle trajectories, as compared to those inferred from linear approximations, the signal can be distributed in space to represent this uncertainty. In practice, this amounts to trading image noise for image blur. Another way to extract more information from available data is to approximate the signal in the voxel as a sum of multiple Gaussians [99].

The three-dimensional image represents the strength of the scattering signal in a false colour scale. These false colours can be used to visualize the distribution of matter within the volume as well as to discriminate between material groups, organics, metals (as illustrated, for example, in Section 8.3.4), etc. However, there is more information in the particle tracks than can be extracted in false colour images. Besides scattering angle and momentum estimation, measurements for particle deflection and distance of the closest approach are also obtained, which are both statistically correlated with the scattering angle, but are independent measures of material properties. Different statistical parameters can be calculated from the distributions, and because of the uncertainties with the objects' locations and sizes, material properties can be calculated differently. Additional information is provided by the muons and electrons that are stopped in the volume of interest. Stopping of muons and electrons, which depends mostly on material density, can augment the information provided by the scattering and discriminate between the materials that produce the same scattering signal but differ in composition. This can be extended with other techniques for certain applications (see Fig. 14 for a comparison of muons, radar, ultrasound, and X-rays, for example).

Even though additional measures provided by tracking can be highly statistically correlated, they enable more sensitive material discrimination by putting material properties in multidimensional space. These measures or features can be used as a data set for machine learning methods that can provide discrimination, classification and identification of materials.

Besides tracking charged particles, the drift tube detectors also detect X-ray and gamma radiation. X-ray and gamma photons produce secondary electrons in Al that then cause gas ionization, in the same manner as charged particles from cosmic rays do. The difference between charged particles and X-ray/gamma radiation is that the former creates tracks in the detector, going – if they have enough energy – through multiple drift tubes located above and below the detector volume. In contrast, a radioactive source outside the detector volume would be more likely to create a signal in a single tube (or group of tube detectors on only one side of the detector volume) that would not, in general, belong to a track moving through the tubes on both sides of the detector volume. Additionally, whereas muons are entering the tubes omni-directionally from outside the detector volume, a radiation sources inside the detector volume would only generate a track on one-side of the detector volume for each emission event. Therefore, X-ray/gamma radiation sources, outside of or inside the detector volume, can be independently detected. With appropriate screening times, large area detectors can provide a detection sensitivity comparable to or exceeding standard portal monitors. Furthermore, it is possible to distinguish between a compact source of radiation and naturally occurring radioactive material by analysing the spatial extent of the radioactivity in the detector volume [100].

7.2. EXAMPLES

Some examples of the DISCOVERY system's performance were presented to the World Customs Organization [101] and are described below. Fig. 45 shows images of what was presumed to be solid coiled steel rolls on a flatbed trailer. X-ray inspection provided no actionable information, due to its inability to penetrate the steel load. It could therefore only provide 'black box' images, without any indication of an internal structure of the load. On the other hand, muon images clearly showed that there was something less dense inside the rolls in a scan collected in approximately 4.5 minutes. After opening the rolls, multiple metal boxes were discovered inside containing bricks of marijuana wrapped in plastic. In total there were approximately 4,150 pounds (1,900 kg) of marijuana hidden inside the rolls with a street value of approximately US $20 million.

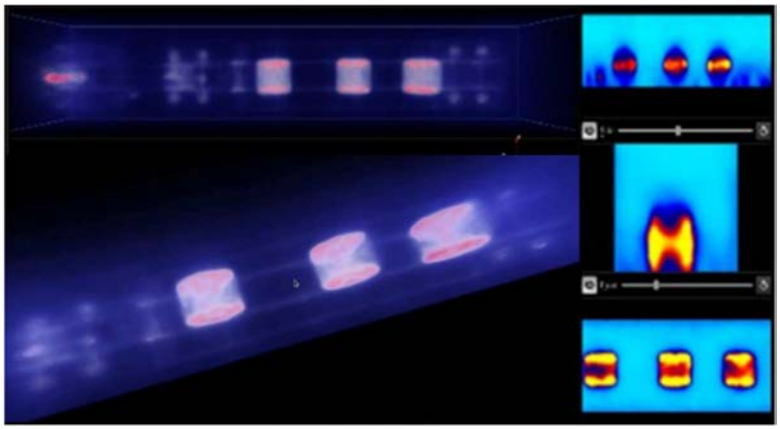

FIG. 45. Images provided by the DISCOVERY system revealed an internal structure inside coiled steel rolls. Image exposure time was ca. 4.5 minutes (courtesy of K. Borozdin, Decision Sciences).

Muon imaging can be used to detect anomalies in many different types of cargo. While Fig. 45 demonstrates an anomaly caused by marijuana inside steel, Fig. 46 shows an image anomaly

caused by a cocaine surrogate hidden inside of a pallet of bananas. The total weight of the surrogate was about 25 kg. This surrogate material was clearly seen in the image as a bright spot. The other pallets are clearly uniform without similar anomalies.

A reconstructed DISCOVERY image for another test scene is shown in Fig. 47. In this scene different chemicals that are surrogates or precursors of explosives are placed inside pallets of bottled water and charcoal. All three objects – two of which weighed 100 kg and one weighed 36 kg – were clearly seen as anomalies in the image that is otherwise without noticeable anomalies.

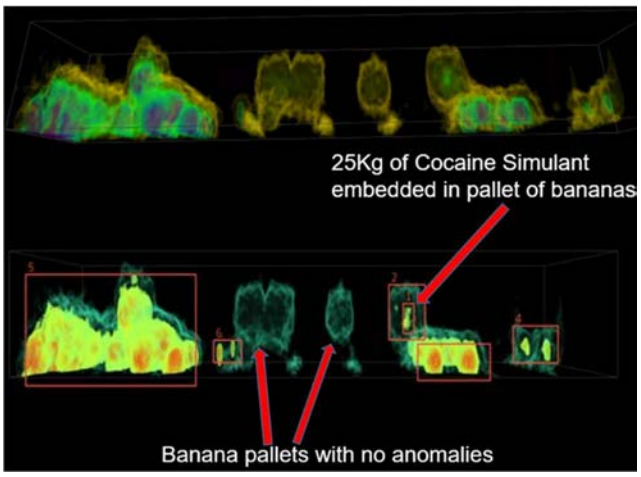

FIG. 46. A muon tomography image of a shipment of bananas with a cocaine surrogate embedded. The image was obtained with a DISCOVERY system installed in Nogales, AZ (USA–Mexico border). Bananas in cardboard boxes were put on a standard shipping pallet with approximate dimensions 1.2 m × 1.2 m and ~2 m tall. A cocaine surrogate was also put in a cardboard box with a weight of 25 kg. The image exposure time was 10 minutes. The surrogate is clearly seen in one of the pallets as an anomaly in the image (courtesy of K. Borozdin, Decision Sciences).

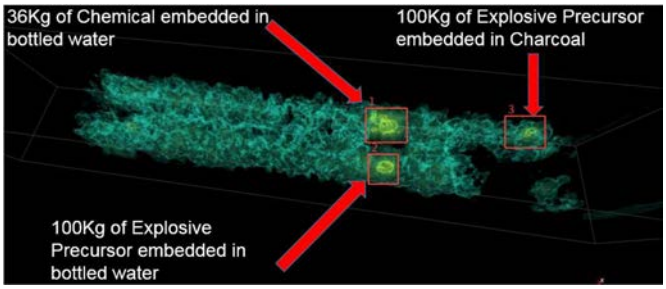

FIG. 47. The muon tomography image of bottled water and charcoal. The image is obtained with a DISCOVERY system installed in Nogales, AZ (USA–Mexico border). Multiple pallets of water in plastic bottles and charcoal in paper bags were put inside a standard shipping container. The pallets had approximate dimensions 1.2 m × 1.2 m and ~2 m tall. An explosive and explosive precursor surrogates were placed inside the pallets. The surrogates had weights of 100 kg and 36 kg. Image exposure time was 10 minutes. The three surrogates are clearly seen as bright anomalies in the image (courtesy of K. Borozdin, Decision Sciences).

8. NUCLEAR WASTE CHARACTERIZATION

8.1. INTRODUCTION

Nuclear waste characterisation is especially suited to the application of muon tomography. Nuclear waste containers are typically heavily shielded and highly engineered to contain radioisotopes and attenuate penetrating radiations. This shielding makes it difficult to apply other non-destructive methods to characterise the contents of the containers. Cosmic ray muons on the other hand are sufficiently penetrating to be used for any nuclear waste container, and the necessity of longer measurement times is usually not a problem as the long-term evolution of the waste characteristics is the primary concern.

Sellafield, in North West England, is Europe's largest nuclear site and houses a diverse range of waste products arising from reprocessing of spent fuel and legacy research facilities. In 2009, the UK Nuclear Decommissioning Authority and Sellafield Ltd. began funding the development of cosmic ray muon tomography for nuclear waste packages by the University of Glasgow and the National Nuclear Laboratory (NNL). A full-scale prototype detector system was successfully tested with a 500 litre Intermediate Level Waste (ILW) drum in 2016. In the same year, the spin-off company Lynkeos Technology was formed. Funding from Innovate UK made it possible to build a CE-certified system, the Lynkeos Muon Imaging System (MIS), and to deploy the system on the Sellafield site. The MIS is the first muon tomography system deployed at a nuclear site worldwide. It has been operational on site since October 2018, without requiring any maintenance during this time. This Section will describe the MIS and the results of tomography campaigns performed with the MIS on wasteforms representative of a selection present on the Sellafield estate.

The MIS comprises two tracking modules using an *x–y* grid of 2 mm diameter scintillating fibres to determine the hit positions of muons (see Fig. 48 and Section 3.2). The design and operation of the system is described in detail in Ref. [102].

FIG. 48. The Lynkeos Muon Imaging System at the NNL Central Laboratory on the Sellafield site (courtesy of R. Kaiser, Lynkeos Technology Ltd).

The incoming and outgoing muon tracks are constructed from the measured muon hit positions and the displacement and scattering angle of the outgoing track are used as input to the reconstruction algorithm [103]. The algorithm produces a 3D representation of the imaging

volume divided into voxels and calculates a scattering density λ (proportional to material *Z* and ρ) for each voxel.

The size of the MIS was driven by the original application to image 500 litre ILW drums. As a result, the active volume of the system is 1 m^3 and the maximum weight of containers is 1 metric ton. The resolution of the system was also optimised for ILW drums; i.e., the scintillating fibre diameter was chosen so that the imaging resolution is mainly limited by multiple scattering of the muons in the active volume, not by the detector resolution.

8.2. STUDIES OF VARIOUS WASTEFORMS

A series of tests on samples representative of typical ILW was conducted to determine the utility of the MIS for such applications. These are outlined below.

8.2.1. 500 litre intermediate level waste drums

A strong motivation for the development of muon tomography for the UK's legacy waste is the many tens of thousands of nuclear waste containers in the form of 500-litre stainless steel ILW drums that exist (Fig. 49). They contain cladding material of fuel rods that was later encapsulated within concrete grout, possibly contaminated with fuel fragments. Swelling of these decaying U fragments over time may threaten the containment, and result in a release. Identifying the presence or absence of fuel fragments within can reduce risks associated with containment breaches, which may require a decontamination and repackaging programme.

FIG. 49. Photographs of the Lillyhall 500-litre ILW drum prior to installation in the prototype MIS at the University of Glasgow. Shown are the four 60 mm-diameter horizontal cores. The two vertical cores are not pictured (courtesy of R. Kaiser, Lynkeos Technology Ltd).

A 500 litre development drum was provided from Sellafield Ltd, which had previously had a quadrant removed. Four horizontal cores of diameter 60 mm were taken out at different heights (Fig. 49). Two vertical cores were removed to allow insertion of material standards.

A small U sample (20 mm diameter, 30 mm long cylinder) was placed in the bottommost horizontal core in an upright position. Lead pieces, measuring ($90 \times 40 \times 20$ mm^3) were inserted into the uppermost core. A total of 24.7 million muons were collected. Fig. 50 shows two 10 mm horizontal image slices through the drum near the locations of the U and Pb samples. Subtle density variations within the concrete and MgO matrix can be discerned. In the U image (Fig. 50a), the high *Z* cylinder has been reconstructed within the core in the open face with the correct 20 mm diameter. The shadow of some of the supporting structures can also be seen. In

the other slice, the rectangular arrangement of Pb can be seen (Fig. 50b) in the same location but with a lower density than that Fig. 50a.

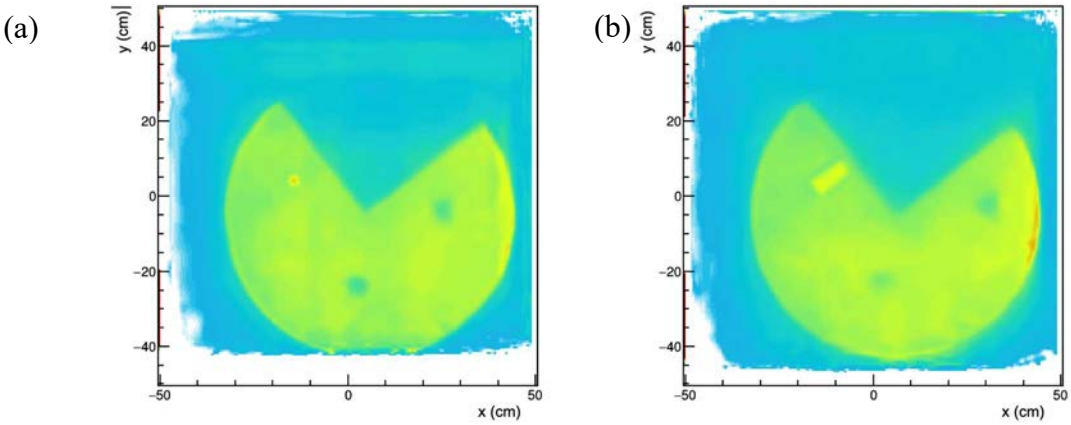

FIG. 50. (a) A 10 mm thick horizontal slice through the 500 l ILW drum with 20 mm diameter U cylinder. (b) A 10 mm horizontal slice throughout the drum with 90 mm long Pb pieces. The horizontal resolution is about 3 mm (courtesy of R. Kaiser, Lynkeos Technology Ltd).

Both slices show apparent signs of a high-ρ material at the right-hand side wall of the drum due to noisy readout channels from a multi-anode photomultiplier tube that yield a false, high detection rate of muons. This issue was later remedied to remove such artefacts.

8.2.2. GeoMelt in-situ vitrified waste

Thermal treatment technologies have developed for intermediate and high level wastes over many years. One such process is GeoMelt, developed by Battelle, since applied to in-situ, in-container and in-cell applications. To date, GeoMelt has been used for the treatment of 26,000 tonnes of waste, mostly via in-situ vitrification.

In-container vitrification is flexible enough to be used for melts from less than a kilo to more than 80 tonnes. A reusable in-container vitrification container is filled with a refractory box as the primary containment for melt products. Waste mixed with granules of borosilicate glass is melted into a single block within the refractory box. Convective mixing that takes place naturally during melting assists in the homogenization of the product.

The GeoMelt containers used for the NNL tests are 100 × 100 × 68 cm^3 in size and weigh close to 1 ton. Due to the thickness of the material, muon tomography is the only applicable non-destructive imaging technique for quality assurance purposes. In fact, muon tomography makes it possible to optimise the operational parameters of the process. The following are three examples of different GeoMelt samples [104].

Sample A was a thermally treated product consisting of a steel ‘top hat’, partially filled with a non-active U analogue (a mix of Ca and La) and dry, aged grout cement (Fig. 51). Steel ‘top hats’ (20 mm thick, 300 mm diameter, 550 mm high containers of stainless steel) are commonly used in the nuclear industry. Sample A was imaged using the University of Glasgow’s prototype MIS which collected 21.3 million muon triggers over a period of ca. 27 days.

The proprietary muon reconstruction software developed can produce 3D rendering of images: Fig. 52 reveals an area of higher density within the thermally treated product, indicating that incomplete melting of the contents had occurred.

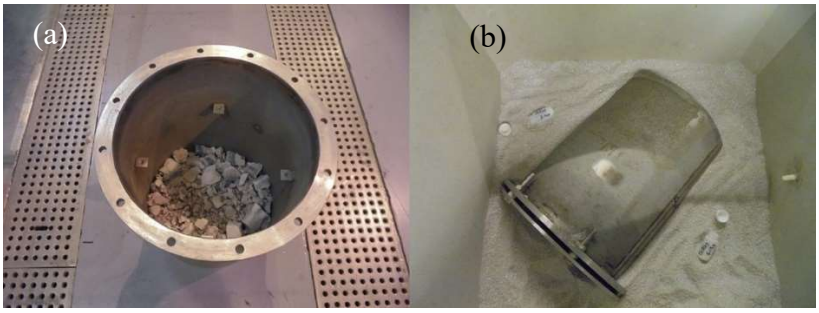

FIG. 51. Sample A – (a) steel top hat containing mischmetal and dry aged grout, filled and then (b) placed in the cast refractory box (courtesy of R. Kaiser, Lynkeos Technology Ltd).

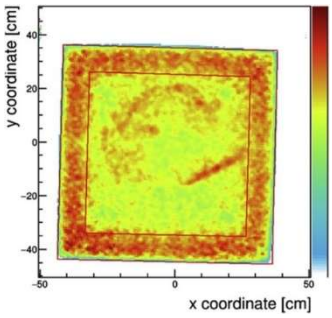

FIG. 52. A 10 mm slice through Sample A, 50 mm above the inner base of the refractory box showing a region of higher density. The colour scale represents relative density on a log scale from 1.0 to 1.8 (courtesy of R. Kaiser, Lynkeos Technology Ltd).

Sample B was another non-active melt specimen consisting of an open topped, cubic, mild steel box. This acted as a scale model for steel skips in use in ponds at Sellafield, which typically weigh ~11 kg and contain 28 kg of corroded Magnox sludge (predominantly $Mg(OH)_2$). It is representative of many mixed beta/gamma waste streams, especially skips in the First Generation Magnox Storage Pond at Sellafield. This was measured at the prototype MIS at Glasgow over ca. 22 days.

Sample C consisted of U pennies, loosely stacked in nine columns inside a small steel box, which in turn was place inside a steel skip. Fig. 53 shows photos of the setup.

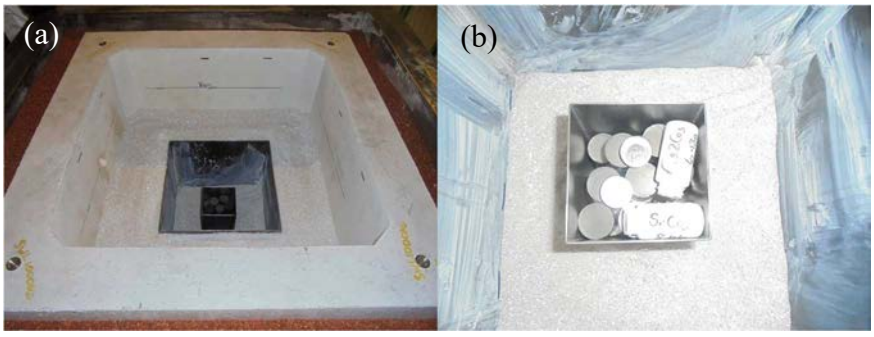

FIG. 53. Photo of the small steel box inside the steel skip for Sample C (a) and of the stacked U pennies inside the box (b) (courtesy of R. Kaiser, Lynkeos Technology Ltd).

The data for Sample C were collected using the MIS system at the NNL Central Laboratory, Sellafield, UK. The GeoMelt sample was placed inside the muon detector system by NNL staff. The sample was positioned roughly in the centre of the detector imaging volume. Initially, it was rotated around the *x*-axis by 90 degrees and measured for a period of 13 days. After that it

was rotated back to its normal orientation and measured for another 8 days. A total of 14.2 million muon tracks was collected. Horizontal and vertical slices through Sample C are shown in Fig. 54. The λ value allowed the identification of the material as high-*Z* material; i.e., nuclear fuel or U. The nine stacks of U pennies are clearly visible; however, the steel box and skip appear to have melted. In fact, a closer investigation showed a layer of metal at the bottom of the cast refractory box.

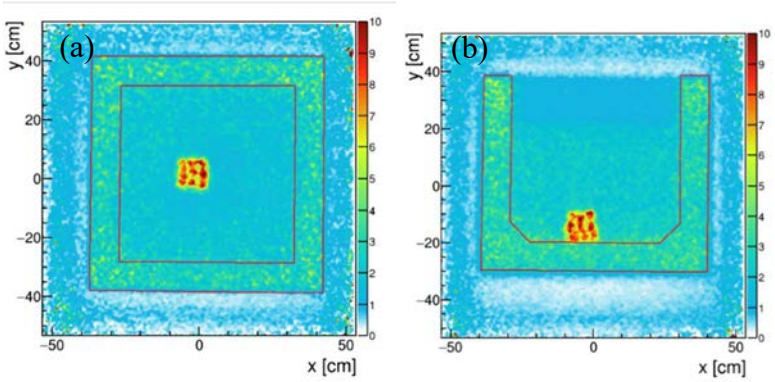

FIG. 54. (a) A 10 mm horizontal slice through Sample C and (b) 10 mm vertical slice through the centre of Sample C. The nine stacks of U pennies are clearly visible (courtesy of R. Kaiser, Lynkeos Technology Ltd).

8.2.3. Condition monitoring of retrieved sludges

The Magnox Swarf Storage Silo (MSSS) at Sellafield was used to store ILW from Magnox reprocessing for four decades. Due to corrosion, much of the waste has formed a sludge, and to accelerate risk reduction Sellafield Ltd. has begun a programme of work to retrieve material from the MSSS compartments and store it in a new facility for an interim period prior to long-term disposal. During the interim period, there is a need to monitor the wastes for any changes that might compromise the integrity of the storage containers.

The standard package for MSSS retrievals is the 3 m^3 box [106]. It comes in a side-lifting and a corner-lifting variant, but both have the basic construction in common – a double wall construction with an inner skip and an outer container, both manufactured from 6 mm thick steel. The space between the outer and inner wall will be filled with grout. Waste material is placed in the inner skip and topped off with water.

From 2018 to 2020, preliminary studies to assess the performance of muon tomography for MSSS waste condition monitoring were undertaken. The primary concerns were the ability to measure the waste and water fill levels and detecting deformations in the skip walls. A full-size 3 m^3 box is too large for the current MIS geometry and with a weight of more than 4 tons also too heavy for the sample table. To enable measurements, a scaled down version that could fit within the imaging volume of the MIS was designed and fabricated.

As with full size MSSS packages, the small-scale box comprises an inner and outer container, both made from S275 grade steel. The outer container is 76 × 76 × 76 cm^3 in *x*, *y* and *z* with a 3 mm thick lid, an 8 mm thick base and 6 mm thick walls. The inner container is 55 × 55 × 65 cm^3 in *x*, *y* and *z* with a 2 cm thick lid. Concrete paving blocks were placed beneath the inner container and concrete blocks placed in the interstitial space between the inner and outer containers to replicate the grout lining of a full-size box.

One of the inner skip walls was deliberately deformed with a bulge of 1 cm over its length to simulate a deformation due to waste expansion. A steel shelf was placed at a height of

approximately 32 cm in the inner container, dividing the skip into two compartments allowing several different waste types to be imaged at once and maximising the amount of data which could be acquired in a single imaging trial.

Sludges of different density were contained in 6 litre plastic jerry cans measuring 19.4 × 14.6 cm^2 at the base and 29.4 cm in height. The jerry cans were placed in the lower compartment of the small-scale inner skip. In addition to the sludges, different materials to simulate miscellaneous beta–gamma waste and high-*Z* material were added to the upper compartment of the skip. The materials were:

- Two bags of partially corroded swarf, one of which contained three small pieces of W;
- A waste bag containing wood, plastic tubing, a paint tin, rags, a steel bolt and two 10 cm W rods;
- A cardboard box containing the remaining W rods.

The material positions in the inner skip are shown in Fig. 55 (the deformation in the left-hand wall of the inner skip can be seen in this image).

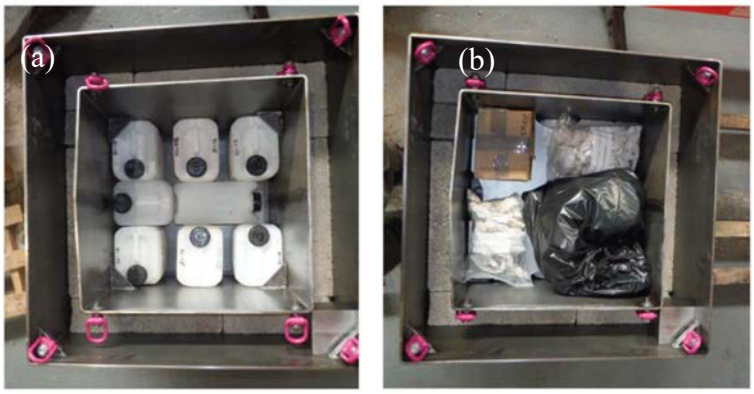

FIG. 55. Materials in the inner skip showing: (a) the jerry cans in the lower compartment; and (b) the bags of swarf, box of W and waste bag of miscellaneous beta-gamma waste (courtesy of R. Kaiser, Lynkeos Technology Ltd).

8.2.3.1. High-Z mass reconstruction

More detailed analysis of the W regions (Fig. 56) revealed the location precision of the W pieces to better than 3 mm. A lower density object, most probably the steel bolt in the miscellaneous waste bag, is observed on the right-hand side of Fig. 56. There are indications in the bottom left corner of the upper compartment of a material with a density that is higher than background. This is consistent with the bag containing swarf.

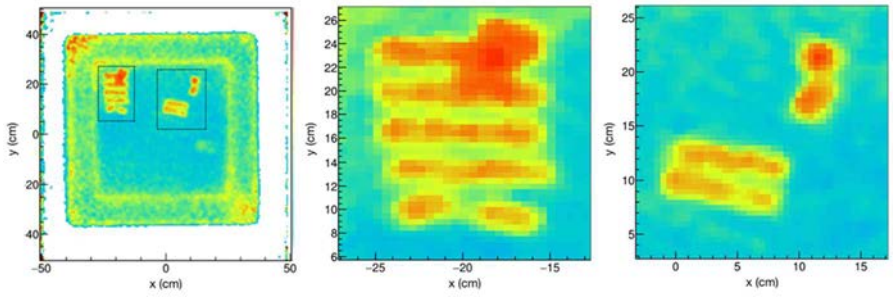

FIG. 56. A 1 cm slice through the skip showing the presence of high-Z materials (courtesy of R. Kaiser, Lynkeos Technology Ltd).

The total mass of the W present has been estimated by summing the λ values in the high *Z* region and subtracting a background generated from a W-free area. The mass estimated was 10.5 ± 0.5 kg. The two pieces of W in the middle image of Fig. 56 have a length of 10 cm and a diameter of 3 cm, with a mass of 2.72 kg. The reconstructed mass for these two rods was 2.37 kg; i.e., accurate within 13%.

8.2.3.2. Identification and measurement of container deformation

The position of the 1 cm deformed wall has been reconstructed by locating the peak λ values within a range of voxels in the relevant areas and a Gaussian fit used to determine the position of the peak. To reduce the statistical error, a sum of the λ values along the vertical length was used to evaluate the peak position. The results are shown in Fig. 57. The red bands indicate the known positions of the walls. Error bars on the data represent the width of the volume elements. The 1 cm deformed wall is clearly shown, as is the straight wall. The small slope in the results for the straight wall results from the slight angle at which the box has been loaded into the MIS.

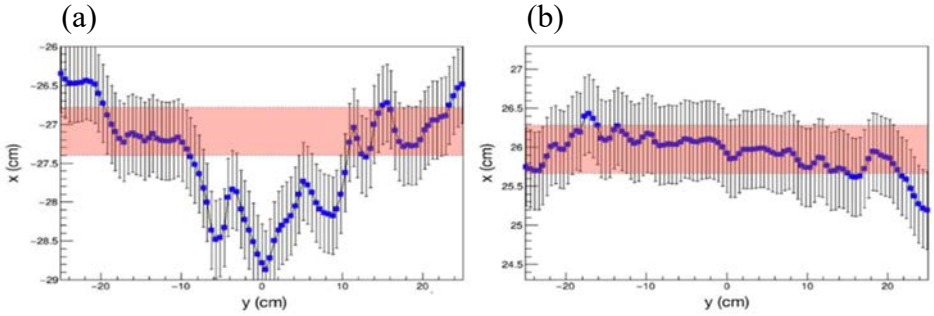

FIG. 57. Reconstructed centre position of the inner skip wall along the vertical y axis for (a) deformed wall (b) and the straight wall (courtesy of R. Kaiser, Lynkeos Technology Ltd).

8.2.3.3. Material fill level measurements

The average λ value of each of the sludges can be calculated over the volume of the jerry cans. The reconstructed value for two samples, which were filled with the same density of sludge to the same level, were consistent with each other, and there was a correlation between the fill levels determined for samples of the same density and the value of λ. In practice, neither the fill level nor ρ will be known, so reference materials in the imaging volume and a look-up table would be required to calculate level measurements.

The results described above attempted to indirectly estimate the fill levels for the different materials present. However, direct accurate measurements of material positions in the plane of muon travel are difficult due to large uncertainties on the scattering position caused by the small magnitude of the scattering angle. To measure the position of vertical material boundaries directly, the solution is to make use of muons at larger zenith angles which will require detectors placed horizontally to each side of the container, rather than above and below as is the case with the current MIS design. A GEANT4 simulation of horizontal detectors imaging a full-size $3m^3$ box shows that measurement of the heights of different materials is achievable.

At present, no horizontal configuration of the MIS exists. To confirm the capability of measuring material boundary positions it was decided to stack plastic sheets of different densities inside the small-scale MSSS container, and then to rotate the container such that the boundaries between different layers appear horizontal to the vertical detectors.

Two types of plastic were used: UPVC ($\rho = 1.45$ g/cm^3, ~20–30% larger than the sludge densities described above) and PE300 ($\rho = 0.96$ g/cm^3, similar to the density of water). A stack of UPVC sheets were placed in the bottom of the small-scale container to a height of 30 cm, and a 20 cm stack of PE300 sheets was placed on top of the UPVC stack. The MIS at Glasgow University was used to image this sample configuration. Fig. 58 shows the plastic sheets used and the rotated box, with the top of the PE300 stack visible, in the MIS at Glasgow.

Four and a half days of muon data was acquired with the plastic stacks in the small scale-container. A background data set was taken for 12 days using the empty container.

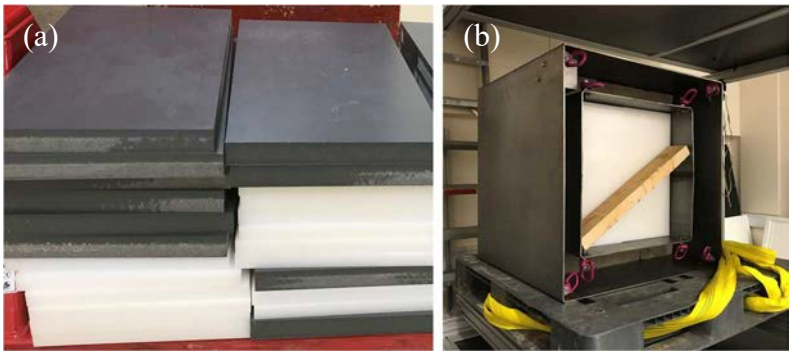

FIG. 58. (a) Sheets of UPVC (dark grey material) and PE300 plastic (white). (b) The rotated container inside the Glasgow MIS (courtesy of R. Kaiser, Lynkeos Technology Ltd).

Only muons satisfying the following angular selections were used in the image reconstruction and analysis: $-15° < \theta_x < 15°$ and $-7.5° < \theta_y < 7.5°$, where θ_x is the angle in the x-z plane between the projected muon track and the z axis (the vertical direction, normal to the detector plane) and θ_y is the angle between the y-z plane and the z axis. These limits are necessary to form as near to a parallel beam as possible, to improve the resolution of the measurement of the position of the phase boundary, while at the same time achieving sufficient statistics.

The position of the phase boundary is determined from the change in measured scattering density. From a plot of scattering density, λ, against distance, it can be seen that the phase boundaries manifest as edges in the data. The phase boundary position is measured as the half maximum point on these edges. The results of the material fill level analysis from experimental and simulated data are shown in Fig. 59. The boundaries between the plastics are clearly identified.

To measure the boundary positions and estimate the resolution of the position measurements, the experimental data were split into ten different data sets, each of them containing 11 hours of data. The PE300/air boundary is reconstructed at $y = -18.6 \pm 0.7$ cm. The PE300/UPVC boundary is at $y = 2.66 \pm 1.06$ cm and the UPVC edge at the bottom of the skip is at $y = 33.26 \pm 0.87$ cm. In other words, the thickness of the UPVC (30 cm) is reconstructed as 30.6 cm and the thickness of the PE300 (20 cm) is reconstructed as 21.26 cm. A GEANT4 simulation of the experiment was performed and took account of muon hit position resolution and alignment errors. Very good agreement between simulation and experiment is observed (Fig. 59).

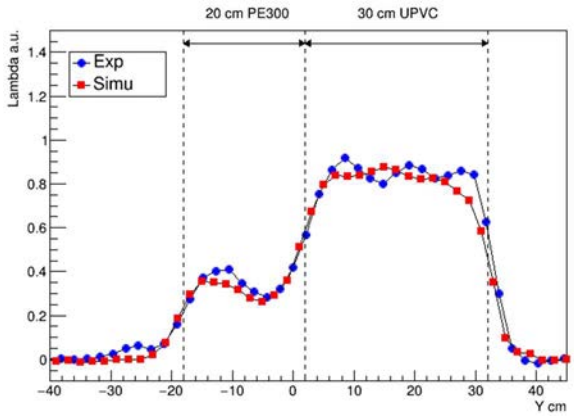

FIG. 59. Experimental and simulated measurements of the fill levels of the different plastics in the small-scale container (courtesy of R. Kaiser, Lynkeos Technology Ltd).

The apparent peak at –11 cm (Fig. 59) is caused by the concrete shielding of the mini MSSS box. This is because the measured scattering density of a material can be affected by the materials above and below it, which, in turn, is because muon tomography is a limited angle tomography problem, which causes distortions in the reconstructed image. This effect is nonlinear, hence even after background subtraction there are still some residual effects. However, as demonstrated above, this does not degrade the ability to determine the phase boundary position.

8.3. NUCLEAR WASTE DRUM STUDIES

The H2020 funded CHANCE project[23] addresses some as yet unsolved and specific issues of the non-destructive assay of large casks of conditioned and often heterogeneous radioactive waste. An independent and non-invasive verification of the radionuclide content declaration and checking the location of some specific items of radioactive waste buried in a large cask is hitherto a regulatory challenge.

One of the novel measurement techniques studied within CHANCE is muography for non-destructive interrogation of the composition and location of radioactive waste in large volume casks [105]. The cosmic ray nature of muon particles as a natural and ubiquitous probe of extreme penetration depth and weak interaction with matter make muon scattering and radiography a powerful candidate to provide proper answers to the three basic questions of radioactive waste management:

(i) What is it?
(ii) Where is it?
(iii) How much is there?

Muography is passive, works when applied to heavily shielded volumes, and is complementary to gamma and neutron tomography. The technique readily detects heavy elements (e.g., lanthanides and actinides) but can also detect density gradients or differences within a material matrix, such as voids and gas bubbles.

8.3.1. The CHANCE consortium

The Universities of Sheffield and Bristol have built a large muon system, which is operated in a non-laboratory environment. It is protected from rain, but neither humidity nor temperature

[23] EU Horizon 2020 grant agreement number 755371, https://cordis.europa.eu/project/id/755371

controlled; hence, the environmental conditions are likely similar to the ones in field deployment. The system (Fig. 60) is a combination of both Resistive Plate Chambers (RPC) and drift chambers, connected to a set of scintillator trigger paddles. The RPCs [106] were designed and built at the University of Bristol, and currently run-on CO_2 gas.

Each RPC layer is a combination of three large 60 × 180 cm^2 area detectors providing a hit position in one dimension with a resolution of ~350 μm. The next layer is rotated 90° around the z-axis to reconstruct three-dimensional hit positions in the upper and lower parts of the detector. Similarly, three layers of drift chambers are arranged along the x-axis while another three are arranged along the y-axis. The six layers together provide muon hit positions with a resolution of ~2 mm. The combination of the information about the muon hits from both the drift chambers and RPCs provide an excellent tracking and measurement of the scattering angles with high precision. The full system is now being commissioned, and a large GEANT4 simulation study is ongoing.

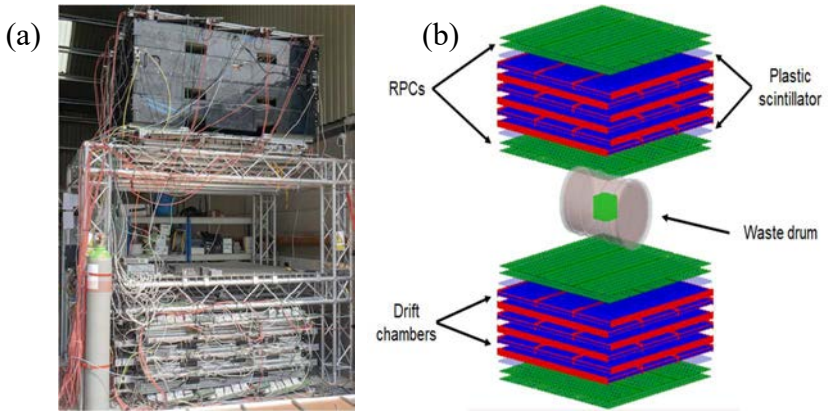

FIG. 60. (a) The CHANCE MST detector system covering an area of approximately 1.8 × 1.8 m^2. The upper and lower detector stacks each have three layers of drift chambers and two RPC layers. The upper stack also contains two layers of plastic scintillators used as triggers (b) Visualization of the CHANCE detector system using a GEANT4 simulation framework (courtesy of the CHANCE consortium).

8.3.2. Metric method

In this study, the metric method presented in Ref. [107] was used, which divides the sample volume into voxels of side 10 mm. High angle muon scattering occurs more frequently in dense material than in less dense material. Therefore, the vertices associated with high angle scattering are closer together in high-Z lumps than in low-Z lumps. For each pair of vertices within a voxel, a weighted metric value, m_{ij}, is calculated, representing the distance between each pair of vertices in that cubic bin, normalized by scattering angle and momentum:

$$m_{ij} = \frac{|v_i - v_j|}{(\theta_i \widetilde{p_i}) \cdot (\theta_j \widetilde{p_j})} \quad (1)$$

where v_i is the position of the i vertex, θ_i is the scattering angle and $\widetilde{p_i}$ is the momentum of muon i. When using this algorithm, it is assumed that the muon momentum is known, representing an 'idealised' MST system with precise momentum measurement capabilities. A good measure of muon momentum could be achieved through measurements of the muon scattering in material of known thickness, either between the layers of the lower detector module, or additional inserted layers of material. The median ('discriminator') of the m_{ij} is determined for each cubic bin. This method is known as the 'binned cluster algorithm'.

8.3.3. Void detection in nuclear waste containers

In some countries, low and intermediate level waste was historically stored in steel containers along with bitumen in some countries. Irradiation of bitumen by nuclear waste produces hydrogen gas, which can aggregate into bubbles and the resulting swelling may cause rupture of the containers and release of waste. Techniques that can detect and quantify gas within containers are, therefore, of interest.

Bubbles can be located by analysing individual image slices, permitting discrimination between single, big bubbles and sets of smaller bubbles. In the example here, the drum was divided into 2 cm slices along the *x*-axis (the central axis of the cylindrical drum). For every slice, the mean value of the discriminator distribution, μ_{discr}, was calculated for three different geometries:

(i) A concrete-filled drum with no bubbles;
(ii) A concrete-filled drum with one bubble in the centre of the drum;
(iii) A concrete-filled drum with two equal size bubbles, each of half the volume of case (ii) (Fig. 61).

The mean values at the edges of Fig. 61 represent the air outside the drum and the steel caps. The values of μ_{discr} within the drum are the same for scenarios (i–iii), except for where the bubbles are present, where the value of μ_{discr} exceeds that of concrete. The difference is greater for larger bubbles, and this can be used to determine the location of the bubbles: a single large bubble can be distinguished from a two-bubble scenario.

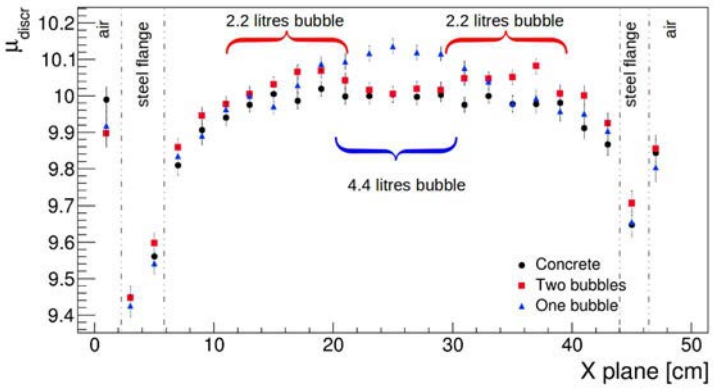

FIG. 61. The concrete-filled drum filled with no bubbles (black circle: scenario i), with a 4.4 litre bubble (blue triangles: scenario ii), and two 2.2 litres bubbles (red squares: scenario iii) (courtesy of the CHANCE consortium).

Gas bubbles can occur close to blocks of material. Three different cases involving a drum filled with concrete were tested:

(i) A concrete-filled drum with no bubble;
(ii) A 2-litre bubble placed in the centre the drum, adjacent to a 3 × 3 × 3 cm^3 U cube;
(iii) A 2-litre, single bubble in the centre of the drum.

Fig. 62 shows the U block (with a characteristically lower value of μ_{discr}) while the adjacent bubbles can be discriminated due to their higher values. For more details see Ref. [108].

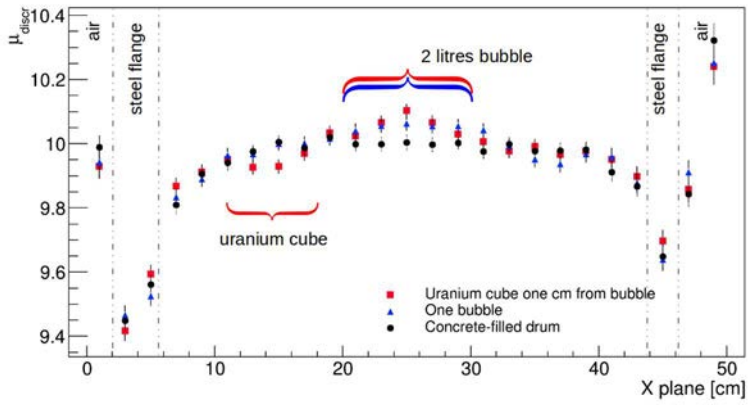

FIG. 62. The concrete-filled drum with solid concrete (case i), containing a 2-litre bubble and U block (red squares, case ii), and a single 2 litre bubble (blue triangles, case iii), (courtesy of the CHANCE consortium).

8.3.4. Material identification in nuclear waste drums

Muon Scattering Tomography performed over days to weeks can yield 3D images in which individual objects can be seen within the drum as well as give information on the Z and ρ of the objects. Ref. [109] reports the training of MultiVariate Analysis (MVA) classifiers on simulated MST data to discriminate between Pb and U blocks within filled drums.

The MVAs were trained on simulated data corresponding to 10 day exposures of four waste drums: an 'empty' drum containing only solid concrete, and three drums containing cubes of Fe, Pb and U (20 cm on each side) placed at the centre and aligned with the cylindrical axis of the drum. Only the voxels in the cubes (or their equivalent for the 'empty' drum) were passed to the classifier (see Section 8.3.1).

Binary classifiers use one dataset of voxel variables as 'signal' and the other 'background'. Non-binary classifiers receive a single signal dataset along with multiple background datasets. The classifiers attempt to distinguish signal voxels from background(s) voxels, such that when applied to a new voxel it will be classified correctly as often as possible. An optimum 'cut' (threshold) value is calculated from the classifier: responses above are 'signal-like' and those below 'background-like'. The non-binary concrete classifier's training outputs and a plot known as a Receiver Operating Characteristic are used to assess the diagnostic ability of the classifier (see Fig. 63).

Next, the method was applied to a simulated drum this time containing three 15 cm side length cubes of three materials: U, Pb and Fe (Objects 1 to 3 in Fig. 64). The MVA correctly assigns the largest material value to the true material for each Object, and the values for the U and Pb blocks are also clearly distinguished from each other.

The results depend on the size of the objects. To quantify the relations between the object size and the material values, the system was applied to a series of simulated drums containing spheres of different materials and increasing radius (Fig. 65). This demonstrates that the sizes of the objects can be extracted from the MST data, and, therefore, the volume effect can be taken into account.

(a)

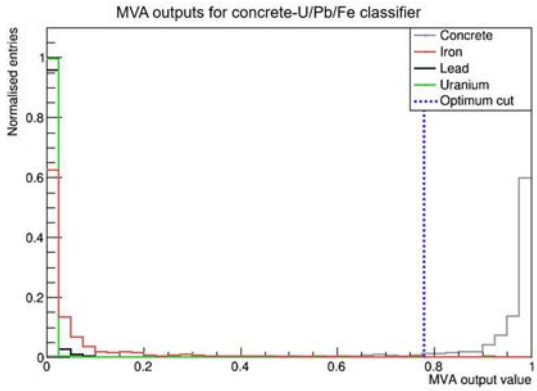

(b)

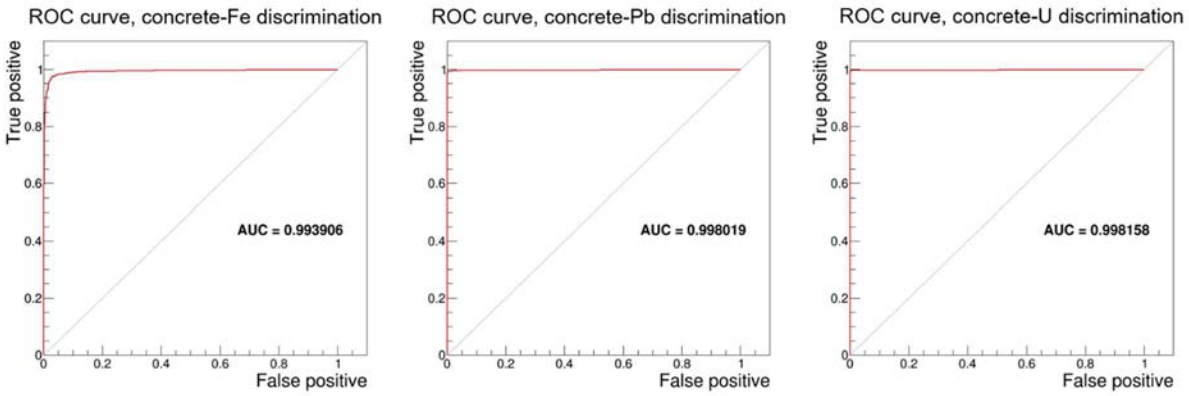

FIG. 63. (a) MVA training outputs and (b) ROC curves for concrete vs Fe/Pb/U nonbinary classifier. ROC = Receiver Operating Characteristic, AUC = Area Under Curve (courtesy of the CHANCE consortium).

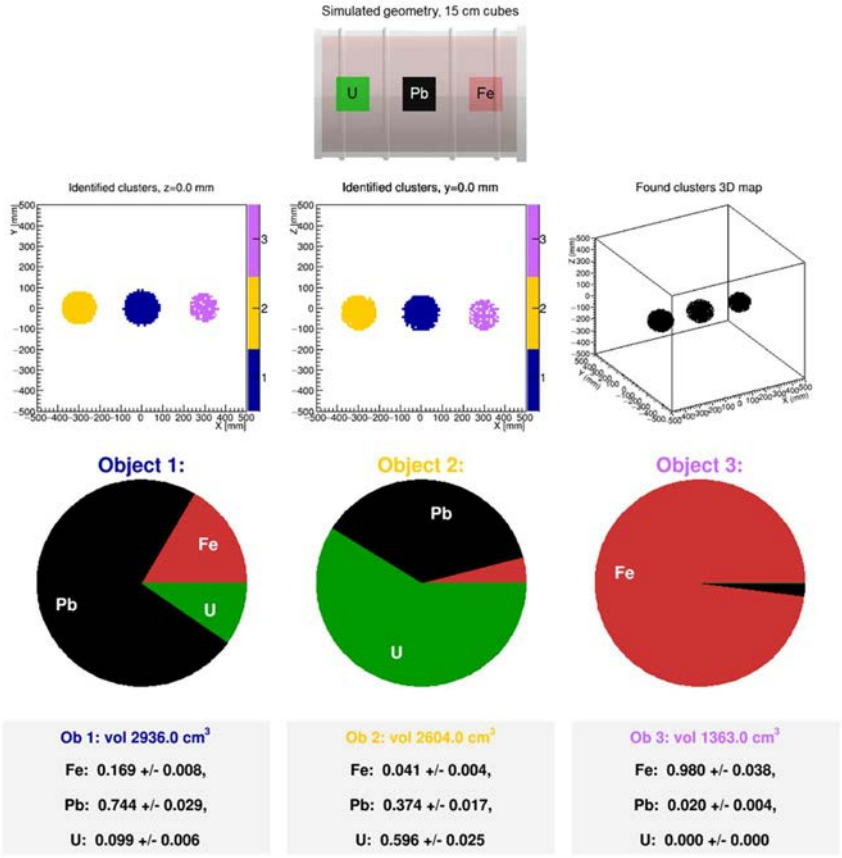

FIG. 64. Material estimates results for the simple geometry of three 15 cm cubes, U, Pb and Fe, aligned with a voxel grid (courtesy of the CHANCE consortium).

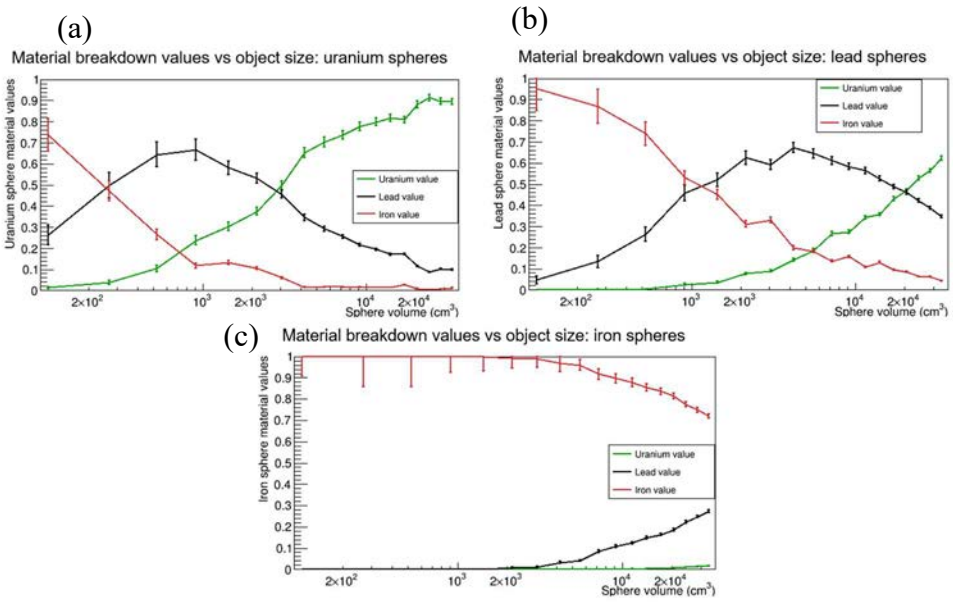

FIG. 65. Relationship between the material breakdown values and size for a single sphere of increasing radius of (a) U, (b) Pb or (c) Fe (courtesy of the CHANCE consortium).

Fig. 66 shows the results from a drum of five objects (two U, two Pb, and one Fe) in a broad range of shapes dispersed more evenly within. The system still performs well, and the identified clusters closely match the true locations of the objects. Only one Pb object was incorrectly assigned: it was a tube that the system identified as Fe, demonstrating a limitation in determining the composition of less-spherical objects.

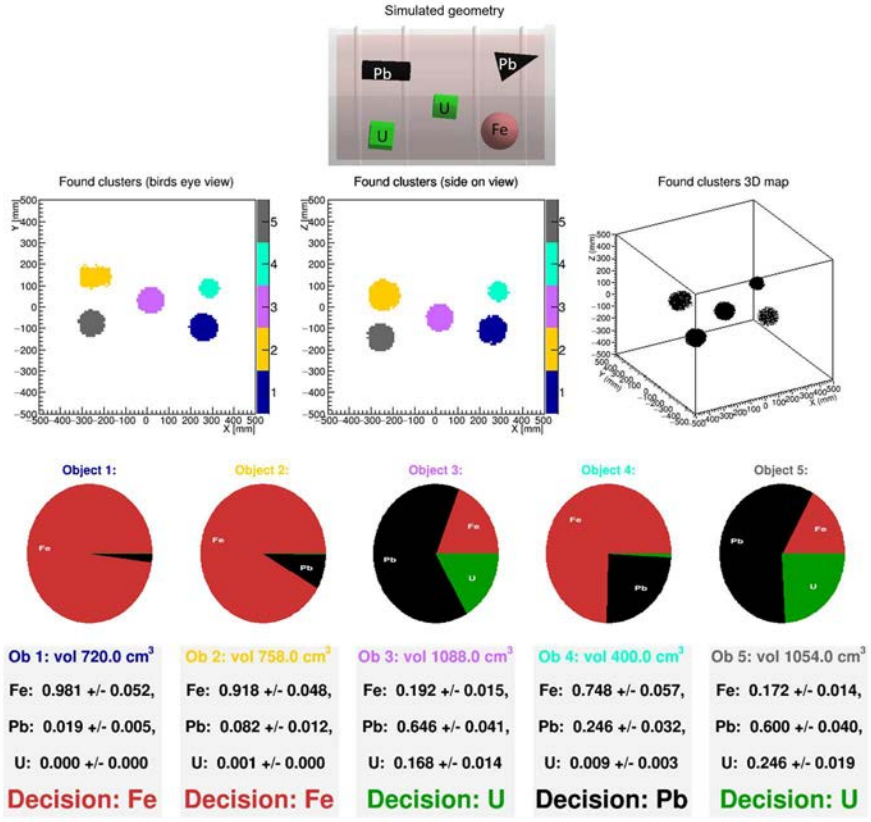

FIG. 66. Material estimates for five irregular objects dispersed through a drum. Four of the objects have been assigned the correct material; one Pb object has been incorrectly classified as Fe (courtesy of the CHANCE consortium).

The sensitivity and false positive rate of the system were then tested via randomly generated simulations. Each simulation had three non-intersecting spheres (radius 6 cm) dispersed through the drum. One hundred simulations were run in total; half contained U, Pb and Fe spheres, and half contained only Pb and Fe spheres. The following identification scheme was used:

- A positive identification is when a U object is identified close to the true location of a sphere given a U decision value;
- A false positive is any U decision value assigned to an object not containing U.

A sensitivity of $0.90^{+0.07}_{-0.12}$, and a false positive rate of $0.12^{+0.12}_{-0.07}$ was achieved [110].

9. NUCLEAR SAFEGUARDS AND MATERIAL CONTROL

9.1. NUCLEAR SAFEGUARDS

Nuclear safeguards are technical means by which legal undertakings not to acquire or use nuclear material (U, Pu, and Th), nuclear facilities and/or related items for proscribed purposes are verified. Nuclear inspectorates, such as IAEA, EURATOM or governmental organisations, perform safeguards verifications during inspections in different nuclear fuel cycle facilities. The main objective of IAEA safeguards is the timely detection of diversion of significant quantities of nuclear material from peaceful nuclear activities to the manufacture of nuclear weapons, other nuclear explosive devices, or for purposes unknown, and deterrence of such diversion by the risk of early detection.

Some of the in-field measures used to implement safeguards are containment and surveillance, and verification of nuclear material by destructive analysis or non-destructive assay (NDA) measurements. Continuity of knowledge of nuclear material and facilities under safeguards is typically maintained during periods between verifications using containment and surveillance measures.

Many NDA techniques used in safeguards are based on measurement of ionising radiation emitted by nuclear materials and are used by safeguards inspectors at all stages of the fuel cycle. Well-established NDA instruments and techniques may permit quantification of the nature, isotopic composition, and quantity of nuclear material, depending on where in the fuel cycle it is found, and any protective measures required to work around it. In the case of spent fuel dry storage facilities, precise NDA measurements may not be possible due to cast Fe or heavy concrete shielding, which significantly attenuates the radiation emitted by spent fuel, or due to significant self-shielding effects of the nuclear material itself.

The number of Dry Storage Casks (DSC) is constantly increasing. In the coming decades it may grow to tens of thousands worldwide [111]. This can become a serious challenge for safeguards inspectorates, as presently no sufficiently precise method is available filling the potential need for reverification of spent fuel contained in DSCs. The possibility of loss of continuity of knowledge cannot be excluded over the long term (50 years or more). The situation may become a pressing issue in states where no on-site installation will be available to open spent fuel casks for reverification purposes. In such a case, reverification of nuclear material inventory of closed DSCs, using NDA, would be crucial. Operation and maintenance of containment and surveillance techniques may require significant resources and can be associated with dose uptake for both safeguards inspectors and the operators of storage facilities with DSCs. For planning purposes, the IAEA uses ‘significant quantities’ (SQ) to establish its inspection goals. One SQ is an approximate amount of nuclear material for which the possibility of manufacturing a nuclear explosive device cannot be excluded; one SQ of plutonium is 8 kg and one DSC can contain several SQs, making it a significant object from a safeguards point of view. Thus, the nuclear inspectorates are looking at possible new NDA techniques that are able to detect the diversion of nuclear material from DSCs. For traditional reactor fuel, one SQ could represent one pressurized water reactor spent fuel assemblies, or 3-4 boiling water reactor spent fuel assemblies, or about 100 CANDU spent fuel bundles.

9.1.1. Verification of fuel assemblies stored in a CASTOR V/52 cask

In addition to the work performed on waste drums (Section 8.3.1), the CHANCE consortium has been involved in examining applications to verification of fuel assemblies in CASTOR V/52 casks. The CASTOR V/52 cask consists of a monolithic body made of ductile cast iron,

a fuel assembly shaft with 52 box-shaped shafts (length, width and height of 13 cm, 13 cm and 448 cm) for storing the fuel assemblies and a bolted double lid system.

In order to compare the performance of the algorithmic methods in imaging the fuel assemblies inside the CASTOR cask, simple tests are used to compare the different regions inside the CASTOR quantitatively. The feature resolution test is used to examine the ability of the algorithms to distinguish the fuel assembly of each fuel assembly shaft individually and to separate these from those of the neighbouring shafts. A number of shafts have been filled up to 50% of their normal capacity and located randomly throughout the CASTOR to test the size resolution.

A contrast-to-noise ration method is developed and applied to the regions containing different fuel assembly shafts accommodating the fuel assemblies (Fig. 67).

- A fully loaded fuel assembly shaft;
- A half-loaded fuel assembly shaft (the central UO_2 pellets inside the fuel assembly shaft are removed on purpose);
- A half-loaded fuel assembly shaft (the UO_2 pellets to the side of the fuel assembly shaft are removed on purpose);
- A Pb fuel assembly shaft (the UO_2 pellets are replaced with Pb pellets for testing purposes);
- An empty fuel assembly shaft.

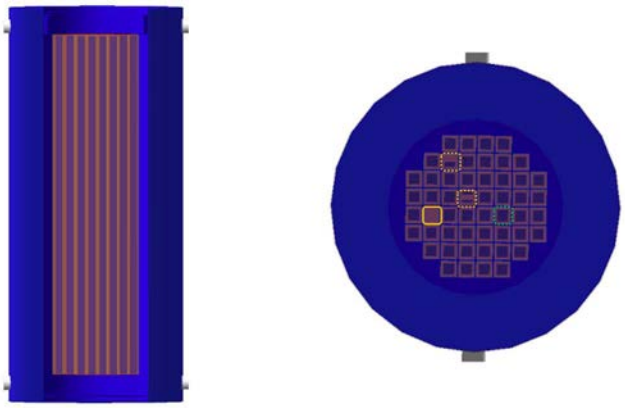

FIG. 67. The top and the side views of the simulated CASTOR V/52 accommodating 52 fuel assembly shafts. The yellow-dashed lines represent the half-loaded fuel assembly shafts, and the green-dashed line represents the fuel assembly shafts that accommodate Pb pellets, and the yellow-solid line represents the empty fuel assembly shaft (courtesy of the CHANCE consortium).

The Angle Statistics Reconstruction (ASR) algorithm is used [112], which was developed to overcome the limitations of the POCA single-scatter approximation. This is achieved by only considering the muon trajectories that enter and exit the volume of interest in the voxels that lie within a chosen minimum distance of these trajectories. For each voxel on the map, the projected scattering angles on the *x*-axis and *y*-axis are calculated to obtain a set of scores, which are the products of the scattering angle in the *xz* and the *xy* plane multiplied by the muon momentum. A distribution of the score is obtained for each voxel. Several quantiles (ASR [0.50] and ASR [0.25]) of the distributions inside each voxel are considered to determine the final discriminator values that convey information about the object inside the volume of interest.

Fig. 68 shows the output for ASR [0.50] and ASR [0.25] for the cask shown in Fig. 67. A comparison of the plots clearly shows that the method can detect the differently filled fuel assembly shafts. For more details see Ref. [113].

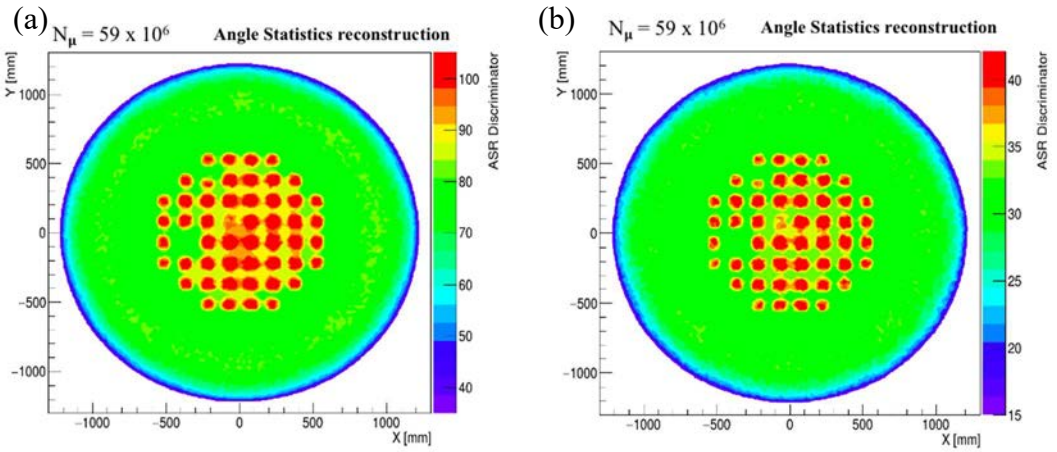

FIG. 68. (a) The ASR output of the fuel assembly feature resolution when 50% of the ASR distribution in each voxel is considered. (b) shows the result of accounting for only 25% of the ASR distribution in each voxel (courtesy of the CHANCE consortium).

9.1.2. Verification of fuel assemblies stored in a CASTOR V/19 cask

Other teams have also been involved in developing muon imaging applications in this area. In a DSC designed to reduce emitted radiation, a large amount of material is present not only in the spent fuel assemblies but also in its structure. As a consequence, it is possible to use the non-negligible rate of absorbed muons as an additional technique to be used together with the MST. Since the absorption rate depends approximatively on the density of the material crossed by muons while the MST is sensitive to the product of ρ and of *Z*, a combination of the muography and MST techniques can give a map of *Z* of the material contained in the cask.

In order to study the cask content, muon detectors capable of measuring charged particle position and direction have to surround the cask. In such a way, muons can be detected when they enter and when (if) they exit from the cask.

Several simulation data have been produced generating cosmic muons that cross a DSC according to their characteristic energy and angular spectrum. Studies based on such simulation data show that the techniques are able to detect the absence of spent fuel assemblies. With a detector placed around a cask, missing assemblies could be detected with a very large statistical precision using a dataset of muons corresponding to less than two days of data collection [114]. In addition, it has been shown that a detector with a limited acceptance could also be used to study the content of a cask [115] provided the detector modules can be rotated as shown in Fig. 69.

A cask with two missing assemblies has been simulated within GEANT4 and a set of simulated cosmic muons corresponding to 12 hours of data collection in each position has been produced (Fig. 70). The analysis used to reconstruct the DSC content is based on the absorption rate and it shows that the absence of fuel assemblies can also be detected with a prototype having a limited acceptance, as shown in Fig. 69.

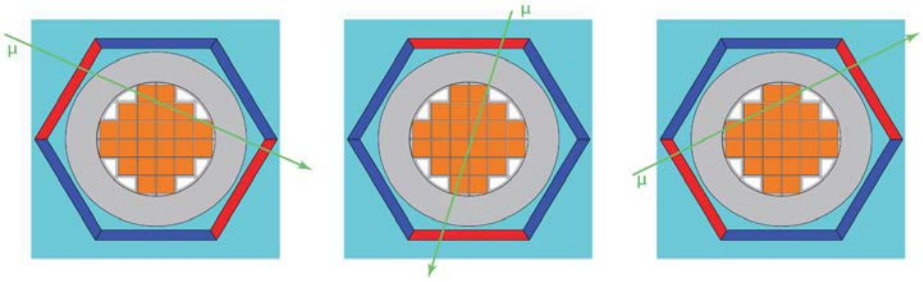

FIG. 69. Schematic view of the positions (rotated by 60°) of the detectors (in red) used to study a DSC (reproduced from Ref. [115]).

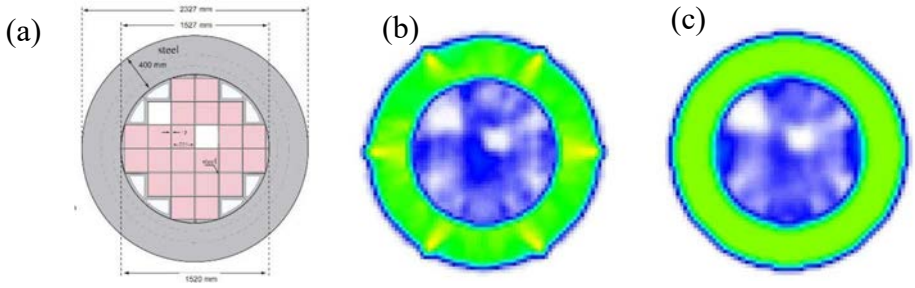

FIG. 70. (a) top view of a cask with two missing fuel assemblies; (b) the image obtained with data taken with the detector modules in three positions as shown in Fig. 71; (c) the image obtained with the same data after fixing the density of the DSC structure (reproduced from Ref. [115]).

With such inputs from the analysis of simulated data, the likelihood of a successful field test that demonstrates the capability of the technique is high. At present two preliminary experimental tests with drift tube detectors placed near casks loaded with spent fuel have been performed [116, 117]. In Ref. [116], the cask had several missing fuel assemblies. An indication was obtained, at the statistical level of 2.3σ, that the measures of the average scattering are lower than expected from simulation of a full cask. In the latter test, a small prototype was positioned near a CASTOR V/19[24] to demonstrate (successfully) that such a type of detector can reconstruct muon tracks even in the presence of the ionizing radiation emitted from the cask. Simulations have shown that muography would be capable of detecting a missing fuel rod in such a cask [118].

9.2. NUCLEAR MATERIAL CONTROL

The objective of nuclear material control is to prevent unauthorized use of nuclear material through tracking while maintaining continuous knowledge of the location of the nuclear material [119]. Confirmatory measurements of nuclear material when it is in storage, during processing, or movement enhance the effectiveness of the control. A variety of techniques and methods can be employed for nuclear material surveillance and monitoring. Examples of control techniques include radiation monitors, motion detectors, video surveillance cameras, weight sensors, heat sensors, etc. Use of a diversity of techniques applied for confirmatory measurements aims to prevent loss of control due to a single point failure. In this Section, the feasibility of applying muon imaging to maintain continuity of knowledge of nuclear material for scenarios not covered in Section 7 and Section 9.1 is discussed.

[24] CASTOR V/19 is similar to CASTOR V/52, containing up to 19 PWR fuel elements

In many instances of nuclear material control, direct confirmatory measurements are practically possible using conventional radiation detection methods combined with visual verification of the nuclear material setup to correct for presence of any shielding material. However, in some cases, such as treaty verification for nuclear disarmament verification or nuclear arms control, direct confirmation is impossible due to the requirement to keep capabilities and technological details of a warhead design hidden from the inspectors.

Verification of nuclear disarmament is an important international initiative towards reducing the number of nuclear weapons, and ultimately, complete disarmament. The International Partnership for Nuclear Disarmament Verification [120] is one of the ongoing initiatives that includes participation from weapon states. It aims to define the requirements for disarmament that are satisfactory to both disarmer and inspector, and to define technologies suitable to meet these requirements. One of the main challenges in the disarmament process is the verification of the nuclear material without revealing the technological details of the warhead or ancillary systems. Therefore, visual inspection and direct detection techniques, especially those that output detailed images, are unacceptable. Moreover, the nuclear core is typically surrounded by a tamper [121] which in turn shields the direct radiation making it challenging to confirm true absence of the fissile core after the dismantlement using conventional detectors. The ability to determine the presence or absence of nuclear material through a closed (shielded) cask wall is critical for such verification and control.

Another example of an application where direct confirmatory measurements are impractical, is treaty verification for arms control. Here, the objective is to ensure absence of undeclared additional warheads inside a weapon delivery system, while not exposing sensitive information on the warhead [122]. Gamma-rays and neutrons emitted by the additional unaccounted warhead can be masked with illicit shielding by a rogue state actor, therefore bypassing conventional gamma-ray and neutron monitors. There is simply not enough radiation that transmits through the shielded cask to verify presence or absence of the nuclear material inside. Cosmic ray muons, however, cannot be shielded and will detect presence of both, nuclear material as well as illicit high-density shielding.

9.2.1. State of the art

The sensitivity of muons to high atomic number (high-Z) materials via multiple Coulomb scattering makes MST a unique tool for passive non-destructive detection of nuclear material, including special nuclear material. The low flux of cosmic ray muons makes it impossible to produce detailed images in short times (minutes or hours depending on the configuration), naturally keeping the smaller technological details hidden.

Application of muon imaging to nuclear warhead inspection and verification has been studied by Los Alamos National Laboratory [99] with an example of counting nuclear warheads inside ballistic missiles on a submarine. Fissile materials, similar to those inside a nuclear warhead, can be detected and imaged using neutron tagged muons [123]. The technique requires knowledge of the incoming trajectory for the cosmic ray muon which then creates neutrons due to its interaction with a fissile material. The detection system consists of a single muon tracker and a neutron detector with an area similar to the tracker. The muon tracker is placed above the submarine missile hatch, whereas the neutron detector is positioned on top of the tracker as shown in Fig. 71. An experimental setup using low-enriched U was built to demonstrate performance of this method. It has been shown that the single sided neutron tagged muon imaging technique is able to reveal information sufficient for counting warheads even through 2.5 cm of steel within about a day of exposure time (Fig. 72). This time could be shortened to

hours with larger detectors. The position resolution is low; thus, all the sensitive details of the warhead are hidden.

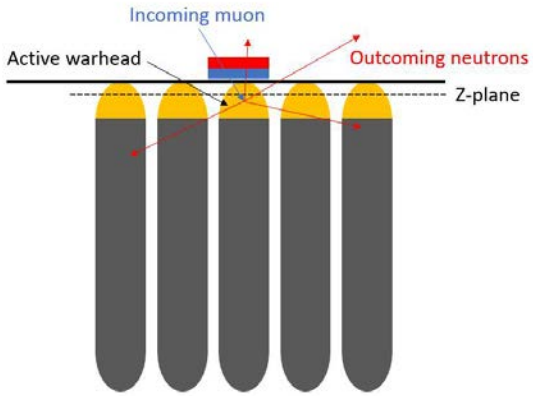

FIG. 71. Schematic of the detection system with a muon tracker (shown in blue) and a neutron detector (shown in red).

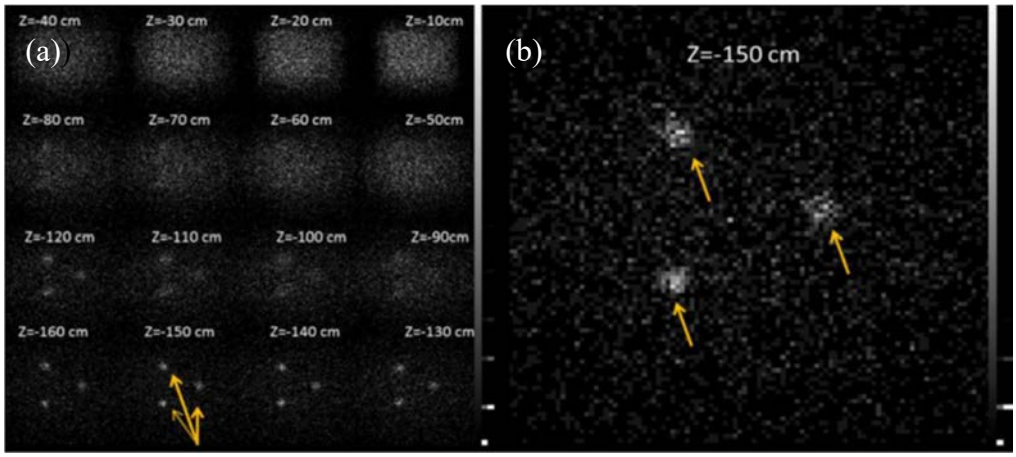

FIG. 72. Location of warheads: (a) Images as a function of distance from the detector; (b) Expanded image at the best focus. Each panel is a 200 cm square (reproduced from Ref. [124], U.S. Government work).

New methods of detection can impose an information barrier between an operator and the results of muon detection. A novel clustering-based method for analysing muon tomography data that does not rely on imaging for the detection of high-*Z* materials has been proposed and experimentally demonstrated at Canadian Nuclear Laboratories [125] for applications where imaging can be considered a disadvantage. The presence of high-ρ/-*Z* objects can be identified by a clustering method and a non-parametric statistical test to compare the muon tomography data against the assumed template data. The method outputs a single decision value for the absence/presence of high-ρ/-*Z* material (e.g., heavy nuclear warhead core). This process is operationally very simple, as a single value (e.g., red light or green light) is provided as an output to the operator, in contrast to detailed muon-based image reconstruction which relies on human interpretation of the image. The algorithm performance was validated using experimental data collected with the Cosmic ray Inspection and Passive Tomography detector at Canadian Nuclear Laboratories used in previous demonstrations for the detection of shielded nuclear material [126]. Fig. 73 shows the experimental setup.

Technology demonstrations for the International Partnership for Nuclear Disarmament Verification using muon tomography with the developed nonparametric dense object detection algorithm were conducted at Canadian Nuclear Laboratories in 2019. A mock-up model of a

warhead, consisting of a W cube and stainless-steel shielding of variable thickness for the tamper, was constructed for proof-of-concept experimental measurements. It demonstrated that muon tomography measurements conclusively identify the presence of a heavy warhead core after only a few hours of data collection, without the need for image reconstruction and human interpretation.

The ability to build scanners of nearly any size and the quantitative density information that can be obtained from muon tomography in both horizontal and vertical geometries suggests a broader range of surveillance activities that might be pursued. One can conceive of using muons to monitor a room, or even an entire building to continuously survey the storage and motion of nuclear materials within. This could be useful in treaty applications where nuclear weapons have been disassembled and their nuclear components have been put in monitored storage.

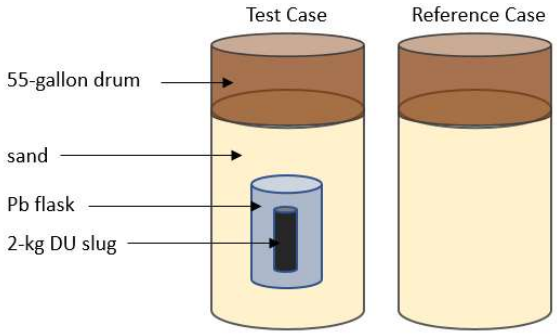

FIG. 73. Illustration of the test case with a Pb flask containing 2 kg of depleted U suspended within a 55-gallon steel drum filled with sand; the reference case is without the flask.

10. CONCLUSIONS

In almost all its current or potential applications, muon imaging has to compete with more established remote-sensing methods. Its main weakness is the limited flux of cosmogenic muons, which requires long acquisition times and large detection surfaces. Nevertheless, it has also several unique and complementary merits. For example, the intrinsic directionality of the method allows obtaining images of the target without relying on conceptually complex and computationally intense non-linear inversion procedures. The high penetrating power of muons makes them able to pass large depths of matter, probing the innermost volumes of very large objects of interest. Last but not least, it is a completely passive method that relies on a natural radiation source that poses no health hazard and is exempt from regulatory constraints.

Muon imaging lends itself to creating bridges between scientific communities that have to date been disconnected. It offers novel opportunities for technology transfer from academia to the private sector, as well as unprecedented collaborations between physicists and other academic communities. The field is currently very lively, with much of the research from universities spun-off or being undertaken in industrial partnerships. The ongoing transition to a phase of muon detector commercialization may have a profound impact. Ideally, a cheap, autonomous and easy to operate muon detector, even if not of the highest precision, may become a common tool of the trade for geological or archaeological prospecting. By cutting costs and reducing the need for expert operators, such a development would also create opportunities for scientists in developing countries to perform original research in domains where muon imaging has an advantage over more established, but also more expensive, imaging methods. Muon imaging can thus contribute to achieving some of the United Nation's Sustainable Development Goals (SDGs)[25], e.g., 'SDG 9' by supporting development of infrastructure and fostering innovation, to 'SDG 11' by preventing disasters in the built environment and preserving cultural and natural heritage, and 'SDG 17' through technological transfer.

Muon imaging has been successfully employed to date in a number of different civil engineering applications, including detecting components within concrete structures, and has been shown itself to be a promising complementary technique to other NDT methods. 'Real world' examples include the monitoring of the deformations of historical buildings. There is no shortage of candidate structures around the world that could be investigated with these techniques, which is also true of many of the archaeological applications. Muon imaging has also been shown to be of interest in predicting potential catastrophic ground instability, e.g., tunnel collapses and sink holes. The application to tunnel boring machines shows that muon imaging is capable of being applied dynamically while civil works are underway, provided the rate of forward progression conforms to the natural muon flux.

The rapid development of robust, transportable, and potentially commercial particle detectors provides a promising tool for archaeologists as it is ideal for in situ measurements, even in the presence of the public. Similar to the large number of potential civil structures to which muon imaging can be applied, studies of many large archaeological sites could be very promising, like the Qumran plateau, which could hide more caverns hosting the famous 'Dead Sea Scrolls', or known sites of prehistoric caverns to look for as yet undiscovered examples in their neighbourhood (e.g., a potential second Lascaux cavern). The list also includes sites associated with legends like the tomb mound of the first Qin Emperor and the tomb of Genghis Khan. Such tomb sites, however, have to be considered carefully, as it is likely that any discoveries of

[25] https://sustainabledevelopment.un.org; http://muographers2019.muographers.org/sdgs/

voids by this non-destructive method may be followed by destructive excavations to access them, which poses some ethical questions.

All archaeological measurements with muons to date have been done by physicists, in the best case within a collaboration with archaeologists. It seems essential in the coming years to transfer the know-how of this technology to archaeological field specialists. This implies the need for a special effort from the physics community, not only in training and sharing knowledge, but also in simplifying the instruments, which are currently far from plug-and-play versions, particularly on the analytical side.

Geoscience (most notably volcanology) is among the most popular applications of muography. Two different trends can be observed: (i) long-term, fixed monitoring facilities consisting of large area detectors and longer data collection to overcome statistical limitations, and (ii) development of portable detectors, which may open broader areas of investigation. Even more so than the applications for civil infrastructures, muon imaging of volcanoes has a large potential for hazard mitigation for affected populations. In this field, low energy muon identification systems to remove the main source of background affecting image quality are also being developed.

The application of muons to industrial process monitoring is especially promising for heavy industry, which is characterized by very large-scale engineering, often with limited physical access. The examples given in this publication include blast furnaces, rotary furnaces, insulated pipes, and a nuclear evaporator, which illustrate the utility of both muography and MST for dynamic, non-invasive, industrial process monitoring. In many cases, such information would otherwise be impossible or extremely expensive to obtain.

Originally invented for detection of special nuclear materials, MST has been expanded to the detection of other materials of interest, including various types of contraband. Large area scalable detectors based on drift tube technology have been built for this application, and a system is currently commercially available. Its capabilities have been already explored by the US Customs and Border Protection Agency and have attracted interest from other relevant organizations in different countries. The World Customs Organization has identified cosmic ray tomography as an emerging technology [127].

Homeland security, nuclear safeguards, decommissioning, and nuclear safety are areas of application for muon scattering in the nuclear field. Muon scattering has a clear advantage for detection of radioactive material in shielded storage containers because muons will pass through containers that are opaque to the radiation they are designed to shield. Similar to process monitoring in heavy industry, the chief attraction of muon imaging for many nuclear materials and technology applications lies in its ability to contrast materials with different values of the atomic number, Z, which is typically the case when special nuclear materials are involved.

Decommissioning and remedial activities are progressing on Europe's legacy nuclear sites and elsewhere, resulting in a wide range of packaged radioactive wastes for interim or long-term storage. Many of these waste forms will require initial characterization and subsequent monitoring of the evolution of their physical characteristics to underpin the safety case for their continued storage. The selection of results presented in this publication demonstrates that muon tomography is an effective and non-invasive interrogation technique for materials contained within heavily shielded and often heterogeneous packages. The method is clearly capable of meeting key characterization and monitoring metrics for diverse waste forms.

A goal of muon imaging applications in nuclear safeguards is to realise a full-scale detector that could be applied for re-verification of spent fuel casks in the case that continuity of knowledge has been lost. This would require a prototype, large enough to prove the concept but at reduced cost. For such a test, long data collection times, possibly with detectors movable in different positions as suggested above, could be acceptable. Simulations suggest that it would not be difficult to detect the absence of a fuel assembly, although few measurements have yet been performed (e.g., see Ref. [116]). However, more difficult requirements could be placed by safeguards inspectors; e.g., differentiation of spent fuel assemblies and the so-called dummy assemblies (steel objects having the same mass but a different geometry). This poses a difficult challenge to distinguish objects with the same geometry but different composition within the rods normally used to contain fuel pellets. Such technical requirements may require more data collection time, more sophisticated algorithms, and better performing detectors (e.g., able to evaluate single particle momenta).

The application of muon imaging for supporting the initiatives of arms control verification have been demonstrated, so far, by several proof-of-principle studies. In these scenarios, direct visual inspection and/or radiation measurements are impractical as weapon states will not share technological information pertaining to the weapon design. Muon imaging, however, can show deviations from the expected configuration with or without a warhead core, while keeping the smaller technological details inside the warhead hidden. Additionally, the combination of muon tracking with neutron detectors for tagging muon-induced fission events allows the unambiguous identification of the presence of fissile materials. Studies in that direction are on-going [128].

Finally, there are other applications to which muon imaging has been applied, but which have not been described in this report. These include other natural and manmade structures including the local structure [129] and regional distribution [130] of seismic faults, landslides [131], glacier beds [132], caves, and ore bodies [133]. There have been attempts to apply this technique to the carbon capture and storage monitoring [134], geothermal reservoir exploration [135], highway roads, debris flow control, and rockfill dam inspection. Muography is currently limited to the land, but submarine applications, monitoring of natural gas reservoirs, and even extra-terrestrial applications [20] are under consideration.

REFERENCES

[1] INTERNATIONAL ATOMIC ENERGY AGENCY, "Cosmic ray tomography: A probe from the stars", Nuclear Technology Review 2019, IAEA, Vienna (2019) 25–28.
[2] BONECHI, L., D'ALESSANDRO, R., GIAMMANCO, A., Atmospheric muons as an imaging tool, Rev. Phys. **5** (2020) 100038.
[3] PARTICLE DATA GROUP, Review of particle physics, Prog. Theor. Exp. Phys. **2020** 8 (2020) 083C01.
[4] BETHE, H., ASHKIN, J., "Passage of radiations through matter", Experimental Nuclear Physics, (SEGRÉ, E. Ed.), J. Wiley, New York (1953)
[5] GEORGE, E.P., Cosmic rays measure overburden of tunnel, Commonwealth Eng., July 1 (1955) 455.
[6] ALVAREZ, L.W., et al., Search for hidden chambers in the pyramids, Science **167** (1970) 832.
[7] MALMQVIST, L., JONSSON, G., KRISTIANSSON, K., JACOBSSON, L., Theoretical studies of in-situ rock density determination using cosmic ray muon intensity measurements with application in mining geophysics, Geophysics **44** 9 (1979) 1549.
[8] BOROZDIN, K.N., et al., Radiographic imaging with cosmic ray muons, Nature **422** (2003) 277.
[9] YIFAN, Z., Discrimination of drugs and explosives in cargo inspections by applying machine learning in muon tomography, High Power Laser Part. Beams **30** (2018) 086002.
[10] RUTHERFORD, E., The scattering of α and β rays by matter and the structure of the atom, Philos. Mag. **6** (1911) 21.
[11] MORRIS, C.L., et al., Tomographic imaging with cosmic ray muons, Sci. Global Secur. **16** (2008) 37.
[12] TSAI, Y.S., Pair production and bremsstrahlung of charged leptons, Rev. Mod. Phys. **46** 4 (1974) 815.
[13] WILLIAMS, N.R., The calculation of air density in various units, Bull. Am. Meteorol. Soc. **30** 9 (1949) 319.
[14] YANG, G., IELAND, D., KAISER, R., MAHON, D., "Machine Learning for Muon Imaging", Advances in Brain Inspired Cognitive Systems (REN, J. et al. Eds.), (Proc. 9th Int. Confer. on Advances in Brain Inspired Cognitive Systems, Xi'an, China, July 7–8, 2018), Lecture Notes in Computer Science, Springer (2018) 10989.
[15] CHAIWONGKHOT, K., et al., Development of a portable muography detector for infrastructure degradation investigation, IEEE Trans. Nucl. Sci. **65** (2018) 2316.
[16] KNOLL, G.F., Radiation Detection and Measurement, 4th edn, JW Wiley & Sons (2010).
[17] TIOUKOV, V., et al., First muography of Stromboli volcano, Sci. Rep. **9** (2019) 6695.
[18] EREDITATO, A., NIWA, K., STROLIN, P., OPERA: an emulsion detector for a long baseline $\nu_\mu - \nu_\tau$ oscillation search, Nucl. Phys. B **66** (1998) 423–427.
[19] GLASSER, V., LIPTON R., Data Analysis and Detector Troubleshooting for the Silicon Muon Scanner, Technical Report (FERMILAB-PUB-18-503-E), Fermi National Accelerator Laboratory, IL (2018).
[20] KEDAR, S., et al., Muon radiography for exploration of Mars geology, Geosci. Instrum. Methods Data Syst. **2** 1 (2013) 157.
[21] CATALANO, O., et al., Volcanoes muon imaging using Cherenkov telescopes, Nucl. Instrum. Methods A **807** (2016) 5.
[22] D'ALESSANDRO, R., et al., Volcanoes in Italy and the role of muon radiography, Philos. Trans. R. Soc. London, Ser. A **377** (2018) 0050.
[23] BONECHI, L., et al., A projective reconstruction method of underground or hidden structures using atmospheric muon absorption data, JINST **10** (2015) 02003.

[24] SCHUTZ, L.J., et al., Image reconstruction and material *Z* discrimination via cosmic ray muon radiography, Nucl. Instrum. Methods Phys. Res. A **519** 3 (2004) 687.
[25] VANINI, S., et al., Muography of different structures using muon scattering and absorption algorithms, Philos. Trans. R. Soc. London, Ser. A **377** (2018) 0051.
[26] GIOMATARIS, Y., REBOURGEARD, P., ROBERT, J.P., CHARPAK, G., MICROMEGAS: a high-granularity position-sensitive gaseous detector for high particle-flux environments. Nucl. Instrum. Methods Phys. Res. A **376** 1 (1996) 2935.
[27] HAGMANN, C., LANGE, D., WRIGHT, D., Cosmic ray shower generator (CRY) for Monte Carlo transport codes, 2007 IEEE Nucl. Sci. Symp. Confer. Record, 26 Oct.-3 Nov. 2007, Honolulu, Hawaii (2007) 1143–1146.
[28] CHAIZE, M.M.P., DAGBERT, M. Rapport d'information de fait au nom de la commission de l'aménagement du territoire et du développement durable (in French). Rapport n° 609 (2018–2019) 26 June 2019, Senate of the Government of France, Paris, France.
[29] MAYER, K., CINTA, P.M., User Guide of Graphical User Interface 52 interSAFT, Department of Computational Electronics and Photonics, Univ. Kassel, Germany (2012).
[30] NIEDERLEITHINGER, E., et al., Muon tomography of a reinforced concrete block: first experimental proof of concept, arXiv (2020) 2008.07251.
[31] BODINI, I., et al., Cosmic ray detection based measurement systems: a preliminary study, Meas. Sci. Technol. **18** (2007) 3537.
[32] DONZELLA, A., Stability monitoring of a historical building by means of cosmic ray tracking, Nuovo Cimento **37** C (2014) 223.
[33] ZENONI, A., et al., Historical building stability monitoring by means of a cosmic ray tracking system, arXiv (2014) 1403.1709.
[34] BONOMI, G., et al., Cosmic ray tracking to monitor the stability of historical buildings: a feasibility study, Meas. Sci. Technol. **30** (2019) 045901.
[35] ALLISON, J., et al., Recent developments in GEANT4, Nucl. Instrum. Methods A **835** (2016) 186–225.
[36] THE INSTITUTION OF FIRE ENGINEERS, The Clifton Hall Tunnel collapse, Incident Directory, https://www.ife.org.uk/Firefighter-Safety-Incidents/1953-clifton-hall-tunnel/39949.
[37] THOMPSON, L.F., et al., Muon tomography for railway tunnel imaging, Phys. Rev. Res. **2** (2020) 02301.
[38] KOTTMEIR, A., et al., New perspectives on interdisciplinary earth science at the Dead Sea: The DESERVE project, Sci. Total Environ. **544** (2016) 1045–1058.
[39] RUIZ-DEL ARBOL, P.M., GARCA, P.G., DIEZ GONZALEZ, C., ORIO ALONSO, A., Non-destructive testing of industrial equipment using muon radiography, Philos. Trans. R. Soc. London, Ser. A **377** (2018) 20180054.
[40] ASTROM, E., et al., Precision measurements of linear scattering density using muon tomography, JINST **11** (2016) P07010.
[41] ZANUTTIGH, P., et al. (MU-Blast collaboration), Study of the Capability of Muon Tomography to Map the Material Composition Inside a Blast Furnace, EU Publications, 2018.
[42] NAGAMINE, K., et al., Method of probing inner-structure of geophysical substance with the horizontal cosmic ray muons and possible application to volcanic eruption prediction, Nucl. Instrum. Methods A **356** (1995) 585–595.
[43] TANAKA, H.K.M., et al., Cosmic-ray muon imaging of magma in a conduit: Degassing process of Satsuma-Iwojima Volcano, Geophys. Res. Lett. **36** (2009) L01304.
[44] TANAKA, H.K.M., KUSAGAYA, T., SHINOHARA, H., Radiographic visualization of magma dynamics in an erupting volcano, Nat. Commun. **5** (2014) 3381.
[45] SHINOHARA, H., TANAKA, H.K.M., Conduit magma convection of a rhyolitic magma: constraints from cosmic ray muon radiography of Iwodake, Satsuma-Iwojima volcano, Japan, Earth Planet. Sci. Lett. **349–350** (2012) 87–97.

[46] KAZAHAYA, R., et al., Pre-eruptive inflation caused by gas accumulation: Insight from detailed gas flux variation at Sakurajima volcano, Japan, Geophys. Res. Lett. **43** (2016) 11,219–11,225.
[47] YOKOO, A., IGUCHI, M., TAMEGURI, T., YAMAMOTO, K., Processes prior to outbursts of vulcanian eruption at showa crater of Sakurajima volcano, Bull. Volcanol. Soc. Jpn. **58** (2013) 163–181.
[48] OLAH, L., TANAKA, H.K.M., OHMINATO, T., VARGA, D., High-definition and low-noise muography of the Sakurajima volcano with gaseous tracking detectors, Sci. Rep. **8** (2018) 3207.
[49] OLAH, L., et al., Plug formation imaged beneath the active craters of Sakurajima volcano with muography, Geophys. Res. Lett. **46** (2019) 10417–10424.
[50] TANAKA, H.K.M., et al., Imaging the conduit size of the dome with cosmic-ray muons: The structure beneath Showa-Shinzan Lava Dome, Geophys. Res. Lett. **34** (2007) L22311.
[51] KUSAGAYA, T., TANAKA, H.K.M., Muographic imaging with a multi-layered telescope and its application to the study of the subsurface structure of a volcano, Proc. Jpn. Acad. Ser. B Phys. Biol. Sci. **91** (2015) 501–510.
[52] TANAKA, H.K.M., Instant snapshot of the internal structure of Unzen lava dome, Japan with airborne muography, Sci. Rep. **6** (2016) 39741.
[53] KUSAGAYA, T., TANAKA, H.K.M., Development of the very long-range cosmic ray muon radiographic imaging technique to explore the internal structure of an erupting volcano, Shinmoe-dake, Japan, Geosci. Instrum. Methods Data Syst. **4** (2015) 215–226.
[54] LO PRESTI, D., et al., Design and testing of a new high-resolution telescope for muography of Etna volcano, Nucl. Instrum. Methods A **904** (2018) 195.
[55] TIOUKOV, V., et al., First muography of Stromboli volcano, Sci. Rep. **9** (2019) 6695.
[56] SARACINO, G., et al., The MURAVES muon telescope: technology and expected performances, Ann. Geophys. **60** (2017) 0103.
[57] JOURDE, K., et al., Muon dynamic radiography of density changes induced by hydrothermal activity at the La Soufrière of Guadeloupe volcano, Sci. Rep. **6** (2016) 33406.
[58] CARLOGANU, C., et al., Towards a muon radiography of the Puy de Dôme, Geosci. Instrum. Methods Data Systems **2** (2013) 55.
[59] TIOUKOV, V., et al., Muography with nuclear emulsions – Stromboli and other projects, Ann. Geophys-Italy **60** 1 (2017) S0111.
[60] NISHIYAMA, R., et al., Monte Carlo simulation for background study of geophysical inspection with cosmic ray muons, Geophys. J. Int. **206** 2 (2016) 1039–1050.
[61] BARBERI, F., "Risk assessment of Vesuvius volcano", paper presented at GIFT2013, European Geophysical Union General Assembly, Vienna, Austria, 2013.
[62] MACEDONIO, G., MARTINI, M., Motivations for muon radiography of active volcanoes, Earth Planets Space **62** (2010) 139–143.
[63] AMBROSINO, F., et al., The MU-RAY project: detector technology and first data from Mt. Vesuvius, JINST **9** (2014) 2029.
[64] AMBROSINO, F., et al., Joint measurement of the atmospheric muon flux through the Puy de Dome volcano with plastic scintillators and resistive plate chambers detectors, J. Geophys. Res. Solid Earth **120** 11 (2015) 7290.
[65] GOMEZ, H., et al., Forward scattering effects on muon imaging, JINST **12** 12 (2017) 12018.
[66] CARBONE, D., et al., An experiment of muon radiography at Mt Etna (Italy), Geophys. J. Int. **196** 2 (2013) 633.
[67] GALLO, G., et al., Improvements of data analysis and self-consistent monitoring methods for the MEV telescope, Nucl. Instr. Methods A. **958** (2020), 162052.

[68] BONANNO, D., et al., Measurement of nearly horizontal cosmic muons at high altitudes with the MEV telescope, Eur. Phys. J. Plus **134** (2019) 281.
[69] GALLO, G., Particelle cosmiche per studiare l'Etna (in Italian), SIF Prima Pagina **60** (2018) 877.
[70] LO PRESTI, D., et al., Feasibility study of a new Cherenkov detector for improving volcano muography, Sensors **19** (2019) 1183.
[71] CATALANO, O., et al., Volcanoes muon imaging using Cherenkov telescopes, Nucl. Instrum. Methods A **807** (2016) 5.
[72] DEL SANTO, M., et al., Looking inside volcanoes with the imaging atmospheric cherenkov telescopes, Nucl. Instrum. Methods A **876** (2017) 111.
[73] CTA CONSORTIUM, Design concepts for the Cherenkov telescope array CTA: an advanced facility for ground-based high-energy gamma-ray astronomy, Exp. Astron. **32** 3 (2011) 193.
[74] LE GONIDEC Y. et al., Abrupt changes of hydrothermal activity in a lava dome detected by combined seismic and muon monitoring, Sci. Rep. **9** 1 (2019) 3079.
[75] ALVAREZ, L.W., Adventures of a Physicist, Alfred P Sloan Foundation Series, Basic Books, New York (1989).
[76] MENCHAC-ROCHA, A., Searching for cavities in the Teotihuacan Pyramid of the Sun using cosmic muons experiments and instrumentation, Int. Cosmic Ray Confer. **4** (2011) 325.
[77] MORISHIMA, K., et al., Development of nuclear emulsion for muography, Ann. Geophys. **60** (2017) 0112.
[78] FUJII, H., et al., Detection of on-surface objects with an underground radiography detector system using cosmic ray muons, Prog. Theor. Exp. Phys. **5** (2017) 053C01.
[79] BOUTEILLE, S., et al., A Micromegas-based telescope for muon tomography: The WatTo experiment, Nucl. Instrum. Methods A **834** (2016) 223–228.
[80] BOUTEILLE, S., PROCUREUR, S., Procédé et dispositif de rétroaction sur la haute tension d'un détecteur gazeux (in French), Brevet **17** (2017) 57755.
[81] SCAN PYRAMIDS MISSION. First conclusive findings with muography on Khufu Pyramid. Press Release Cairo, October 15, 2016.
[82] MORISHIMA, K., et al., Discovery of a big void in Khufu's Pyramid by observation of cosmic ray muons, Nature **552** (2017) 386–390.
[83] PROCUREUR, S., et al., Why do we flush gas in gaseous detectors? Nucl. Instr. Methods A **955** (2020) 163290.
[84] BACCANI, G., et al., The MIMA project. Design, construction and performances of a compact hodoscope for muon radiography applications in the context of archaeology and geophysical prospections, JINST **13** (2018) 11001.
[85] SARACINO, G., et al., Imaging of underground cavities with cosmic ray muons from observations at Mt. Echia (Naples), Sci. Rep. **7** (2017) 1181.
[86] BONECHI, L., et al., Multidisciplinary applications of muon radiography using the MIMA detector, JINST **15** (2020) C05030.
[87] CIMMINO, L., et al., 3D muography for the search of hidden cavities, Sci. Rep. **9** (2019) 2974.
[88] BACCANI, G., et al., Muon radiography of ancient mines: the San Silvestro archaeo-mining park (Campiglia Marittima, Tuscany), Universe **5** (2019) 34.
[89] BORSELLI, D., Studio muografico della miniera del Temperino con il rivelatore MIMA: sviluppo e test di un algoritmo di identificazione e ricostruzione di cavità in tre dimensioni, Master's thesis (in Italian), Univ. Florence, Italy (2020).
[90] HANAZATO, T., TANAKA, H.K.M., Inspection of the internal structure of the UNESCO-World Heritage with cosmic rays, Isotope News (in Japanese) **741** (2016) 60–64.

[91] KAMAI, T., et al., 1596, Keicho Obushi Landslides on an ancient tomb due to an earthquake, Jpn. Soc. Eng. Geol. **48** 6 (2008) 285–298.
[92] TANAKA, H.K., SUMIYA, K., OLÁH, L., Muography as a new tool to study the historic earthquakes recorded in ancient burial mounds, Geosci. Instrum. Methods Data Syst. **9** 2 (2020) 357–364.
[93] MORRIS, C.L., et al., Obtaining material identification with cosmic ray radiography. AIP Adv. **2** (2012) 042128.
[94] SCHULTZ, L.J., et al., "Cosmic Ray Muon Radiography for Contraband Detection," LA-UR-03-4804, Los Alamos National Laboratory, USA (2003).
[95] ÅSTRÖM, E., et al., Precision measurements of linear scattering density using muon tomography, J. Instrum. **11** 7 (2016) P07010.
[96] CHECCHIA, P., Review of possible applications of cosmic muon tomography, J. Instrum. **11** 12 (2016) C12072.
[97] ANTONUCCIO, V. et al., The muon portal project: design and construction of a scanning portal based on muon tomography, Nucl. Instrum. Methods Phys. Res. Sect. A **845** (2017) 322–325.
[98] PUGLIATTI, C., et al., Design of a muonic tomographic detector to scan travelling containers, J. Instrum. **9** 5 (2014) C05029.
[99] MORRIS, C.L., et al., A new method for imaging nuclear threats using cosmic ray muons, AIP Adv. **3** 8 (2013) 082128.
[100] MORRIS, C., et al., Radiation Portal Monitor System and Method, U.S. Patent 7,633,062, issued December 15, 2009.
[101] BOROZDIN, K., "The next generation of passive non-intrusive inspection", Proc. 6th Meeting of TEG-NII, Brussels, November 13–14, 2019.
[102] MAHON, D., et al., First-of-a-kind muography for nuclear waste characterization, Philos. Trans. R. Soc. London, Ser. A **377** 2137 (2019) 20180048.
[103] YANG, G., et al., Novel muon imaging techniques, Philos. Trans. R. Soc. London, Ser. A **377** 2137 (2019) 20180062.
[104] SIMPSON, A., et al., Muon tomography for the analysis of in-container vitrified products, Appl. Rad. Isotopes **157** (2020) 109033.
[105] TIETZE-JAENSCH, H., et al., "Numerical assessment of SNF parameter bandwidths and muon tomography assay for large volume casks", Proc. WM2018 Confer., 18–27 March 2018, Phoenix, AZ (2018) 18185.
[106] BAESSO, P., et al., A high resolution resistive plate chamber tracking system developed for cosmic ray muon tomography, JINST **8** (2013) 08006.
[107] THOMAY, C., et al., A binned clustering algorithm to detect high-*Z* material using cosmic muons, JINST **8** (2013) 10013.
[108] DOBROWOLSKA, M., et al., A novel technique for finding gas bubbles in the nuclear waste containers using muon scattering tomography, JINST **13** (2018) 05015.
[109] FRAZAO, L., VELTHUIS, J., THOMAY, C., STEER, C., Discrimination of high-*Z* materials in concrete-filled containers using muon scattering tomography. JINST **11** 7 (2016) 07020.
[110] WEEKES, M., et al., Material identification in nuclear waste drums using muon scattering tomography and multivariate analysis, arXiv (2020) 2012.01554v1.
[111] INTERNATIONAL ATOMIC ENERGY AGENCY, Operation and Maintenance of Spent Fuel Storage and Transportation Casks/Containers, IAEA-TECDOC-1532, IAEA, Vienna (2007).
[112] STAPLETON, M., et al., Angle statistics reconstruction: a robust reconstruction algorithm for muon scattering tomography, JINST **9** (2014) 11019.

[113] ALRHELI, A., et al., “A muon scattering tomography method for verification of fuel assemblies stored in V/52 CASTOR”, Proc. WM2021 Confer., 7–11 March 2021, Phoenix, AZ (2021) 21123.
[114] POULSON, D., et al., Cosmic ray muon computed tomography of spent nuclear fuel in dry storage casks, Nucl. Instrum. Methods A **842** (2017) 48–53.
[115] ANCIUS, D., et al., “Modelling of safeguards verification of spent fuel dry storage casks using muon trackers”, Proc. ESARDA 41st Annual Meeting Symp. on Safeguards and Nuclear Material Management, 14–16 May 2019, Regina Palace Hotel, Stresa (VB), Italy (2019) 142–148.
[116] DURHAM, J.M., et al., Verification of spent nuclear fuel in sealed dry storage casks via measurements of cosmic ray muon scattering, Phys. Rev. Appl. **9** (2018) 044013.
[117] CHECCHIA, P., et al., “Cosmic ray muography”, Proc. IAEA Symp. on International Safeguards, Vienna (2018).
[118] BRAUNROTH, T., BERNER, N., ROWOLD, F., PÉRIDIS, M., STUKE, M., Muon radiography to visualise individual fuel rods in sealed casks, EPJ Nucl. Sci. Technol. **7** (2021) 12.
[119] INTERNATIONAL ATOMIC ENERGY AGENCY, Use of Nuclear Material Accounting and Control for Nuclear Security Purposes at Facilities, IAEA Nuclear Security Series No. 25-G, Vienna (2015).
[120] HINDERSTEIN, C., International Partnership for Nuclear Disarmament Verification: Laying a foundation for future arms reductions, Bull. At. Sci. **74** (2018) 305.
[121] FETTER, S., et al., Detecting nuclear warheads, Sci. Global Secur. **1** (1990) 225.
[122] ZIOCK, K.P., Principles and applications of gamma-ray imaging for arms control, Nucl. Instrum. Methods A **878** (2018) 191.
[123] GUARDINCERRI, E., et al., Detecting special nuclear material using muon-induced neutron emission, Nucl. Instrum. Methods A **789** (2015) 109.
[124] MORRIS, C.L., et al., Horizontal cosmic ray muon radiography for imaging nuclear threats, Nucl. Instrum. Methods B **330** (2014) 42.
[125] RAND, E.T., et al., Nonparametric dense-object detection algorithm for applications of cosmic ray-muon tomography, Phys. Rev. Appl. **14** 6 (2020) 064032.
[126] KAMAEV, O., et al., Complementary non-destructive detection of nuclear materials with passive neutron and gamma-ray detectors, and a large-volume muon tomography system, Nucl. Instrum. Methods A **944** (2019) 162503.
[127] WORLD CUSTOMS ORGANIZATION, Guidelines for the Procurement and Deployment of Scanning/NII Equipment, Brussels (2018).
[128] BACON, J.D., et al., Muon Induced Fission Neutrons in Coincidence with Muon Tomography, report LA-UR-13-28292, Los Alamos National Laboratory, Los Alamos NM (2013).
[129] TANAKA, H.K.M., et al., Cosmic muon imaging of hidden seismic fault zones: Rainwater permeation into the mechanical fractured zones in Itoigawa–Shizuoka Tectonic Line, Earth Planet. Sci. Lett. **306** 3–4 (2011) 156–162.
[130] TANAKA, H.K.M., Muographic mapping of the subsurface density structures in Miura, Boso and Izu peninsulas, Japan, Sci. Rep. **5** (2015) 8305.
[131] TANAKA, H.K.M., SANNOMIYA, A., Development and operation of a muon detection system underextremely high humidity environment for monitoring undergroundwater table, Geosci. Instrum. Methods Data Syst. **2** (2013) 29–34.
[132] NISHIYAMA, R., et al., Bedrock sculpting under an active alpine glacier revealed from cosmic ray muon radiography, Sci. Rep. **9** (2019) 6970.
[133] SCHOUTEN, D., Muon geotomography: selected case studies, Phil. Trans. R. Soc, Ser. A. **377** 2137 (2019) 20180061.

[134] GLUYAS, J., et al., Passive, continuous monitoring of carbon dioxide geostorage using muon tomography, Phil. Trans. R. Soc. A **377** (2018) 0059.
[135] TANAKA, H.K.M., MURAOKA, H., Interpreting muon radiographic data in a fault zone: possible application to geothermal reservoir detection and monitoring, Geosci. Instrum. Method. Data Systems **2** 1 (2013) 145–150.

LIST OF ABBREVIATIONS

ASR	Angle Statistics Reconstruction
BF	Blast Furnaces
CEA	Commissariat à l'énergie atomique et aux énergies alternatives
DSC	Dry Storage Casks
ILW	Intermediate Level Waste
MEV	Muography of Etna Volcano
MIMA	Muon Imaging for Mining and Archaeology
MIS	Muon Imaging System
MLEM	Maximum Likelihood / Expectation Maximization
MSSS	Magnox Swarf Storage Silo
MST	Muon Scattering Tomography
MVA	Multivariate Analysis
mwe	Metres of water equivalent
NDA	Non-Destructive Assay
NDT	Non-Destructive Testing
NE	Nuclear Evaporators
NNL	National Nuclear Laboratory
PE300	Polyethylene 300
POCA	Point of Closest Approach
RPC	Resistive Plate Chamber
RPM	Radiation Portal Monitor
SQ	Significant Quantity
TBM	Tunnel-Boring Machine
UPVC	Unplasticized Polyvinyl Chloride

CONTRIBUTORS TO DRAFTING AND REVIEW

Affum, H.	Ghana Atomic Energy Commission, Ghana
Alrheli, A.	University of Sheffield, United Kingdom
Ancius, D.	EURATOM, Luxembourg
Andringa Dias, S.	Laboratorio de Instrumentacao e Fisica Experimental de Particulas, Portugal
Aymanns, K.	Forschungszentrum Jülich GmbH, Germany
Barker, D.	University of Sheffield, United Kingdom
Besnard-Vauterin, C.	International Atomic Energy Agency
Bonechi, L.	Istituto Nazionale di Fisica Nucleare, Italy
Bonomi, G.	Istituto Nazionale di Fisica Nucleare, Italy
Borozdin, K.	Decision Sciences International Corporation, United States of America
Borselli, D.	Istituto Nazionale di Fisica Nucleare, Italy
Bosnar, D.	University of Zagreb, Croatia
Brisset, P.	International Atomic Energy Agency
Checchia, P.	Istituto Nazionale di Fisica Nucleare, Italy
Cortina Gil, E.	Université catholique de Louvain, Belgium
Dahlberg, J.	International Atomic Energy Agency
D'Alessandro, R.	University of Florence, Italy
De Sio, C.	University of Bristol, United Kingdom
Díez González, C.	Muon Tomography Systems S.L., Spain
Dobrowolska, M.	University of Bristol, United Kingdom
Foulon, F.	International Atomic Energy Agency
Giammanco, A.	Université catholique de Louvain, Belgium
Harel, A.	Lingacom Ltd, Israel
Heng, Y.K.	Institute of High Energy Physics, China
Hlavac, S.	Institute of Physics SAS, Slovakia
Jussofie, A.	Gesellschaft für Zwischenlagerung mbH, Germany
Kaiser, R.	Lynkeos Technology Ltd, United Kingdom; University of Glasgow, United Kingdom
Kamaev, O.	Canadian Nuclear Laboratories, Canada
Kikola, D.	Warsaw University of Technology, Poland

Kopp, A.K.	H. H. Wills Physics Laboratory, United Kingdom
Marteau, J.	Institut de physique des deux infinis, France
Martinez Ruiz Del Arbol, P.	Institute of Physics of Cantabria, Spain
Massey, C.	International Atomic Energy Agency
Mavric, H.	International Atomic Energy Agency
Mhaidra, M.	University of Bristol, United Kingdom
Morris, C.L.	Los Alamos National Laboratory, United States of America
Procureur, S.	CEA-Saclay, France
Rezniczek, A.	UBA Unternehmensberatung GmbH, Germany
Smith, N.A.	International Atomic Energy Agency
Stanca, D-I.	Horia Hulubei National Institute, Romania
Steer, C.A.	Geoptic Infrastructure Imaging Ltd, United Kingdom
Stowell, P.	University of Sheffield, United Kingdom
Swainson, I.P.	International Atomic Energy Agency
Thompson, L.F.	Geoptic Infrastructure Imaging Ltd, United Kingdom; University of Sheffield, United Kingdom
Tietze-Jaensch, H.	European Spallation Source, Sweden
Tytgat, M.G.	Ghent University, Belgium
Veltius, J.	University of Bristol, United Kingdom
Vieh, C.	Bundesgesellschaft für Endlagerung, Germany
Weekes, M.	University of Sheffield, United Kingdom
Whitlock, J.	International Atomic Energy Agency
Yang, G.	University of Glasgow, United Kingdom
Yaish, D.	Lingacom Ltd, Israel

Consultancy Meeting

Vienna, Austria: 25–29 September 2017

Technical Meeting

Vienna, Austria: 9–12 September 2019

IAEA
International Atomic Energy Agency

No. 26

ORDERING LOCALLY

IAEA priced publications may be purchased from the sources listed below or from major local booksellers.

Orders for unpriced publications should be made directly to the IAEA. The contact details are given at the end of this list.

NORTH AMERICA

Bernan / Rowman & Littlefield

15250 NBN Way, Blue Ridge Summit, PA 17214, USA
Telephone: +1 800 462 6420 • Fax: +1 800 338 4550

Email: orders@rowman.com • Web site: www.rowman.com/bernan

REST OF WORLD

Please contact your preferred local supplier, or our lead distributor:

Eurospan Group

Gray's Inn House
127 Clerkenwell Road
London EC1R 5DB
United Kingdom

Trade orders and enquiries:

Telephone: +44 (0)176 760 4972 • Fax: +44 (0)176 760 1640
Email: eurospan@turpin-distribution.com

Individual orders:

www.eurospanbookstore.com/iaea

For further information:

Telephone: +44 (0)207 240 0856 • Fax: +44 (0)207 379 0609
Email: info@eurospangroup.com • Web site: www.eurospangroup.com

Orders for both priced and unpriced publications may be addressed directly to:

Marketing and Sales Unit
International Atomic Energy Agency
Vienna International Centre, PO Box 100, 1400 Vienna, Austria
Telephone: +43 1 2600 22529 or 22530 • Fax: +43 1 26007 22529
Email: sales.publications@iaea.org • Web site: www.iaea.org/publications

International Atomic Energy Agency
Vienna